Travail de fin d'études et stage[BR]- Travail de fin d'études : Fabrication and characterization of AISI S2 Tool Steel + SiC by Laser Powder Bed Fusion[BR]- Stage d'insertion professionnelle

Auteur : p253917
Promoteur(s) : Mertens, Anne
Faculté : Faculté des Sciences appliquées
Diplôme : Cours supplémentaires destinés aux étudiants d'échange (Erasmus, ...)
Année académique : 2022-2023
URI/URL : http://hdl.handle.net/2268.2/17799

Université de Liège - Faculté des Sciences Appliquées

Universitat Politècnica de Catalunya – Escola Superior d'Enginyeries Industrial Aeroespacial i Audiovisual de Terrassa

Fabrication and characterization of AISI S2 Tool Steel + SiC by Laser Powder Bed Fusion

Master's Thesis completed in order to obtain the Degree of Master of Mechanical Engineering by

Gerard Roger Vila

Supervisor: Prof. Anne Mertens (Université de Liège)

Academic course 2022-2023

ABSTRACT

The present study evaluates the processability of AISI S2 plus 10% in volume of SiC through the Laser Powder Bed Fusion (LPBF) technology. It is the continuation of the work "Fabrication and characterization of low-alloyed tool steel obtained by Selective Laser Melting," 2023 [1] carried out by the same team. This S2 low-alloyed tool steels have been rarely studied in Additive Manufacturing (AM) due to poor welding properties. Using alloying methods to create Metal Matrix Composites (MMCs) can improve several properties of these steels though. For instance, adding SiC nanoparticles to AISI S2 enhances both the hardness and wear resistance among other properties, but in the meantime, this will increase the carbon content which has been found to promote crack appearances. Therefore, a careful evaluation of the processability of the MMCs is needed.

In order to analyse the capability of fabricating these samples, two different batches were considered, one with and another without preheating the baseplate of the printer. Achieving crack-free fully dense samples is demonstrated to be possible under some premises. There is a tendency for SiC nanoparticles to agglomerate, thus leading to non-homogeneous properties. Therefore, optimizing the powders preparation is required. Different kind of defects may be observed on parts processed by LPBF depending on processing parameters. Therefore, optimizing the parameters of the LPBF laser process is also mandatory to set a defined processing map for each batch of samples. Nevertheless, preheating of the baseplate seems to be required since all the samples without preheating exhibit cracks.

Moreover, taking advantage of both batches, the influence of the preheating on both the microstructure and the mechanical properties is highlighted. Furthermore, the effect of SiC nanoparticles addition is enhanced when comparing the MMCs to S2 samples obtained from LPBF process.

RÉSUMÉ

Cette étude évalue la mise en œuvre du composite à matrice métallique AISI S2 plus 10 % en volume de nanoparticules SiC par le procédé de fusion laser sur lit de poudre (LPBF, Laser Power Bed Fusion). Elle fait suite au travail intitulé « Fabrication and characterization of low-alloyed tool steel obtained by Selective Laser Melting », 2023 [1], réalisé par la même équipe. Les études sur les aciers à outils à faible teneur en éléments d'alliage tel que la nuance AISI S2, qui sont mis en œuvre par fabrication additive sont rares, car ces alliages ont une soudabilité limitée. Cependant, la possibilité de mélanger des poudres pour produire par fabrication additive des composites à matrice métallique (Metal Matrix Composites) pourrait améliorer plusieurs propriétés de ces aciers. En l'occurrence, l'ajout de nanoparticules de SiC améliore notamment la dureté et la résistance à l'usure, entre autres propriétés. Cependant, un tel mélange de poudres va aussi augmente le teneur en carbone du composite, ce qui va favoriser la formation de fissures en cours de procédé. Cet antagonisme nécessite donc une évaluation minutieuse de la mise en œuvre de tels MMCs par le procédé LPBF.

C'est afin dans le but d'étudier la faisabilité de la production de tels MMCs par LBPF qu'on a considéré deux lots différents du même composite S2+10%SiC, l'un avec préchauffage du substrat support d'impression 3D, et l'autre sans préchauffage du substrat. Une des premières contributions de l'étude est de démontrer dans quelles conditions il est possible d'obtenir des échantillons entièrement denses et sans fissures. L'étude permet aussi de montrer qu'il est important d'avoir une préparation optimale du mélange des poudres pour obtenir l'homogénéité, en évitant notamment la tendance à l'agglomération des nanoparticules de SiC. Les paramètres de processus optimaux du laser LPBF sont également obligatoires. La variation des paramètres du procédé LPBF peut conduire à différents types de défauts dans les pièces imprimées. C'est pourquoi il faut aussi déterminer la fenêtre optimale pour les paramètres du procédé, celle-ci étant influencée par le ratio des poudres mélangées, mais aussi par l'existence ou non du préchauffage du substrat. L'étude a aussi permis de déterminer les paramètres de procédé définissant la fenêtre optimale pour chaque lot d'échantillons, selon qu'on soit avec ou sans préchauffage du substrat. Il a aussi été observé que le préchauffage était nécessaire pour éviter la fissuration en cours de fabrication.

La comparaison des deux lots d'échantillons (avec et sans préchauffage) permet en outre de mettre en évidence l'effet du préchauffage d'une part sur la microstructure, et d'autre part sur les propriétés mécaniques, notamment la dureté. Par ailleurs l'influence de l'addition de nanoparticules SiC sur la microstructure de l'acier à outil S2 élaborée par LPBF est discutée, en comparant les résultats de cette étude avec ceux des précédents travaux.

RESUMEN

El presente estudio evalúa la procesabilidad del AISI S2 con un 10% en volumen de SiC a través de la tecnología Laser Powder Bed Fusion (LPBF). Es la continuación del trabajo “Fabrication and characterization of low-alloyed tool steel obtained by Selective Laser Melting” 2023 [1] realizado por el mismo equipo. Estos aceros para herramientas de baja aleación, S2, rara vez se han estudiado para la fabricación aditiva debido a sus pobres propiedades de soldadura. Sin embargo, el uso de métodos de aleación para crear compuestos de matriz metálica puede mejorar varias propiedades de estos aceros. Por ejemplo, añadir nanopartículas de SiC al S2 mejora la dureza y la resistencia al desgaste, entre otras propiedades pero a su vez aumenta el contenido de carbono que se ha comprobado que promueve la aparición de grietas. Por ello, se necesita una evaluación cuidadosa de la procesabilidad de los compuestos de matriz metálica.

Para analizar la capacidad de fabricar estas muestras, se crearon dos lotes diferentes, uno con y otro sin precalentar la placa base de la impresora. La obtención de muestras completamente densas libres de grietas es posible bajo algunas premisas. La tendencia de las partículas de SiC a aglomerarse conlleva propiedades no homogéneas. Entonces, la optimización del proceso de creación de polvos es necesaria. Diferentes defectos pueden ser observados en las muestras hechas por LPBF dependiendo de los parámetros. Por ello, optimizar los parámetros del láser también es obligatorio. Por último, se requiere el precalentamiento de la placa base puesto que todas las muestras sin ello muestran grietas.

Además, aprovechando ambos lotes, el efecto del precalentamiento sobre las propiedades y microestructura de las muestras es remarcado. También, comparando las muestras con el estudio previo realizado por el equipo con muestras de S2, también se incluye un estudio del efecto del SiC.

ACKNOWLEDGMENTS

My first acknowledgements go to Prof. Anne Mertens and Dr. Jérôme Tchoufang Tchuindjang for being the supervisors of my thesis and for guiding me anytime. I would also like to thank my former university Universitat Politècnica de Catalunya for all the paperwork that led me to this destination, and Université de Liège for accepting and welcoming me so well.

Enrico Saggionetto deserves special mention for working on everything hand to hand with me, helping, and guiding me at every stage of my thesis. The team from the Metallic Materials Science (MMS) department also deserves my deepest gratitude. It is composed by Sylvie Salieri, Rosine Pirson, Olivier Dedry and Herrim Seidou. They included me in every aspect and helped me with all of the drawbacks and difficulties during this period.

Furthermore, my family and friends have been a fundamental pilar in this experience. My mother, father, and sister have been essential in giving me the courage to take this experience, knowing they are always supporting me from Spain, and being my first backup in the difficult moments of indecision. Also, my group of friends “Guada”. Their support and constant presence made me appreciate how important and special they are.

Deep acknowledgments to my university friends “Indus family”. They have made my overall university phase easier not only in terms of friendship but also in pushing me to obtain the best results. Their support made easier the long study days and the solving of difficult problems proposed in class. Without them, the academic experience would have been much harder and they also have lead me to where I am now.

Finally, I thank all my new friends and colleagues who I have met in the Erasmus experience. They have been my day-to-day backup and have made this stage of my life unsurpassable.

TABLE OF CONTENTS

LIST OF FIGURES

LIST OF TABLES

GLOSSARY

AM: Additive Manufacturing

CM: Conventional Machining

DTA: Differential Thermal Analysis

EBSD: Electron Backscatter Diffraction

EDX: Energy-dispersive X-ray spectroscopy

HAZ: Heat Affected Zone

HIP: Hot Isostatic Pressing

LOF: Lack Of Fusion

LPBF: Laser Powder Bed Fusion

MA: Mechanical Alloying

MMCs: Metal Matrix Composites

MS: Maraging Steel

Ms: Martensite start temperature

OM: Optical Microscope

PSD: Particle Size Distribution

P500: Preheating of 500ºC

SEM: Scanning Electron Microscope

SLM: Selective Laser Melting

SLS: Selective Laser Sintering

VED: Volumetric Energy Density

XRD: X-ray Diffraction

1 INTRODUCTION

During the last decades Additive Manufacturing (AM) has been increasingly investigated due to its advantages in comparison to conventional manufacturing techniques. Nowadays, the processability of some materials with this technology is yet to be analysed. More specifically, there has been a huge interest in mechanically alloyed materials for their ability of properties improvement [2]. In Laser Powder Bed Fusion (LPBF), ceramic reinforced metal matrixes have been a focus of study because ceramic materials can improve the mechanical and tribological behaviour of the matrix [3]. However, the processability with LPBF might be difficult for the intrinsic out-of-equilibrium conditions of the technology along with high-carbon composites, that usually have issues with AM according to several studies [4] [5].

This Master's thesis consists in a part of a PhD thesis that aims to fabricate innovative alloys, usually metals, using LPBF technology. To do so, the optimal mixture of powders to create the alloy and the later printing of samples is required. A multiscale characterization is performed on the samples to better understand the microstructure evolution during the printing. The microstructure, then, can be related to the final properties that the samples will have. The final objective, however, is to produce crack-free fully dense samples with these new alloys.

In this study, two different batches of samples were produced. One using the preheating of the baseplate and the other without using it. The samples were printed using powders of S2 + 10%SiC in volume. The processability of the samples of each batch is investigated as a function of the energy given to the powders by the laser. Different properties have been evaluated of each sample, such as the density, the porosity, the types of defects, the melt pool depth, the microstructure or the hardness, aiming to find the combination of parameters that produce the best samples.

The microstructural characterization is performed using techniques like Optical Microscope (OM), Electron Backscattered Diffraction (EBSD) and Energy-dispersive X-ray spectroscopy (EDX) under Scanning Electron Microscope (SEM) and reversed Differential Thermal Analysis (DTA). This way the evolution of the microstructure during the printing process can be discussed. Also, the effect of the preheating and the SiC is identified.

2 STATE OF THE ART

2.1 Additive Manufacturing (AM)

Additive Manufacturing (AM), also known as 3D Printing, is one of the engineering technologies gaining more importance in the last years. It was first developed in the late 1980s and it is defined as:

Group of fabrication technologies that using the superposition of layers are capable of creating 3D objects. Depending on how the material is deposited, different 3D Printing technologies can be distinguished. [6]

This technology is being extensively investigated due to its potential as a complementary fabrication technique. Thus, it is not a technology to substitute traditional fabrication techniques, such as machining or injection moulding, but a complementary one. There are usually two situations in which AM is better than traditional techniques: when the number of parts is low, or when the complexity of these parts is high. The reason for this is that the unitary cost of the parts printed with AM is the same regardless of the complexity or the number of parts. In other situations, other techniques can be considered [7].

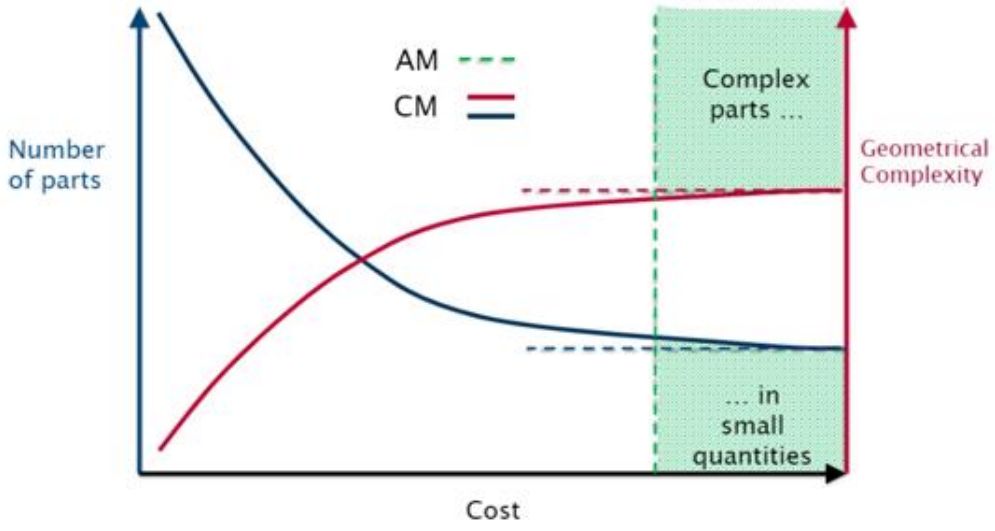

Figure 1. Evolution of the cost in objects produced by CM and AM as a function of the geometrical complexity and the number of parts [7]

The advantages and disadvantages of AM are summarized in Table 1.

Advantages	Disadvantages
Short time with small parts	Limited accuracy
Wide material range	Parts can be hard to clean due to remaining raw material or supports
High geometrical complexity achievable	Part dimension limited to printer size
Lighter parts	Usually need post-processes
Customization	

Table 1: Advantages and disadvantages of AM [7]

Among these points, one AM quality stands out. The capacity for customization is one of the main reasons why 3D printing is currently used in many applications, and it considers the possibility of building parts with specific complex shapes. For instance, in dental sector, AM have been used since 2002. More specifically, it has become a standard process for the production of crowns and bridges made of non-precious alloys. Although each unit can be of a different shape, a large number of them can be positioned in a single platform to reduce the production time and optimize the process [8].

As a summary, 3D printing is known for fabricating a wide range of structures and complex geometries from three-dimensional model data. It has been increasingly applied in different sectors due to its optimization in time, cost and overall limitations. Now, the technology can produce objects with less material waste, freedom of design and automation. These advantages along with the ability to create small quantities of complex, precise and customised products with low costs makes AM worth-considering [9].

However, depending on the specific characteristics that we need for the part there are 7 different methodologies to create 3D objects using AM:

- ✓ Extrusion: The material is selectively deposited layer by layer using a wire passing through nozzles. At the same time, the material is melted so later it solidifies together.
- ✓ Vat photopolymerization: A photoreactive liquid resin situated in a tray is selectively solidified when focused with an UV light.
- ✓ Powder bed fusion: Powders that melt or sinter together when focused with an energy source.
- ✓ Material jetting: Droplets of raw material are selectively dropped in a platform to form the object layer by layer.
- ✓ Binder jetting: Powders that are sticked together using binder instead of an energy source, thus avoiding internal thermal stresses.

- ✓ Sheet lamination: Material sheets built one above the other.
- ✓ Direct energy deposition: The material as powder or wire is melted with a focused energy source as it is deposited on the surface. [10]–[12]

In each category there are also different technologies depending on factors such as the energy source. In Vat photopolymerization the resin can be cured with a laser (SLA), a projector (DLP) or a LED plus oxygen (CDLP). In Powder bed fusion technologies, the energy source to fuse the powders can be either an agent plus a laser (MJF), a laser (SLS/SLM) or an electron beam (EBM). Regarding Material jetting, the energy to cure can be UV light (MJ), heat (NPJ) or milled plus heat (DOD). Finally, in Direct energy deposition a laser (LENS) or an electron beam (EBAM) can be used [13]. Therefore, fifteen different technologies are available (Figure 2).

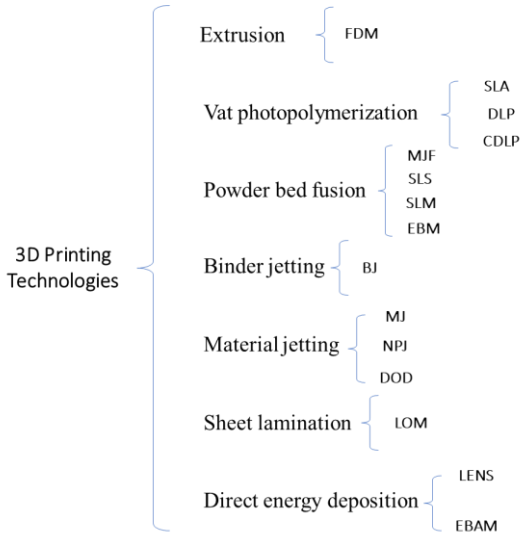

Figure 2. 3D printing technologies [10]

This study is focused on Laser Powder Bed Fusion (LPBF) technology using a laser as energy source responsible for the merging of the powders.

2.1.1 Laser Powder Bed Fusion

2.1.1.1 Process mechanism

The process followed to create an object using AM is the same regardless of the technology. A 3D CAD model needs to be created using a computer program so a .STL file can be obtained. A slicing software slices the model into hundreds of thin layers. Each layer corresponds to the 2D shape of one

section. Later, it exports all the data of 2D sections in a G-code that is the language the printer is able to understand. The part is printed layer by layer [14].

Figure 3. Steps of the 3D printing process [15]

Specifically, LPBF uses a laser beam that selectively melts powder that solidifies assembled. Then, another layer of powder is spread on top of the previous one using a platform that goes down and a roller. The process is repeated multiple times until all the layers of the object are printed, as it is shown in Figure 4.

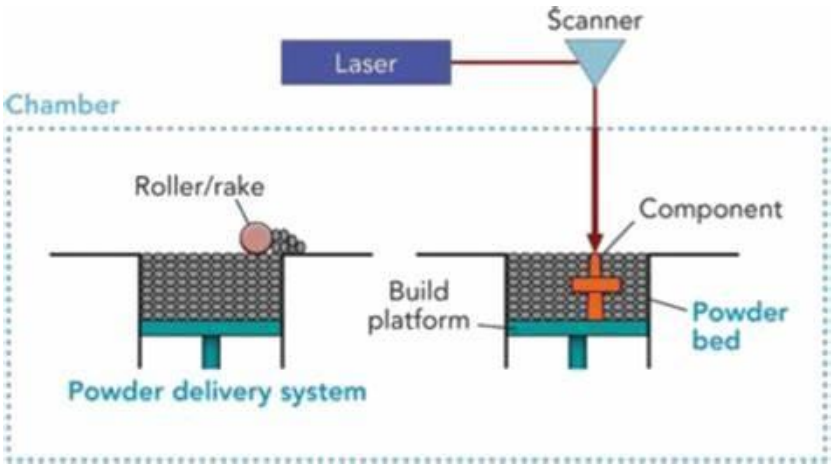

Figure 4. LPBF working principle [16]

Among different advantages of this technology stands out the wide range of materials that can be used. The technology accepts raw material in powder form that can go from polymers, metals and ceramics to even composites, as long as the powders are created correctly. Furthermore, inside these material types, LPBF cover materials with high or low melting point, making the technology useful for many materials. [17]

The typical general features of these technology can be summarized as follow:

Maximum building volume	630x400x500
Layer thickness	30-60 µm
Powder Size	20-60 µm
Minimum wall thickness	0,2 mm
Accuracy	0,1%
Porosity	0,5 – 2%
Rugosity (Ra)	7 – 15 µm

Table 2. General features of LPBF [7]

Moreover, it is commonly known that LPBF significantly overcomes the design limitations of traditional methods. As can be deduced from the values of Table 2, complex and dense (density > 99,9%) parts can be printed with high mechanical properties. [18]

Nevertheless, the technology also comes with several drawbacks that must be considered. Apart from the problems related to the cleaning and production of powders, LPBF goes along with internal stresses due to thermal gradients and physical defects such as porosities or spatters that depend highly on the initial parameters [19]. These effects and, consequently, parameters will have a huge impact on the final properties of the parts [20], as will be discussed in section 2.1.1.3. Because even though the technology could seem like it is based on a relatively simple working principle, there are a lot of variables that can influence the quality of the parts.

2.1.1.2 Process parameters

There are over 150 parameters influencing the LPBF process. The most influential ones, and the ones the user have control over, include laser power, layer thickness, laser scan velocity, distance between successive laser passes (or hatch distance) and atmospheric chamber gas and pressure [21]. The optimal parameters will result in dense parts with minimum defects and surface roughness. However, the optimal depends on the material, the shape, whether or not there are thin walls… [22]

There is an optimization metric for LPBF process parameters, though, that takes the four major influential parameters into consideration [23]. The concept is known as the “Volumetric Energy Density (VED)” and is defined as the laser beam energy transmitted to a volumetric unit of powder material. The empirical formula of VED is [24]:

$$VED = \frac{P}{Vs * Dh * t} \left[J/mm^3 \right]$$

Where P is the laser power $[W]$, Vs is the scan speed $[mm/s]$, Dh is the hatching distance $[mm]$ and t is the layer thickness $[mm]$. The VED will have a direct impact on the size, shape, temperature, cooling rates within and near the melt pool and, therefore, on the final characteristics and quality of the part [24]. Then, it goes without saying that controlling the power, scan speed, hatching distance and layer thickness is mandatory and knowing the VED of a sample, a lot of what is happening during the printing process can be understood.

Another factor that affects the quality of the final part is the scanning strategy, as it is essential in the formation of a desired microstructure. Increasing the scanning vector can result in an increase in the residual stresses [25]. In short, the scan strategy affects the heat transfer, powders melting, solidification and, consequently, the microstructure and defects [26]. There are different scan strategies, as it can be seen in Figure 5.

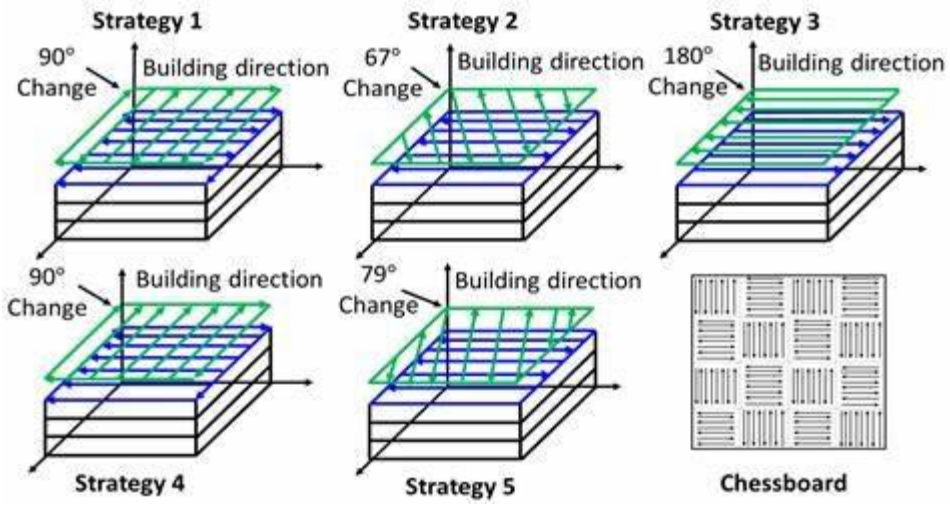

Figure 5. Scan strategies in LPBF [27]

Among them, the most typical is Strategy 1 because it allows to better balance the laser energy input in the whole layers, which prevents defects accumulation and propagation [26].

2.1.1.3 Defects in LPBF

The most typical defects in LPBF are porosities. Even though the technology is known for the printing of high-density specimens (>99%), and thus low porosity, it is inevitable to have some

porosities even in the best samples. Having highly porous samples is a problem since porosity can easily turn into cracks [28].

To understand how porosities are created it is important to first talk about the melt pool. It is basically the zone of powders being melted with the laser. The size of this melt pool will be critical in the processability of the parts and can be related to the VED. It will not only affect the zone being melted at a certain moment, but also will transfer heat to previous layers and will act as an internal thermal treatment during the printing [29]. Furthermore, if the size is too big (meaning too high VED), it will remelt previous layers. This remelting is normal until a certain point to ensure good adhesion, but if the portion is too large the energy costs increase. On the other hand, if it is too small (meaning too low VED) there will be lack-of-fusion problems since some of the powders will not be melted.

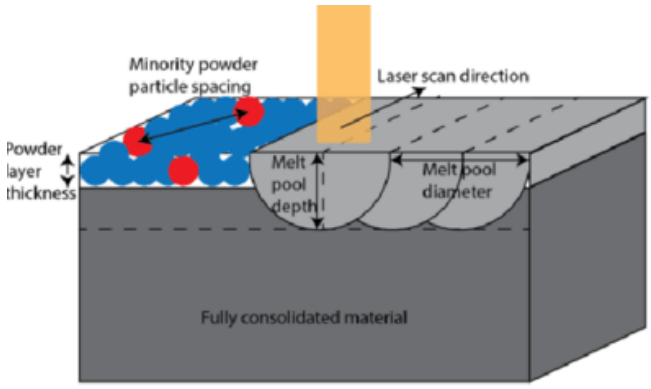

Figure 6. Melt pool in LPBF [30]

There are three main reasons for the occurrence of porosities. The first one is the so-called gas porosities. This kind of pores are easy to identify for their small size, typically less than 100 µm, and spherical shape. The formation is due to the gas present between powder particles, that may be dissolved in the molten pool if the packing density is low e.g., fifty percent. Because of the high cooling rate, the dissolved gas cannot come out of the melt pool before solidification and remain in the fabricated part. Besides, Gong et al [31] attribute this formation to vaporization of low melting point constituents within an alloy [32]. This type of porosities appear frequent since are not easy to control.

Secondly, there is also the Lack Of Fusion (LOF) porosities. These are mainly due to lack of energy input during the printing. The formation of LOF is because the powders are not fully melted to deposit a new layer on the previous one with a sufficient overlap [33]. If the laser energy input is low, the melt pool width will be small and not all the powders will be melted [32]. LOF defects are characterized for being bigger than the other types of porosities and having an irregular non-spherical shape.

Furthermore, keyhole porosities can also be detected in LPBF. These defects are more or less spherically shaped. The sphericity, though, usually is not as perfect as gas porosities. Keyhole porosities can be identified for being a little bit bigger than gas porosities, having the shape of a sphere or a cut sphere, like an hemisphere, and being situated on the lower part of the melt pools, as it is shown in Figure 7b. These pores are caused by excessively high laser energy input leading to inclusion of evaporated metal by the surrounding melt during solidification [34].

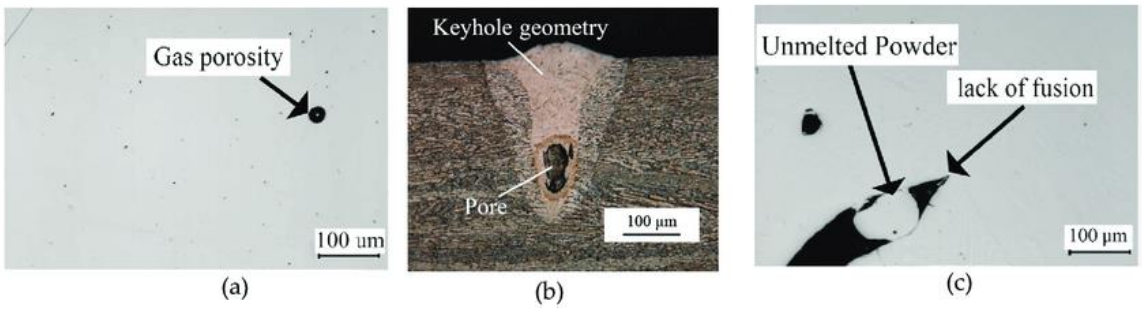

Figure 7. Types of defects in LPBF. a) Gas porosity b) Keyhole porosity c) Lack of fusion [35]

However, there is the possibility of doing some post-treatments in order to close these pores. Hot Isostatic Pressing (HIP), for example, is used to increase the density, closing the pores by applying pressure and a thermal treatment simultaneously. This allows the diffusion of elements and the formation of more homogeneous materials [36].

Another common defect is due to the balling effect. This problem affects the surface precision of the melted part. It is mainly due to the large surface tension, that can also be related to the initial parameters. The liquid phase sintering line is broken into spherical protrusions. In metals, because of the high surface tension due to the higher energy needed, this effect is more notorious so must be considered [37]. Not only does it affect the rugosity and surface uniformity but also the density of the parts [38], because it affects the spreadability of the subsequent layer which generates non-uniform powder beds. This problem is intensified when the structures resulting from balling exceeds the consecutive layer thickness. It can cause wear in the blade resulting in non-uniform powder distributions [39].

The initial parameters that can induce to balling effect are too high or too low scan speed and laser power. When it comes to laser power, if it is too high there will be evaporation and splashing of the liquid during the melting generating pores. There will be a steep temperature gradient between the center and the surface resulting in Marangoni effect. Consequently, the melt will flow radially to the center of the melt pool instead of outwards on the surface below. On the other hand, if the laser power is too low the sintering temperature will also decrease, resulting in a reduction of liquid amount. This

will rearrange the liquid flow and will, thus, create a tendency for the molten material to aggregate into a single coarsening sphere, whose diameter is approximately the same of the laser beam. Furthermore, considering the scan speed, a high speed can also induce the balling effect, since the melt droplet will be easier to splash. With high scan speed the molten sintering track is short so it is highly unstable. In order to obtain the equilibrium state, the surface energy will decrease continuously and this reduction causes small liquid droplets splashing from the surface. Besides, a slow laser scan speed would lead to excessive liquid. Due to this large melt pool, the powder particles around would be sucked into the pool and the next scan track would have a shortage of powders [40].

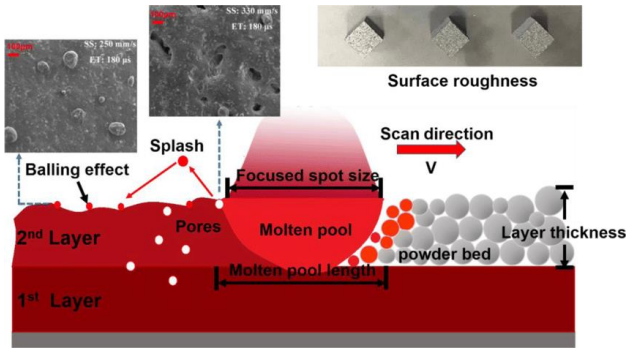

Figure 8. Graphical representation of balling effect [40]

Finally, another typical defect in LPBF is spattering [41]. This phenomenon destroys the initial powder bed conditions and breaks the uniformity of the melt tracks leading to balling, pores and rough surfaces. Experimental studies have shown that spattering is equally or even more influential over the melting process than the spreading procedure itself [42]. Five different types of spatters have been detected. Solid spatter is formed due to intense vapour jet that ejects unmelted powders out of the powder bed. Metallic jet spatter is caused by the intense metallic vapor from the laser heating process. Powder agglomeration spatter is due to coalescing of multiple powders or spatters. Entrainment melting spatter is the melting and ejection of entrained powders. Last, defect induced spatter is induced by the previous layer's large defects [43].

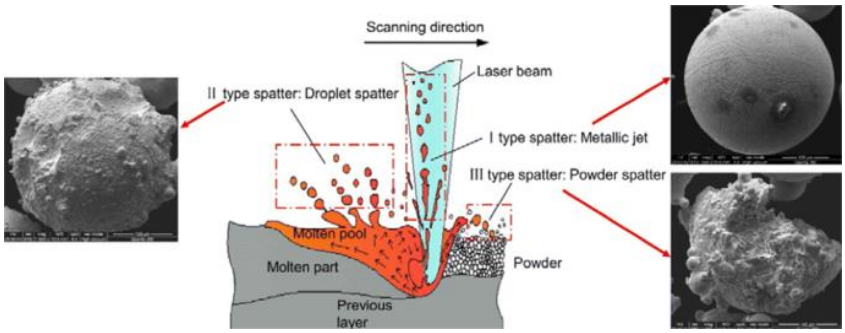

Figure 9. Spattering in LPBF showing types of spatter 1) metallic jet 2) droplet spatter 3) powder spatter [44]

Summarizing, the defects in LPBF influence the final quality of the samples and, therefore, the mechanical properties. The majority of these defects affect the density measurements, which is critical in the likelihood of cracks appearing. In short, in order to obtain crack-free parts the optimal initial parameters must be evaluated in terms of volumetric energy density and the morphology and size of the powders. Depending on the material, the optimal can be shifted, since the absorptivity and melting point will not be the same.

2.2 Raw materials for LPBF

The material used in LPBF must be in form of powders. A component fabricated with this technology may contain thousands of finely spread powder layers. The uniformity of these layers affects the quality of the final component so the way that the powders spread and flow is critical [45] [46]. Therefore, before the printing of a sample is important to make sure that the powder feedstock is adequate and suits with the final quality that is wanted.

2.2.1 Powders production

There are three typical production routes for general powders: mechanical, spray or atomization and chemical route. Among these three, the most used one is atomization by far, for his better results. It is described as a method by which a liquid or flow is broken up into fine droplets of dry powder by the stream of a hot gas [47]. The melt is shearing due to the high-velocity gas/water/plasma jets. Therefore, atomization processes are respectively divided into gas/water/plasma atomization [48].

The most significant difference between the methods is the sphericity obtained along with the particle size distribution. With plasma atomization the particles obtained are extremely spherical but, of course, it is the most expensive method. Gas atomization is available for a wide range of alloys, even the reactive ones, and spherical particles are obtained (less spherical than plasma atomization but more than water atomization). The cost is lower than plasma atomization. Finally, water atomization

is the most used due to its lower cost and spherical enough particles [45]. The working principle and characteristics of each method are discussed below.

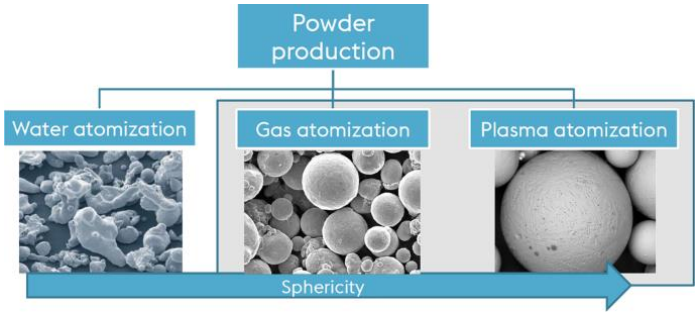

Figure 10. Powders morphology of the different atomization methods [49]

Gas atomization is the conversion of a molten metal into aerosol particles, thanks to inert gas jets, that cool down during the fall in the atomizing tower. It is used to produce controlled particle sizes using the surface tension to break up the free-falling melt-stream. The result is particles with the already-mentioned perfect sphericity combined with smooth surfaces and high cleanliness level [50].

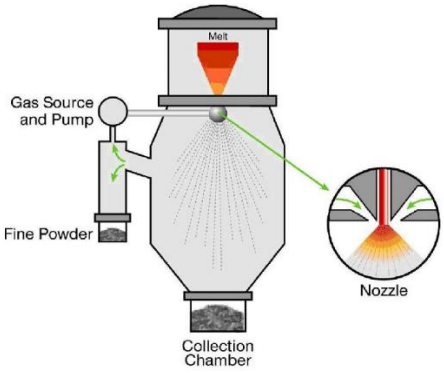

Figure 11. Gas atomization working principle [51]

Regarding water atomization, it is the most used technique to produce powders, as it has been mentioned. The main uses for them, though, are the press and sintered powder metallurgy automotive parts and the Metal Injection Moulding (MIM) industry. The method consists in a metal stream disintegrated with high pressure water. Since the metal is cooled quicker, the droplets do not have time to become spherical, so the shape is more irregular [52].

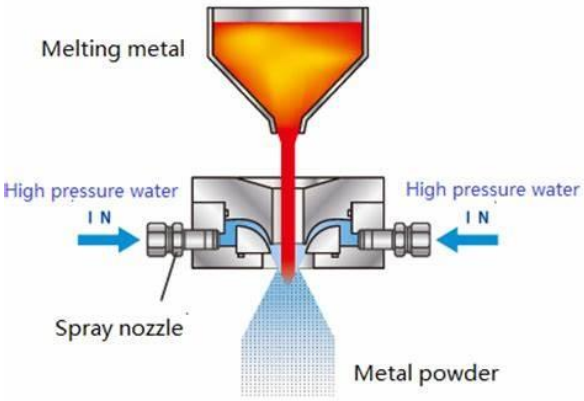

Figure 12. Water atomization working principle [53]

Plasma atomization, however, is a technique where powder or a wire is fed into high energy plasma. Due to this high energy, the material melts immediately. Then, it is necessary to remove residual material cleaning the powders in a separate post process in order to get the highly spherical powder [49]. This technique is more expensive than the previous ones so it is usually used to produce high quality powders. For this reason, plasma atomization feedstock is usually expensive metals such as titanium alloys [54].

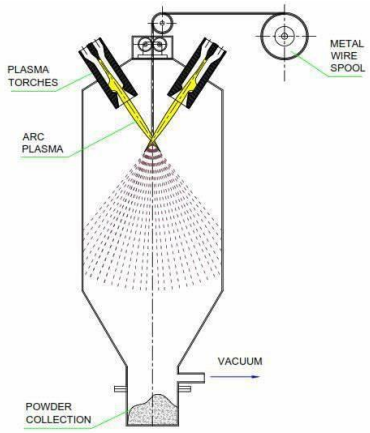

Figure 13. Plasma atomization working principle [55]

It has been seen, then, that depending on the application, the material and the quality needed for the parts it is important to choose wisely the production technique for the powders in LPBF. The sphericity and the size of the powders used affect directly the flowability and the uniformity of the layers so the production methodology must be premeditated.

2.2.2 Composition modification by mechanical alloying

There are many materials or composites whose viability with AM has not been tried yet. In terms of LPBF, in order to produce and study new materials or composites researchers need the proper powder feedstock. The problem is that the market of powder for AM is relatively small, since there is not a lot of demand. The most used materials are easy to get from different suppliers but for less typical materials, the situation changes.

This lack of raw material means that researchers usually need to produce the powders to create new alloys themselves. Starting from elemental powders produced by atomization from different materials, the user mixes them obtaining powders to print composites with different percentages of each material. In-situ alloying of blended powder mixtures during LPBF speeds up the alloy development as it allows quick composition adjustment. Normally, then, pre-alloyed powders are used in industrial settings to ensure consistency whereas blended powders are used to experiment with new alloy compositions [56]. ´

However, this mixture can be done using different techniques that will also influence the final properties. The most typical methods to alloy different powders are the ones under the name of mechanical alloying (MA). This is a generic term for processing metal powders in high-energy mills. If the pre-alloyed powders are milled in a high-energy mill and material transfer is not required for homogenization, the process is more accurately called mechanical milling (MM) [57]

Among alloying procedures ball milling stands out. It is a technique not only used as an alloying method but also as a method to produce powders. In the second field, though, it is not as good as atomization methods. It produces non-spherical particles that result in poor rheological properties [58]. On the other hand, this technique is useful to mix different powders homogeneously.

Ball milling is a type of grinder used to grind or blend materials. It works on the principle of impact and attrition. The mill consists in a hollow cylindrical shell rotating about its axis. Inside, both the powders and a certain number of balls are placed. As the shell rotates, the balls are lifted up on the rising side and they cascade down. Therefore, the powders are reduced in size and mixed at the same time [59].

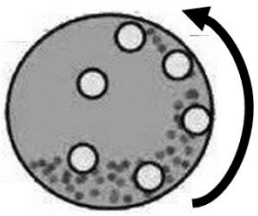

Figure 14. Ball milling working principle [60]

Nevertheless, it must be considered that milling powders can promote the agglomeration of the particles. Naturally fine particles in the micron size range are usually so cohesive that they cannot exist alone and tend to form clusters. Even though milling them can help break these clots, if the milling time is excessively high it can provoke a reagglomeration. Indeed, if the powders are subjected to vibration the clumping of powders can occur even with no binder or external agent [61].

2.2.3 Rheological properties

The uniformity of the layers spread in AM is critical to ensure the best final quality of the samples. This is why rheological properties in 3D printing are such an important parameter to control, because they are directly related to the good spreadability of the layers. How the powder flows and packs as the layers are formed are defining aspects of this performance [62].

Rheology is the study of the relationship between a force and the deformation suffered [63]. When it comes to fluids or powders that together act as a fluid, it is the science of fluid flow, studying the behaviour of plastic and non-Newtonian fluids [64]. There are several properties of the powders that affect the rheological behaviour of the powders.

- Particle size

Particle size distribution (PSD) is identified as the main influence on the rheological behaviour. It affects the laser melting efficiency. Large particles require more energy to be melted and usually reduce the pack density of the powder bed whereas small particles tend to agglomerate, making powder layering more difficult [65]. Having small particles in between larger ones reduce the rheological index, also increasing the density. PSD is known to have an impact on the forces acting on particles during powder flow. This is due to the drag forces acting on particles, such as gravity [66]. On the other hand, there are several studies that confirm that a wider PSD increases the packing density but decreases the powders flowability; coarse particles have a better flowability than their fine counterparts. Despite this, flowability is not the only thing that must be considered since coarser particles also worsen the density and surface finish [67].

In short, narrower PSDs, larger particles and decrease moisture content increase flowability, something interesting to maintain the uniformity of the layers in LPBF. Also, higher density correlates with wider PSDs and smaller particles due to small particles positioning in between larger ones. When it comes to mechanical properties, narrower PSDs improve them. However, there are studies that do not fit with these aspects since they are relative changes that require compromises. For instance, fine particles with a narrow PSD, expected to have good density due to the small particles and high mechanical properties due to the narrow PSDs, may in fact have poor density and properties because of the decreased flowability [68].

- Morphology

With an influence on the rheological behaviour similar to the size, the shape of the particles is also critical. The shape can be mainly controlled by the production route, as seen in section 2.2.1. It affects technological properties such as bulk density, flowability or surface area that influence the final part quality. The preferable shape is, indeed, spherical since it improves the flowability, optimal conditions for melting, density and overall uniformity of the samples [69].

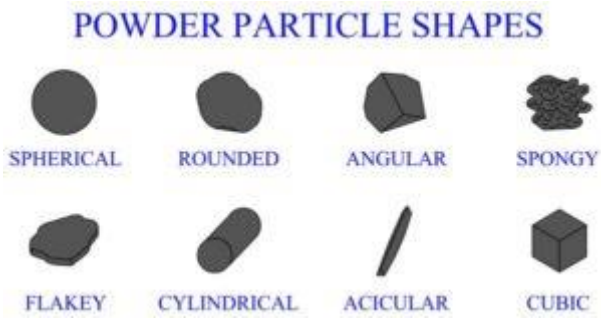

Figure 15. Powder particle shapes [70]

In order to characterize the particle morphology and approach the type of particle, different shape factors are calculated. These are the ellipticity, elongation, dispersion, roundness and particle angularity [69].

It is also worth noting that a spherical particle may appear smooth at first but with many protuberances when observed at higher magnifications. In this aspect, though, atomized particles usually have fine surface roughness. Surface topography is important for its influence on frictional forces, that can be related to flowability, settling and compaction of the bulk [71].

Furthermore, it has to be mentioned that the morphology of the powders is highly affected by whether or not the powders are recycled. If it is not the first time that the powders have been used, they might have lost some sphericity or worsen surface roughness due to contamination, frictions…

- Bulk density

The bulk density is the ratio of mass of an untapped powder sample and the volume including the void volume between particles. Hence, the bulk density is a function of both the particle density itself and the amount of void space in the bed, so the arrangement of the powders. This measurement is dependent upon the preparation, treatment and storage of the sample. Because of this, bulk density can vary easily with the slightest change, that can make the powders pack and rearrange. It is, then, a volatile measurement difficult to measure with good reproducibility [72].

The density obtained by dividing the mass by the initial volume of powder is known as the initial bulk density. If the mass is divided by the volume of the shaken or tapped powder bed, we obtain the tapped density or packing density. This is an indicator of the flow properties and is used to calculate Hausner ratio and Carr's index. The first one affirmed that depending on the value of this ratio we have free-flowing particles with low friction between them (Hausner ratio < 1.2) or more cohesive particles (Hausner ratio > 1.5). On the other hand, Carr's index is an indicator of the compressibility of the powders. It is a measure of the tendency for bridge formation and an indirect measure of flowability. It correlates the initial bulk density with the tapped density according to the following equation [73]:

$$\%\text{Compressibility (Carr}'s\text{ index)} = \frac{\rho_n - \rho_0}{\rho_n}\ x\ 100$$

Where ρ_n is the tap density and ρ_0 is the initial bulk density [71].

- Spreadability

Creating a highly dense powder layer before laser scanning is a must for producing non-porous parts on LPBF. The ability of the powders to uniformly spread and flow is a function of other powder characteristics such as PSD or morphology [74]. However, it is also dependent on external factors such as humidity, temperature and consolidation history. The large number of factors influencing flowability makes difficult to approach an accurate and repeatable quantification [75]. Numerical studies are performed with further experimental validation such as measuring the angle of repose (AOR) or avalanche angle. The first one is defined as the angle with the horizontal plane that the static powders will create after being released from an orifice under gravity. In contrast, the avalanche angle is the angle that the powders will dynamically create with the horizontal when being rotated with a drum [74].

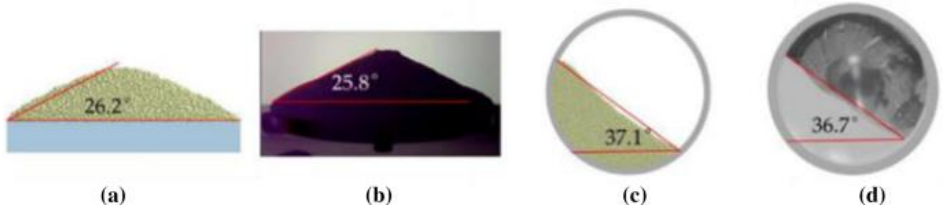

Figure 16. Numerical methods to simulate powder performance in terms of a) AOR c) angle of avalanche and its experimental validation of b) AOR d) angle of avalanche [74]

The spreadability can be classified as a function of the AOR:

AOR	Flow properties
20° < α < 30°	Very free-flowing
30° < α < 38°	Free flowing
38° < α < 45°	Fair to passable flow
45° < α < 55°	Cohesive
55° < α < 70°	Very cohesive

Table 3. Flow properties of powders as a function of AOR [76]

2.3 Tool steels by LPBF

Generally, steels can be classified as carbon steels (basically Fe and C) and alloyed steels (steels with a significant amount of alloying elements able to modify certain properties) [77]. On the one hand, carbon steels are divided by its carbon content. On the other, alloy steels are classified depending on the percentage of alloying elements. Among high carbon steels and high alloy steels we find a group named tool steels.

Tool steels are used to make tools such as drills, dies, cutting tools… They have these applications because of their good hardness, wear resistance and high temperature softening. These kind of steels are usually alloyed with vanadium (V), chromium (Cr), molybdenum (Mo) and tungsten (W). Usually, tool steels also require a heat treatment in order to achieve a hard matrix and provide the desired hot hardness and wear resistance [78].

In terms of tooling applications, LPBF enables to create features such as internal cooling channels that can be implemented in cutting or shaping tools. This is interesting because higher cutting speeds are feasible thanks to the more efficient cooling unachievable with CM [79]. Tool steels, however, are known for having a difficult processability. They are likely to end up with cracks or even to break during printing. Because of these difficulties, in LPBF tool steels are still a complicated topic. Nowadays, they are being increasingly studied in order to find the exact optimal parameters for each material and avoid defects. Moreover, researchers are focusing on finding techniques to reduce internal stresses that end up with cracks and on fully understanding what happens inside the samples during the process of printing.

2.3.1 Conventional Tool Steel

According to AISI designation, there are seven types of tool steels, as shown in Table 4.

Table 11.1. Designation of Tool Steels

Group	*Symbol*	*Type*
Water-hardening Tool steels	W	
Shock-resisting Tool steels	S	
Mould steels	P	P1-P19 low carbon types P20-P39 other types
Cold-work Tool steels	O	Oil-hardening
	A	Medium-alloy air-hardening
	D	High-carbon high chromium
Hot-work Tool steels	H	H1-H19 Chromium types H20-H39 Tungsten types H40-H59 Molybdenum types
High-speed steels	T	Tungsten types
	M	Molybdenum types
Special-purpose steels	L	Low-alloy
	F	Carbon-tungsten

Table 4. Types of tool steels [80]

Among the tool steels available, only few of them are being processed by LPBF. The majority of studies are focused on M2 HSS, AISI H13 HSS, AISI M50, HS 6-5-8-3, FeCrMoVC and FeCrMoVWC [79]. In Table 5 a summary of tool steels found in literature and the outcome of their processability is shown.

Table 5. Processability outcomes and chemical compositions (in wt. %) of tool steels found in literature [79]

Refs.	Alloy	Processability	C	Si	Mn	Cr	Mo	V	Co	W	Fe
Buls and Humbeeck, 2014; Liu et al. (2011)	M2 HSS	Severe cracking Crack free with BP[1] at 473 K	0.9	0.35	0.38	3.97	4.89	1.82	–	6.15	Bal.
Saewe et al. (2020)	HS6–5-8–3	Severe cracking Crack free with BP at 773 K	1.31	0.5	0.3	4.0	4.7	2.9	8.5	6.4	Bal.
Saewe et al. (2019, 2018)	AISI M50	Severe cracking Crack free with BP at 773 K	0.83	0.2	0.25	4.0	4.3	1.05	–	–	Bal.
Yan et al. (2017)	AISI H13	Lower residual stresses with BP	0.41	1.12	0.41	5.20	1.23	1.10	–	–	Bal.
Beal et al. (2008)	AISI H13	Porosity Cracking	0.32–0.42	0.85–1.15	0.4	4.75–5.25	1.25–1.75	0.9–1.1	–	–	Bal.
Mertens et al. (2016)	AISI H13	Crack free and lower residual stresses with BP at 573 K	0.32–0.4	1.0	–	5.13–5.25	1.33–1.4	1.0	–	–	Bal.
Krell et al. (2018)	AISI H13	Cracking Crack free with BP at 573 K	0.39	1.0	0.3	4.9	1.2	1.0	–	–	Bal.
Narvan et al. (2019)	AISI H13	Cracking Crack free with BP at 573 K	0.39	1.08	0.40	5.27	1.34	0.97	–	–	Bal.
Sander et al. (2016)	Fe85Cr4Mo8V2C1	Crack – free with BP at 773 K	1	–	–	4	8	2	–	–	Bal.
Sander et al. (2017a, b)	Fe85Cr4Mo8V1C1	Crack – free with BP at 773 K	1	–	–	4	8	1	–	–	Bal.
Sander et al. (2017a)	FeCr4Mo1V1W8C1	Crack – free with BP at 773 K	1	–	–	4	1	1	–	8	Bal.
Platl et al. (2020a)	–	Severe cracking Porosity	0.85	0.53	0.36	4.25	2.72	2.01	4.35	2.46	Bal.

In those studies, several characteristics regarding the processability of tools steels by LPBF appeared. Tools steels in LPBF usually solidify as martensite, retained austenite and carbides due to their high carbon content and high cooling rates. Furthermore, this high cooling rates induce a fine microstructure, usually elongated grains in the building direction (direction of the heat flow) [79]. When the laser beam affects a certain zone of powders, it turns them into liquid, generating the melt pool and releasing heat. Without the focus of the laser, the primary solid phase, austenite, starts forming at the interface between the solid and liquid phases. It grows radially to the center of the melt pool. Because of the high cooling rates, the process does not stop there and transforms the austenite into martensite. However, in the boundaries of the melt pool there is a zone that will not reach martensite start temperature (Ms) and will remain as retained austenite [81].

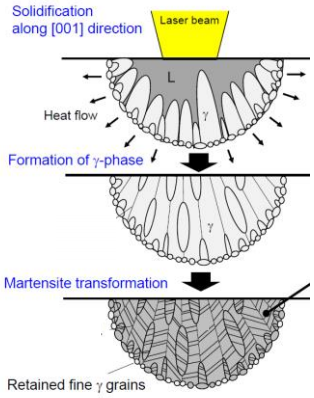

Figure 17. Evolution of the typical microstructure in the melt pool of tool steels [81]

Furthermore, it must be considered that the solidified layers can be affected by the melting of the next layers. The zones close to the melt pool can be remelted. At a certain distance to the melt pool there is a zone that might be heated up to temperatures above austenite transformation but below the melting point, causing the reaustenitisation of the martensite. Further distant from the melt pool, the heat will be just sufficient for tempering the martensite, i.e. for carbon partitioning and carbide precipitation. In short, in LPBF there is an internal thermal treatment occurring during the printing with the layers placed above a certain zone [78].

Taking a look at the studies presented in Table 5, in the case of M50 specimens, columnar dendritic grains due to epitaxial growth can be seen in the upper area. In the lower area, a martensite-dominated structure. In between the martensite needles, small fractions of retained austenite are visible [82].

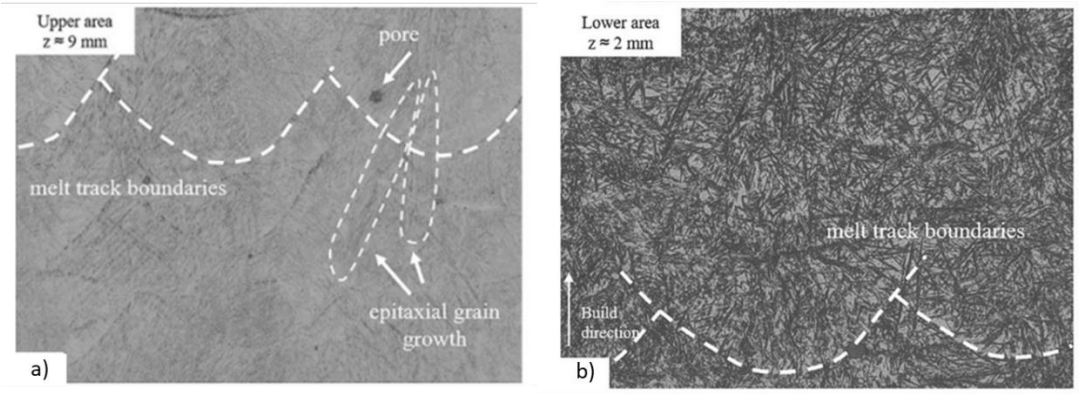

Figure 18. M50 etched cross sections with VED of 70 J/mm3 at a) z = 9mm b) z = 2mm [82]

Similarly, the study of J. J. Yan *et al.*, "Selective laser melting of H13: microstructure and residual stress," [83], distinguished α-Fe phase, cementite, martensite and retained austenite in as-built samples of H13. In this particular case, AM high cooling rates enabled the formation of martensite but also its partial decomposition into ferrite and cementite, owing to different cooling rates throughout the sample and to cyclic thermal effects from successive layers [83].

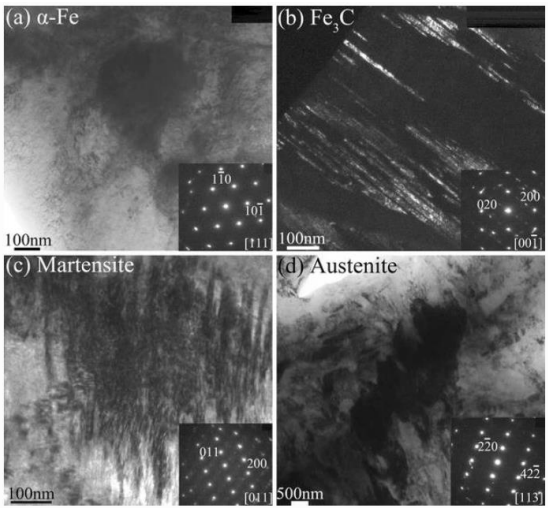

Figure 19. Major phases observed in H13 samples: a) α-phase b) cementite c) martensite d) retained austenite [83]

In the Fe85Cr4Mo8V2C tool steel, a fine microstructure with homogeneously distributed alloying elements was obtained. Figure 20 depicts again a needle-shaped phase. In image a) the epitaxial growth of needle-shaped martensite is visible. Depending on the position of the melt track, the size and phase is different. Looking at (Figure 20b), in the center of the melt tracks dendritic long needle-shaped austenite and martensite grains show up. However, the austenite and martensite grains are globular at the boundaries of melt tracks.

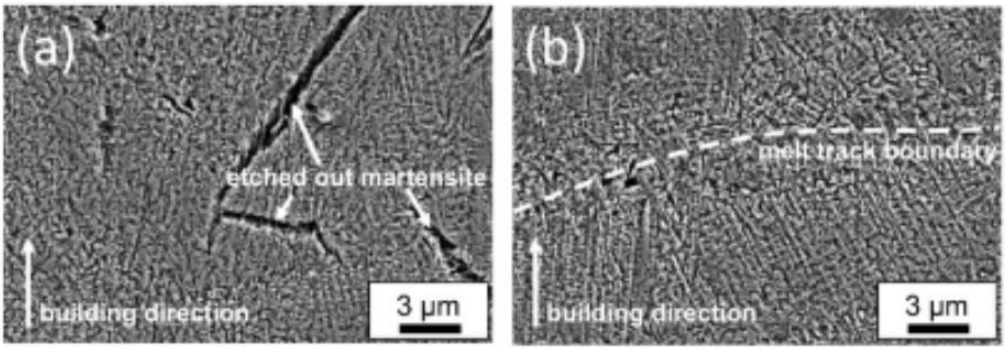

Figure 20. SEM images of Fe85Cr4Mo8V2C with a) VED = 89.3 J/mm3 b) VED = 129.6 J/mm3 [84]

On the other hand, most of the tool steels produced by LPBF present cracks if the baseplate is not preheated. M2 HSS showed cracking, delamination and distortion as a result of high thermal stresses along with a high carbon content, which in LPBF is known for producing defects. This could be avoided by using a preheating baseplate that reduces the thermal gradient, thus the internal stresses, inside the part [85].

Figure 21. M2 HSS parts with preheating temperatures of 90ºC (left), 150ºC (middle) and 200ºC (right) [85]

Similarly, when studying M50 and HS6-5-8-3 cracks were observed. That could be avoided with a baseplate preheating of 773 K [79]. This is due to the fact that LPBF fabricates metal parts in out-of-equilibrium conditions, with temperatures above the melting point and rapid solidification rates. This result in tool steels with microstructural and chemical inhomogeneity inside the parts that usually comes with a brittle martensitic phase susceptible to cracking [1].

Furthermore, tool steels have a complex chemical composition with high carbon content. Carbon can segregate to the melt surface reducing the wettability. This effect combined with the thermal gradient involved in the manufacturing process result in high internal stresses and cracking [78].

In fact, there are many studies focusing on the effect of carbon content in the processability of samples in LPBF. All of them arrive to the conclusion that carbon increase the likelihood of having cracks.

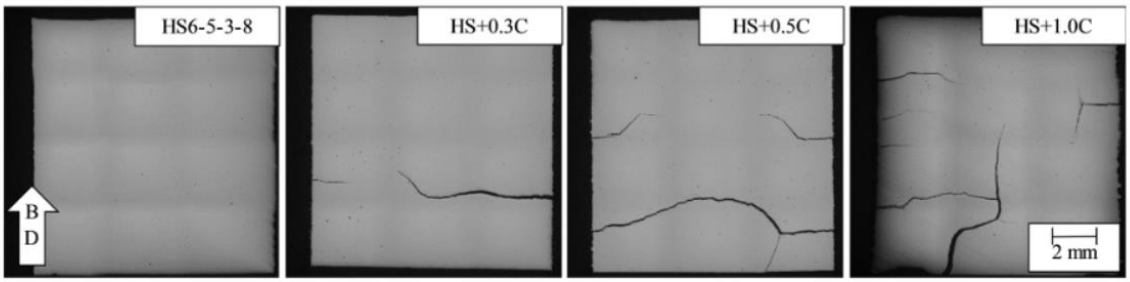

Figure 22. Influence of increasing carbon content on crack appearances [5]

In one of these investigations, for example, high-speed steel HS6-5-3-8 blended with different amount of carbon powder is produced with LPBF (see Figure 22). Increasing the carbon content, the cracks quantity also increases. According to the study, even though the martensite formation is suppressed with the carbon content, which is beneficial on avoiding cracks, these still appear. Therefore, it is concluded that martensite formation is not the only source for cracking. High stresses also appear due to high content of carbides which lead to embrittlement at grain boundaries and can promote crack formation [5].

Apart from the embrittlement due to carbide formation, carbon content also leads to cracks due to the increase of porosities. Indeed, the more porosity of a sample, the more tendency to develop cracks. In the section Defects in LPBF it was seen that porosity could be related to VED. However, some studies have been able to relate porosity also to carbon content [4].

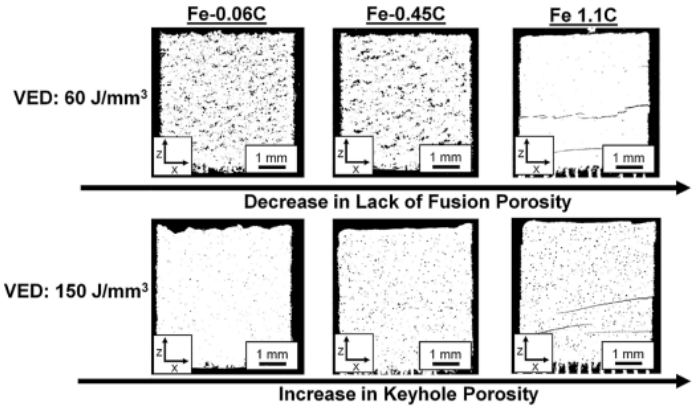

Figure 23. Influence of C in samples 60 J/mm3 and 150 J/mm3 [4]

Increasing carbon content reduces the lack of fusion porosity. According to the study, it is due to an improved wettability and flow of the melt pool. It also increases keyhole porosity because adding carbon reduces the melting temperature so the melt pool increases [4].

Summarizing, tool steels in LPBF are difficult to process because of the cracking tendency. The carbon content and intrinsic properties along with high cooling rates end up with high internal stresses that lead to cracks. In order to print this kind of steels, researchers use the preheating of the baseplate so as to reduce the internal thermal gradient that lead to internal stresses. This solution can produce crack-free samples, depending on the situation, with compositions and initial parameters that would produce cracks if no preheating was applied [5].

In general, the addition of a preheated baseplate can change most of the characteristics, from mechanical properties to the microstructure. Depending on the preheating temperature the effects change. When it comes to the density, for instance, higher preheating temperatures lead to higher values of relative densities even though the optimal process window shift towards lower VED. This is due to the additional energy input coming from the base plate. It provides extra energy to the powders, so the energy needed from the laser is less [86].

Comparing different preheating temperatures reveal that microstructure and melt track boundaries also differ from one another. At low preheating temperatures, long needle-shaped lancets tend to form within grain boundaries. Columnar dendritic structures can also be seen, indicating an epitaxial growth during the printing where grains grow in the direction of the thermal gradient through the melt pool. Increasing the preheating temperature up to 500ºC the microstructure becomes more fine-grained and homogeneous. If it is increased even more, larger grains are present in the center of the melt pool [87]. This can be seen in Figure 24.

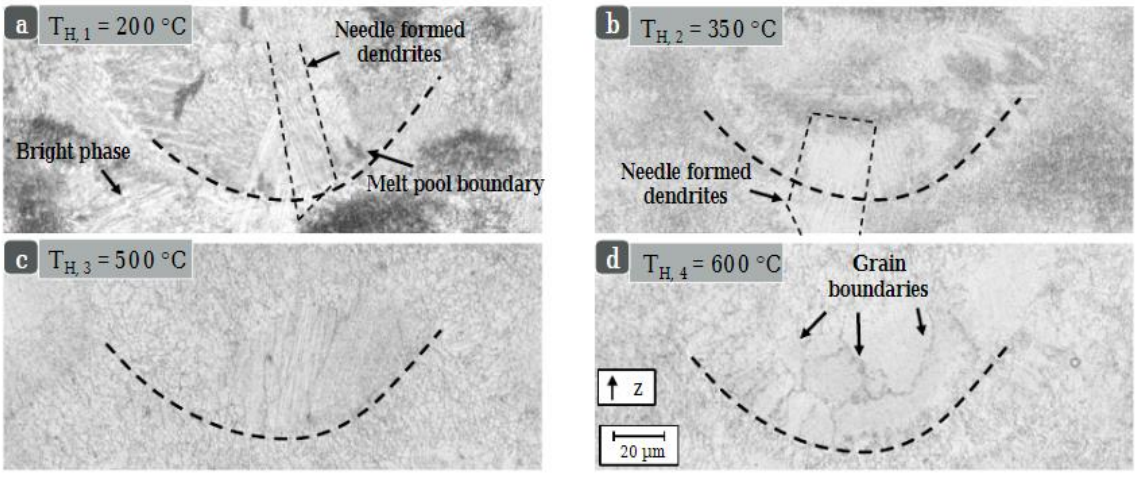

Figure 24. LOM of etched HS6-5-3-8 cross-sections at different preheating temperatures [87]

Regarding the hardness, the most influential factor is the martensite in the sample. As mentioned, tool steels solidify as martensite plus retained austenite. However, with the in-situ thermal treatment happening during the printing process the martensite characteristics can be modified. With the

addition of preheating temperature, a relation between the temperature and the hardness can be found. The temperature act as an in-situ tempering of the martensite, so the final properties are derived from the tempering diagram of the specimen's material. A maximum hardness value can be reached with preheating but if the preheating temperature is too high, it softens the martensite decreasing its hardness [87].

2.3.2 Modified Tool Steel

Nowadays, researchers have been focusing on the development of new alloys by LPBF, thanks to the modification of conventional tool steels with the addition of reinforcements, such as nanoparticles. Using in-situ alloying methods is cost-effective and offers great opportunities to produce non-conventional alloys [2]. More specifically, Metal Matrix Composites (MMCs) have been receiving increasing attention due to the enhanced properties, such as specific strength. A lot of different reinforcements can be used; carbides (TiC, B_4C, SiC, WC), oxides (ZrO_2, Fe_3O_4, Al_2O_3), nitrides (ZrN, Si_3N_4, TiN), borides (TiB, ZrB_2, TiB_2, WB) and different carbon forms (graphite, carbon nanotubes, graphene) [88]. However, there is an increasing interest on the ceramic Silicon Carbide (SiC) as reinforcing agent for different Fe-based tool steels. Indeed, SiC presents high hardness, wear resistance and capacity to retain its strength at high temperature maintaining good toughness, creep properties and fatigue strength [89]. The problem is that SiC at high temperature has a strong reactivity with most of the transition metals even in solid state [90].

Processing a mixture of Fe and SiC by LPBF leads to the decomposition of SiC particles and there is a modification in the structure [91]. This decomposition of SiC is deleterious for strength properties, although the modification of the matrix by Si and C might bring positive properties such as solid solution strengthening [90]. Also, the addition of this ceramic increases the laser absorptivity of the matrix, which has and important influence on the LPBF formation quality. In addition, it can improve melt pool stability and the viscosity of the liquid phase, which led to enhanced mechanical properties. Finally, in situ exothermic reactions between ceramics and metals increase the temperature and therefore can increase the density [89].

Depending on the study realized, the material used in the matrix and, of course, the percentage in volume of SiC the final results and effects of this reinforcing agent might change. For instance, the study [89], showed that when the addition was 15 vol% or higher in the C300 MS matrix there were visible defects such as cracks and large pores. The main reason is the change in the thermal conductivity of the sample due to SiC, which lead to an increase of residual stress with the same VED [89]. This is why depending on the percentage of each material in a MMCs the processing parameters must be well-optimised [3].

Besides, a significant influence on the microstructure was detected. With the addition of SiC the microstructure turned from cellular to dendritic as the percentage of SiC increased due to reduced temperature gradient and higher solidification rate. Massive nanoprecipitates were observed in as-fabricated MMCs without the necessity of a post thermal treatment. It could have been an in-situ process via the SiC particles and dislocations acting as preferential nucleation sites [89].

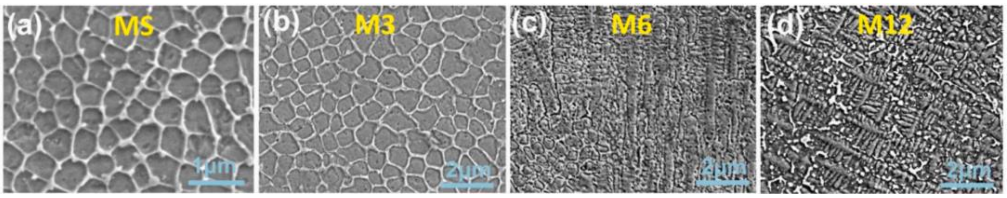

Figure 25. SEM microstructure of samples with a) 0 vol% SiC b) 3 vol% SiC c) 6 vol% SiC d) 12 vol% SiC [89]

The hardness and strength of MMCs also increased with the addition of SiC due to the properties of the ceramic [89].

On the other hand, study [91] compared the phase composition, microstructure and mechanical properties of Fe/SiC with a volume ratio of 95 to 5 to pure iron samples. It stands out the fact that the SiC was partially melted. Hence, homogeneously distributed SiC particles were visible throughout the Fe matrix. Furthermore, the structural modification generated by SiC particles can be observed in Figure 26a and b in comparison to only Fe samples showed in Figure 26c and d. The fine needle-shaped martensite and partial pearlite can be observed which was also confirmed by the XRD results. Since the carbon content in the iron powder was only 0.03 vol% this martensitic and pearlitic microstructure can only be associated to the SiC [91].

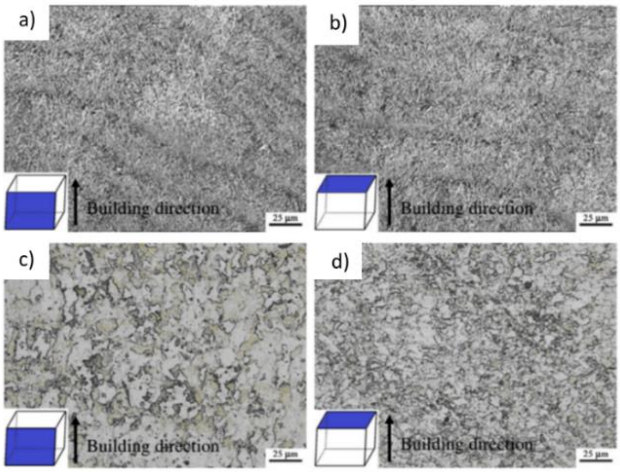

Figure 26. SEM images showing a) Fe/SiC cube from the front view b) Fe/SiC cube from the top view c) Fe cube from the front view d) Fe cube from the top view [91]

It is also worth noting that the homogeneous microstructure obtained with the SiC has replaced the elongated or columnar grains along the building direction observed in the pure Fe samples. Such a homogeneous microstructure can be a way to eliminate the anisotropic mechanical properties with the addition of SiC [91].

In general, again, much higher values of strengths were obtained with the SiC samples due to retained reinforcing agent itself, the modification of microstructure, grain refinement and the dislocation pinning by the SiC particles resulting from the SiC decomposition [91].

Summarizing, SiC partially dissolve during manufacturing in the matrix. Depending on SiC content different microstructures show up, reaching the formation of carbides and even graphite needles. This result in different optimal processing parameters that will vary the hardness and overall properties [92].

3 MATERIALS AND EXPERIMENTAL METHODS

In this section the equipment and the methods used for the experimental part are presented.

3.1 Original powders

The raw materials used in this work are AISI S2 (Shock-Resisting Tool Steel) and SiC (Silicon Carbide).

3.1.1 S2 Tool Steel

The S2 tool steel powder was provided by SANDVIK OSPREY LTD. It was produced with gas atomization, using nitrogen as the atomise gas. Regarding the Particle Size Distribution (PSD), Laser Diffraction Analysis reveals a D10 % of 20.6 µm, a D50 % of 31.0 µm and a D50 % of 47.5 µm, according to the datasheet provided by the supplier (Annex 1). In Figure 27 the morphology of the powders can be seen along with their chemical composition in Table 6.

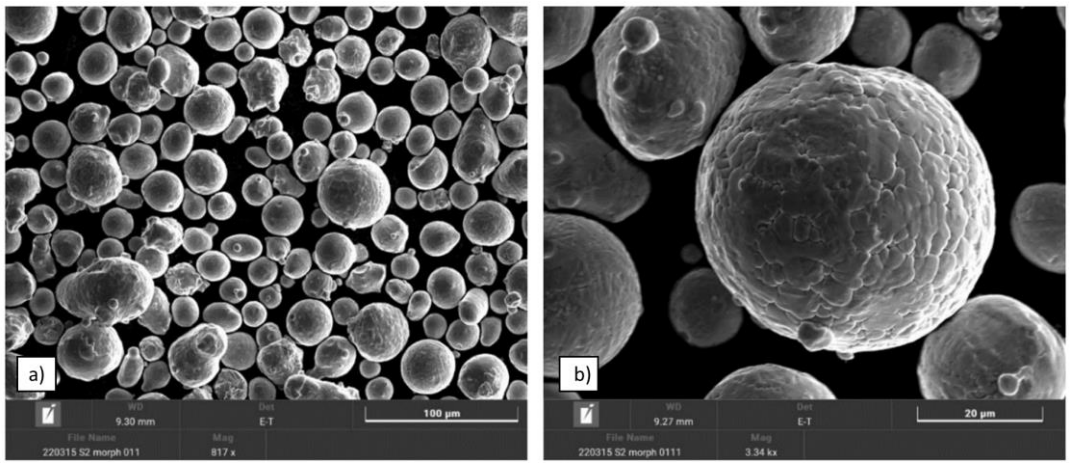

Figure 27. SEM micrographs of S2 powders at magnifications a) 817x b) 3.34 kx

Element	C	Si	Mo	Mn	Fe
wt.%	0.49	1.20	0.6	0.6	Bal.

Table 6. Chemical composition of S2 powders

3.1.2 Silicon Carbide (SiC)

The SiC powders were provided by the company KYOCERA. It was also tested the PSD obtaining a D10 % of 0.4 µm, a D50 % of 0.75 µm and a D90 % of 1.5 µm. The morphology of the SiC powders and the chemical composition can be seen in Figure 28 and in Table 7 respectively. In Figure 28a the typical formed agglomerations are depicted whereas in Figure 28b the irregular nanoparticles are shown.

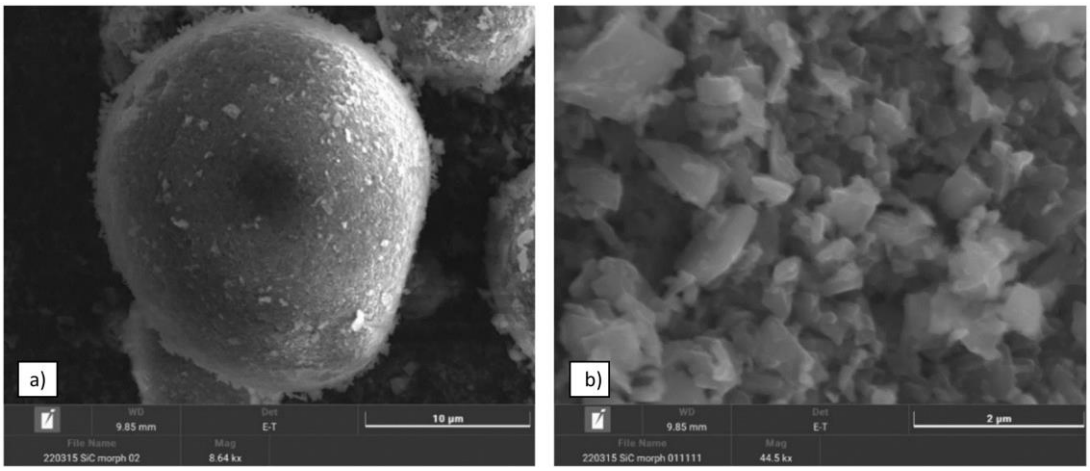

Figure 28. SEM micrographs of SiC powders a) granule b) nanoparticles

Element	C	O	Al	Ca	Fe
wt.%	29-30	max 1.5	max 0.03	max 0.01	max 0.05

Table 7. Chemical composition of SiC powders

3.2 Mixed powders

S2 tool steel was mixed with 10 % in volume of SiC. In order to obtain a homogeneous mixture with the good rheological properties required by the LPBF process, different devices and operational steps were performed.

3.2.1 Sieve shaker

Sieving processes are needed to make sure that the particles used in the printing process are smaller than 63 µm, as required for the LPBF process. The sieve shaker used is from Haver and Boecker and the model is Haver EML 200 Premium. It allows up to 3 Kg of sample weight with amplitudes up to

3 mm. Among the advantages, the quietness and the three-dimensional movement stand out [93]. The test sieves available are of 250, 125, 80, 63 and 50 µm.

Figure 29. Haver EML 200 Premium

3.2.2 Ball milling

The device used to blend homogeneously the mixed powder is a 'Pulverisette 6'. It is a high-performance Planetary Ball Mill with a single grinding bowl and high-energy effect of up to 650 rpm [94]. It is composed by the turning system, a bowl where both the powders and balls are put and these stainless-steel balls.

The parameters used in this study for the mixture are the following:

Ball to Powder Ratio	Time	Rotational speed	Number of balls
1:4	45 min	100 rpm	16

Table 8. Ball milling parameters used

Figure 30. Ball milling equipment a) 'Pulverisette 6' b) Bowl and metal balls

3.2.3 Optimal preparation

The correct preparation regards the optimization of the results obtained from the previous work with the same powders [71].

First, excluding the SiC granules larger than 50 µm was required, as in the original powders are present granules bigger than 100 µm. This step was necessary to allow the complete dissolution of the SiC during the LPBF process since undissolved granules generate non-homogeneous parts in both composition and properties. Then, the mixture S2 + 10% (in vol.) of SiC was carefully manually mixed in order to homogenise the two different powders and avoid segregation. Ball milling was then used to break the SiC granules and make adhering the SiC nanoparticles to the surface of the S2 powders. Finally, a sieving using a test sieve of 63 µm was used, to exclude any agglomerates that may have formed during the ball milling. After this final step, a negligible mass lost was detected. Therefore, the powders composition can be assumed as S2 + 10% (in volume) of SiC. A scheme of the optimal powder preparation process is:

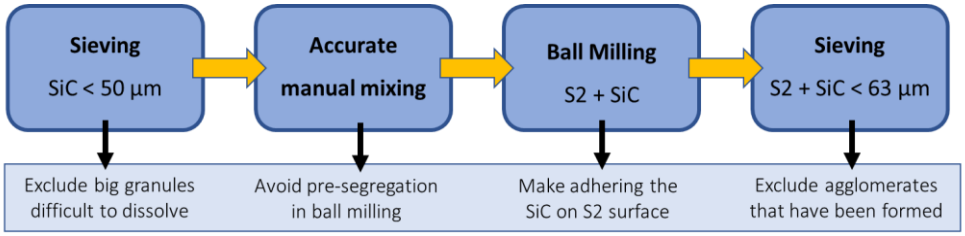

Figure 31. Optimal powder preparation process

Preparing the powders using the optimized method and making sure there are no agglomerates larger than 63 µm, resulted in a good mix of S2 + 10%SiC in terms of homogeneity. After the optimal powder preparation process the mixed powders had the following aspect:

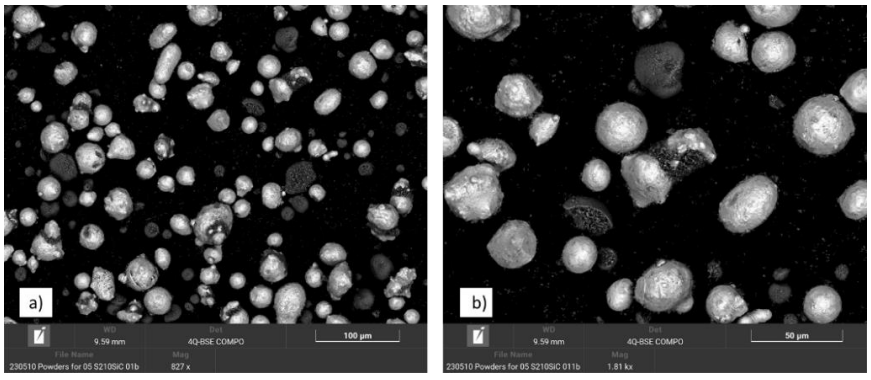

Figure 32. SEM images of Blended S2 + 10%SiC at a) 827x magnification b) 1.81kx magnification

S2 particles (white) and SiC agglomerations (dark) broken due to ball milling can be seen. With higher magnification, Figure 32b, small and irregular SiC particles attached to the S2 can be observed. Also, S2 changed morphology due to ball milling hits can be identified.

3.3 Samples fabrication

3.3.1 LPBF machine

The machine used to produce the samples is a brand-new LPBF 3D printer from Aconity. The model is AconityMINI and represents the entry-level system from the company. It has full access to all relevant process parameters, allowance for efficient material research and fast part production for small batches. Besides, it has a strong recirculation, allowing the production of highly reactive materials with high amount of weld fumes. The device is equipped with preheating up to 500ºC. [95]. The technical specifications from the producer are the following:

Build space	Ø 140 mm x H 190 mm Ø 55 mm x H 190 mm
Laser Configuration	Single Mode resp. AFX Multi Mode 400 W / 500 W / 700 W / 1000 W / 1200 W AFX Green Single Mode 200 W / 400 W
Optics configuration / Spot size	F-Theta / 80 µm 3D Scanning / 80 – 500 µm
Process monitoring options	Coaxial pyrometer Coaxial high-speed CMOS
Preheating temp / build space	500 °C / Ø 140 mm x H 150 mm 800 °C / Ø 100 mm x H 150 mm
Layer thickness	Down to 10 µm
Max scan speed	12 m/s
Inert gas type / pressure	Argon 4.6 / 6 bar Nitrogen / 6 bar Vacuum / < 2 mbar
Inert gas consumption	< 5 l/min during process < 60 l/min during purging 0 - 5 l/min for vacuum
Residual oxygen content	< 100 ppm
Pressurized air type / pressure	ISO 8573-1:2010 [1:4:1] / 6 bar
Pressurized air consumption	< 50 l/min
Machine Dimensions (W x D X H)	2450 mm x 1500 mm x 2320 mm
Machine weight w/o powder	850 kg

Table 9. Technical specifications of AconityMINI

3.3.2 Parameters of the samples

Two batches of samples (10*10*10 mm^3) have been used in this study. The first one is samples of S2 + 10%SiC with no preheating. The second, samples of S2 + 10%SiC with a preheating of 500ºC applied. In all of them has been regulated a Gaussian laser distribution with a laser spot size of 80 µm, no supports, a scan strategy of 90º/90º, a hatch distance of 80 µm and a layer thickness of 30 µm. Also, argon was used as the inert gas. The parameters that change between the samples are the laser power, the scan speed and, thus, the VED. In the second batch, they were adapted considering the best samples of the first batch. The parameters of each batch are listed in Table 10 and Table 11.

- **Batch 1:** S2 + 10%SiC no preheating

Sample	P [W]	Vs [mm/s]	VED [J/mm3]
7	150	600	104
8	150	800	78
12	175	800	91
13	175	1000	73
10	175	400	182
16	200	500	167
17	200	600	139
14	200	700	119
18	200	800	104

Table 10. Printing parameters of batch S2 + 10%SiC with no preheating

- **Batch 2:** S2 + 10%SiC with preheating of 500ºC (P500)

Sample	P [W]	Vs [mm/s]	VED [J/mm3]
1	175	500	146
2	175	600	122
3	175	700	104
4	200	700	119
5	200	600	139
6	200	800	104
7	200	1000	83
8	200	1200	69
9	200	700	119

Table 11. Printing parameters of batch S2 + 10%SiC P500

3.4 Microstructural characterization

3.4.1 Samples preparation

In order to analyse and perform the full characterization of the samples, the internal cross-sections of the cubes are needed. The cubes were cut from the substrate and cut again vertically in three parts. It was cut in three to be able to use the same sample in different analysis if needed. In case Differential Thermal Analysis (DTA) was required, one of the three parts is also cut in three due to the necessity of smaller parts. The cutting is done with the Spark Erosion Machine. It is basically a manufacturing device used to cut or create shapes using sparks coming from the current discharges between two electrodes separated by a dielectric liquid [96].

After cutting, the samples are stored in a bakelite using a powerful hot mounting press named Struers Citopress-1. The procedure to create this bakelite is to put both the sample and bakelite powder inside the machine hole. It is then heated and pressed together to finally obtain the bakelite with the cross sections visible.

Figure 33. Struers Citopress-1 [97]

However, the surface needs to be polished so a clear and plane surface is obtained. The polisher used is Struers Tegramin-30. It is an automatic, microprocessor-controlled machine for polishing and grinding on a 300 mm disk with a cone [98]. It uses a wear paper with some lubricant to polish the surface with rotational movements.

Figure 34. Struers Tegramin-30 [98]

The samples in the bakelite after all this procedure have the following appearance:

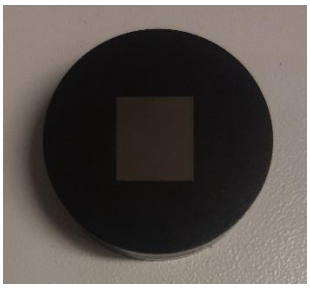

Figure 35. Sample prepared in the bakelite and polished

3.4.2 Optical Microscope (OM) and Stream Analysis Software

The optical microscope used to analyse the cross sections is the Olympus BX60M along with the software Stream Motion used to see in real live what the microscope is focusing and take the interesting pictures. It has six different magnifications: 2,5x, 5x, 10x, 20x, 50x and 100x. The reflected light is powered by a 12V 100W lamphouse [99].

Figure 36. Olympus BX60M [99]

The OM was used to see the defects present in the samples, the melt pools morphologies and sizes, analyse the microstructure and take overviews of the cross sections to obtain the porosity values.

However, the melt pools and microstructure require a previous etching of the surface in order to be observable. An etching is a technique where a reactive liquid is impregnated in the sample and, depending on the liquid, different microstructures are highlighted. In this study the liquids used are Nital 2% and Alkaline Sodium picrate at 90ºC. The first one is the most used for steels and it is excellent for revealing martensitic microstructures. Also, it is good for revealing ferrite in martensite matrix and for showing ferrite grain boundaries in low carbon steels. Alkaline Sodium picrate reagent is used to colour cementite, whether it is in pearlite or primary cementite in white cast iron [100].

Furthermore, the porosity analysis required the overviews at 2,5x and a software to mark and quantify the holes. The program used is Stream Analysis Software. The program allows the user to delimitate a zone of interest manually. Inside the zone, is able to quantify the dimension of the holes and the average value, the total area of porosities and the percentage of porosity. Indeed, this is based on a 2D cross-section overview that may differ from another of the same sample.

3.4.3 Scanning Electron Microscope (SEM)

To deeply analyse the samples surface a SEM was used. It uses an electron beam that interact with the atoms of the sample and gives information regarding the topography and composition [101]. More specifically, the model used is Tescan Clara Ultra-High Resolution SEM. Before using the SEM, though, the samples in the bakelite need further preparation. A conductive bond between the sample and the bottom of the bakelite needs to be formed. Thus, silver painting has been used.

Figure 37. Tescan Clara UHR SEM [102]

Electron Backscatter Diffraction (EBSD) and Energy-dispersive X-ray spectroscopy (EDX) tests have been also conducted by means of the SEM. The first one enables the sample's microstructure to be analysed, visualized and quantified [103]. The second, is used for the chemical characterization of the sample [104].

3.5 Thermo-Physical Analysis

3.5.1 Pycnometer

The density values of the samples, that can be related to the porosity, defects and overall quality, have been measured with a pycnometer. It has been used a gas pycnometer from the company Micromeritics model AccuPyc II 1345. Gas pycnometry is recognized as one of the most reliable techniques for obtaining the absolute, true, skeletal and apparent volume and density [105].

Figure 38. AccuPyc II 1345 [105]

For each sample 5 different density values have been obtained, considering the average.

3.5.2 Differential Thermal Analysis (DTA)

STA 449C Jupiter from the company NETZSCH was used to carry out DTA tests on the samples after the LPBF process. The test consisted in heating and cooling with no isothermal time in between. However, the heating and cooling rate from the DTA (5ºC/min and 20ºC/min respectively) is much slower than what actually happens in LPBF (peak cooling rates of 40ºC/µs) [106] so it is an approach.

Figure 39. STA 449C Jupiter from NETZSCH [107]

3.6 Hardness test

Emco test M1C 010 was used to perform macro hardness measurements. It provides the value of macro hardness at small test forces, doing an indentation in the as-polished sample. The range of HV available goes from HV 0.1 to HV 30 [108]. The machine can switch between an optical microscope and the indenter so the user can firstly select where the indentation is going to be placed. In the experimental part a grid of indentations has been performed to see the tendency of the hardness as a function of the height of the layer. HV 5 have been used in all the sample except in the top layer, in which HV 1 was used to precisely calculate the value in only this region. The samples used were the best (in terms of high density and defect-free) for both batches.

Figure 40. EMCO test M1C 010 [109]

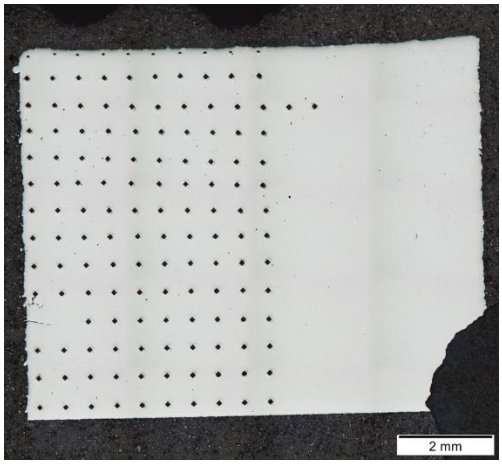

Figure 41. Grid of indentations in sample 14 without P500

4 RESULTS

4.1 Printing process

4.1.1 S2 + 10%SiC

The printing of samples with S2 + 10%SiC with no preheating was performed firstly. The batch appeared with cracks in every sample, mainly horizontally close to the substrate. Also, sample number 18 appeared with a huge vertical open crack. The best sample visually was number 14, even if it presented a small crack at the bottom.

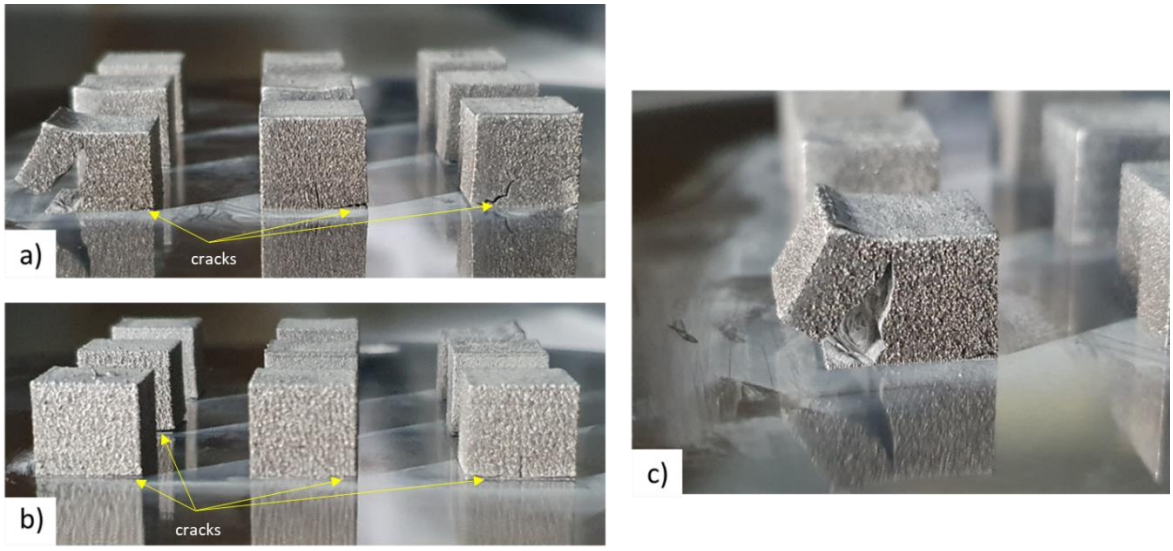

Figure 42. Batch 1 of S2 + 10%SiC a) front image b) lateral image c) crack in sample 18

Figure 43. S2 + 10%SiC samples in the substrate

However, in most of the studies sample number 17 was not considered due to a problem on the cutting process that made it impossible to analyse.

4.1.2 S2 + 10%SiC with preheating

Since the final objective of every AM material research is obtaining crack-free fully dense samples, which was not accomplished with S2 + 10%SiC, a preheating on the baseplate was added. The parameters can be seen in Table 11. Interestingly enough, the best observable sample had the same parameters as the best sample with no P500. This time no cracks nor major defects could be observed. The printing process was fluid with no significant problems detected.

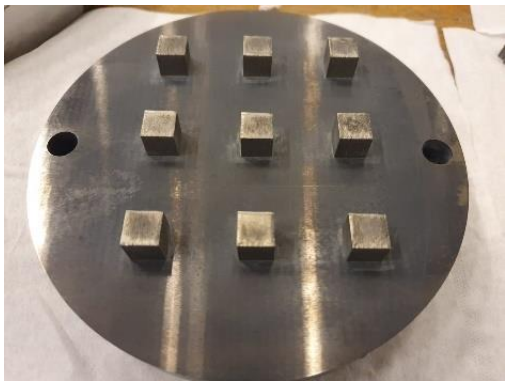

Figure 44. S2 + 10% SiC P500 samples in the substrate

4.2 Post-process analysis

4.2.1 Pycnometry density evaluation

The density of each sample for both batches is visible in Table 12. Figure 45 shows the density as a function of the VED applied. The value of sample number 18 has not been taken because of the vertical crack.

Batch	Sample	Average density [g/cm^3]
No Preheating	7	7.685
	8	7.621
	12	7.653
	13	6.427
	10	7.515
	16	7.548
	14	7.599
	18	-
Preheating	1	7.469
	2	7.551
	3	7.538
	4	7.547
	5	7.514
	6	7.570
	7	7.525
	8	7.565
	9	7.530

Table 12. Density of all the samples of S2 + 10%SiC

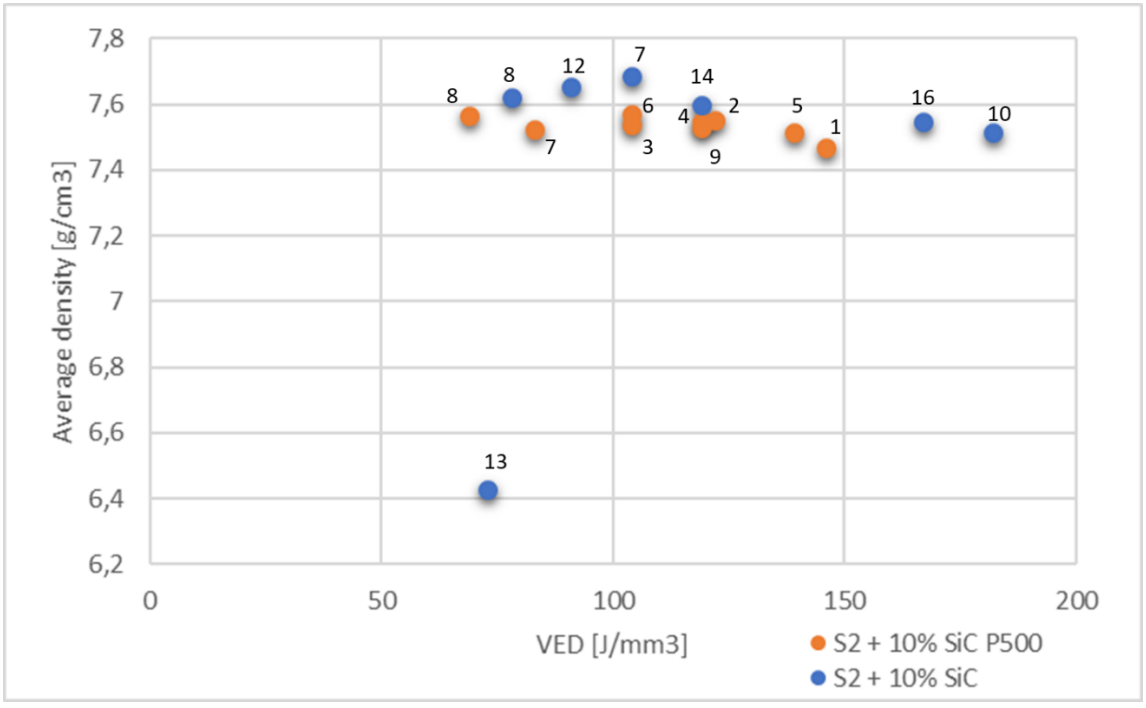

Figure 45. Density vs VED graph in every S2 + 10%SiC sample

4.2.2 Cross sections

Cross-section overviews at 2.5x magnification were taken in every sample in order to check internal defects, such as porosities and cracks. Besides, they were used after etching to see the microstructure and the top layers.

- **Batch 1:** S2 + 10%SiC no preheating

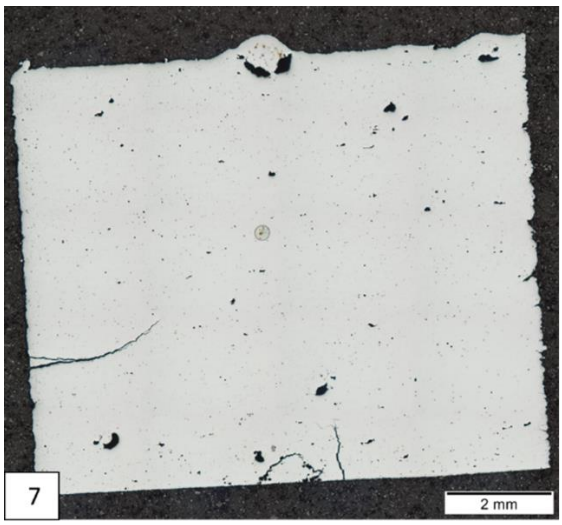

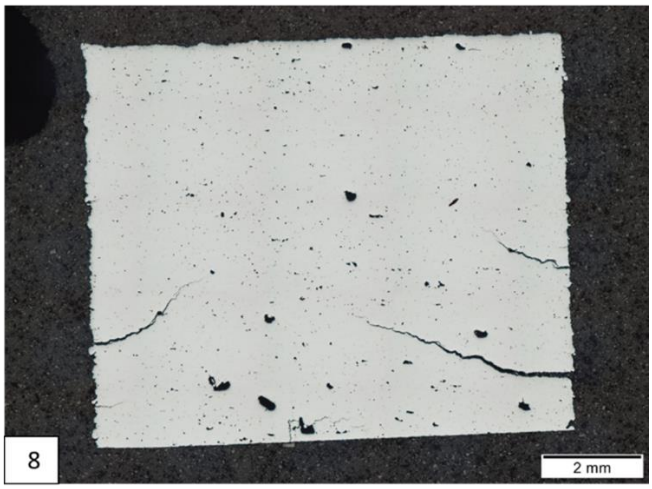

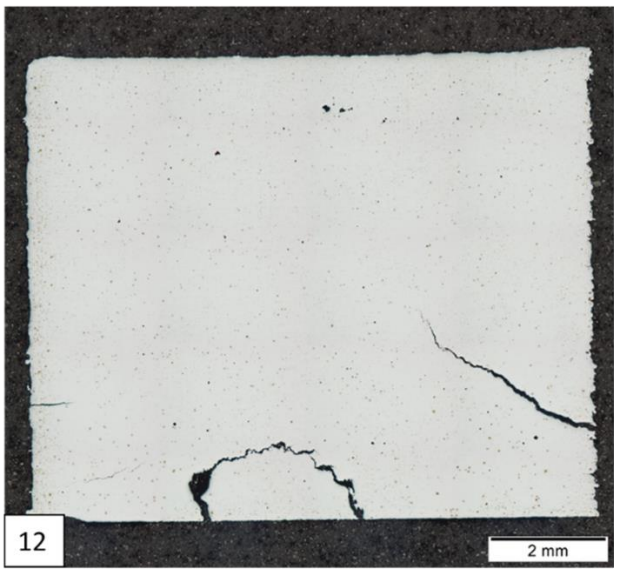

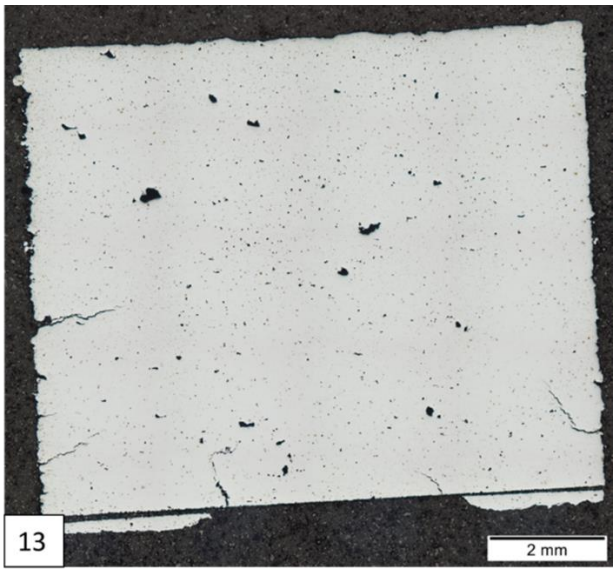

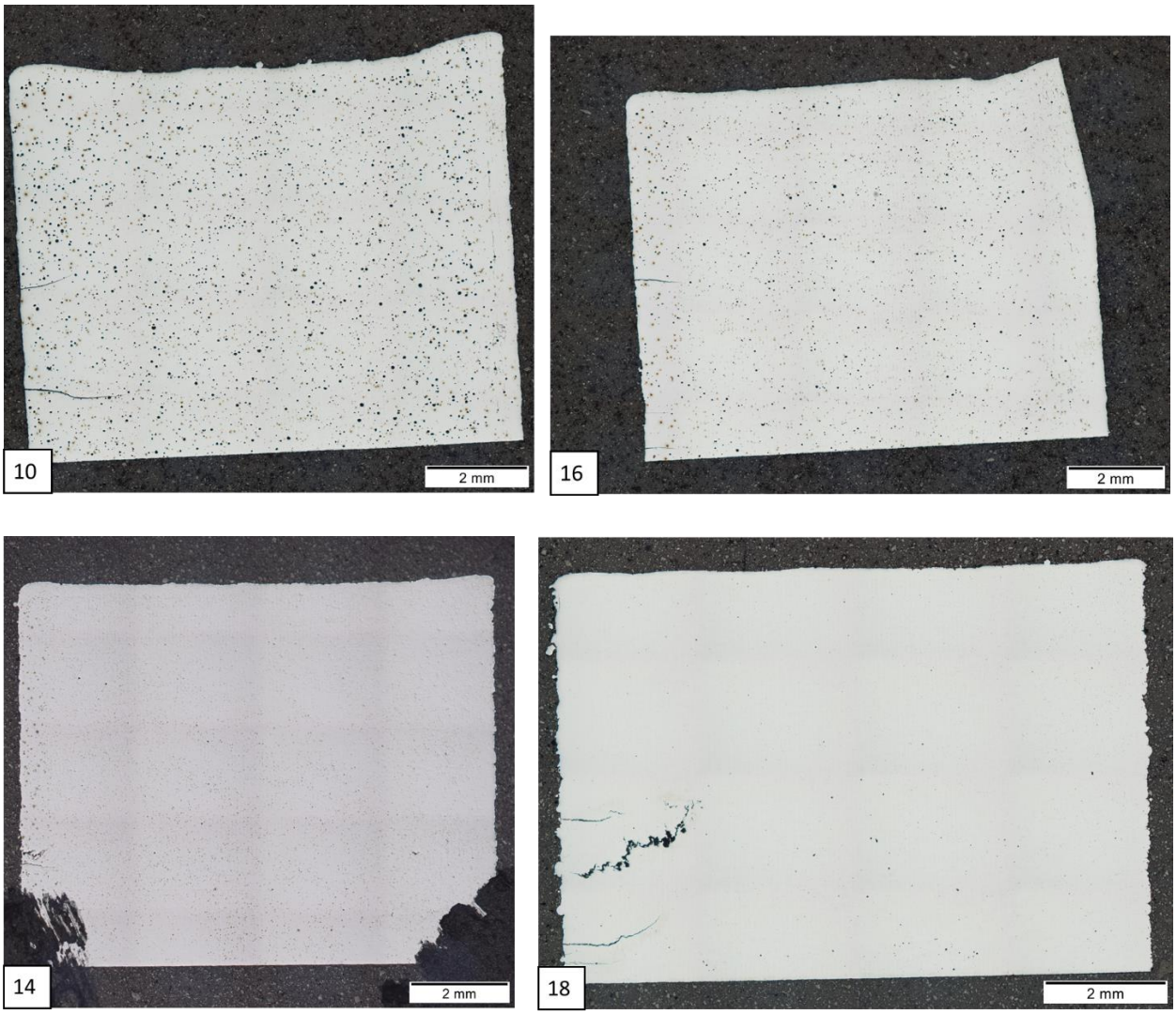

Figure 46. Cross-sections overviews of samples of S2 + 10%SiC

- **Batch 2:** S2 + 10%SiC P500

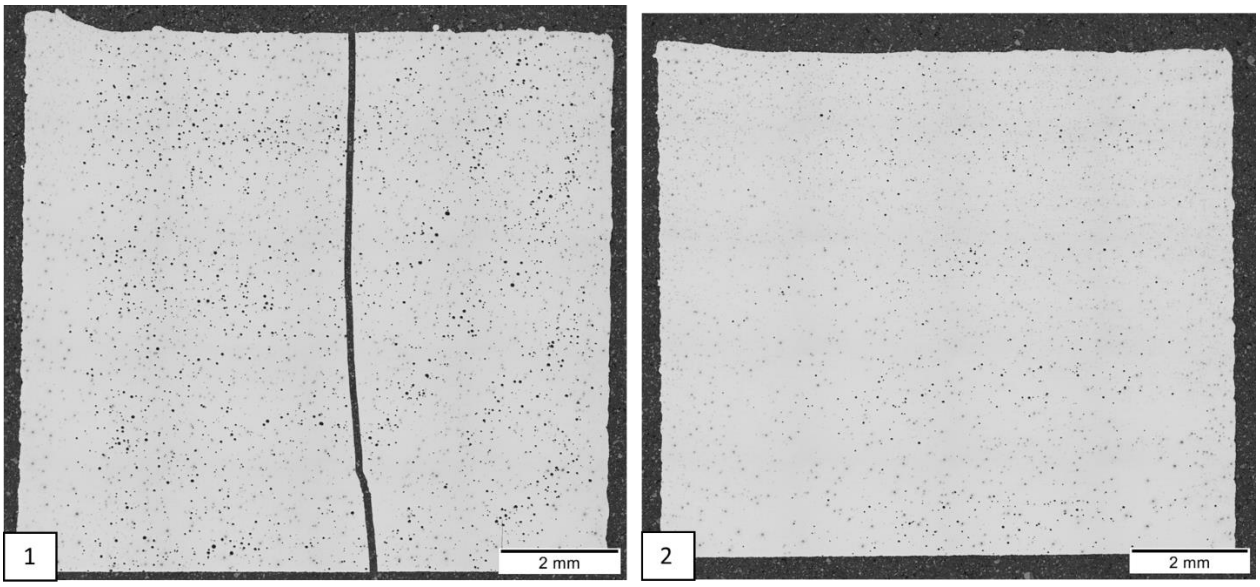


3
2 mm

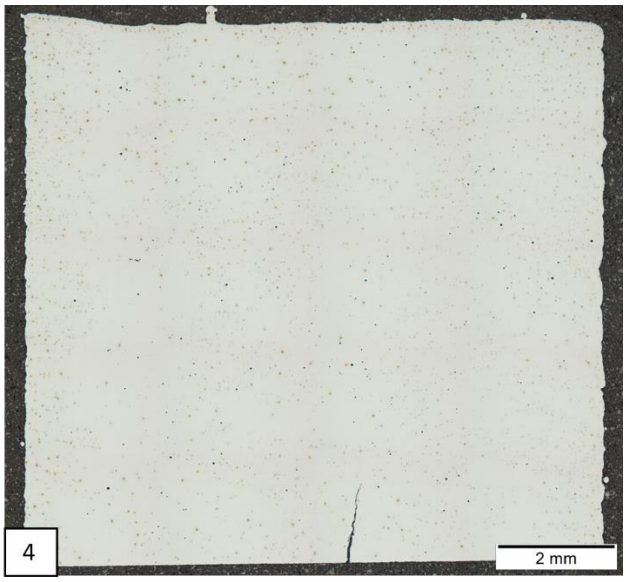
4
2 mm

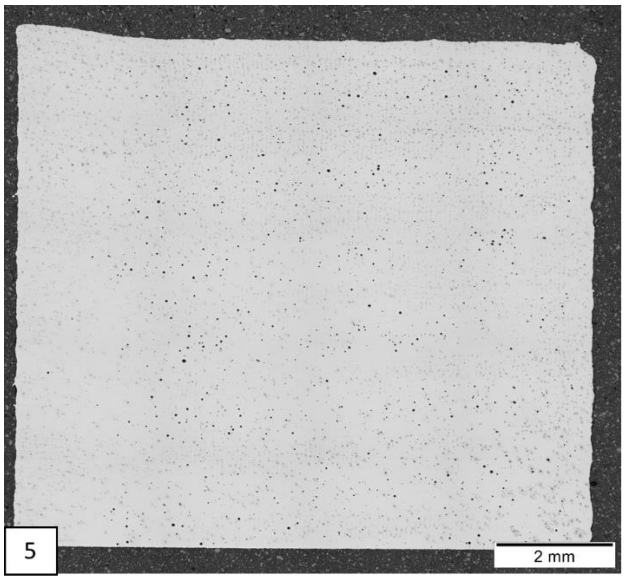
5
2 mm

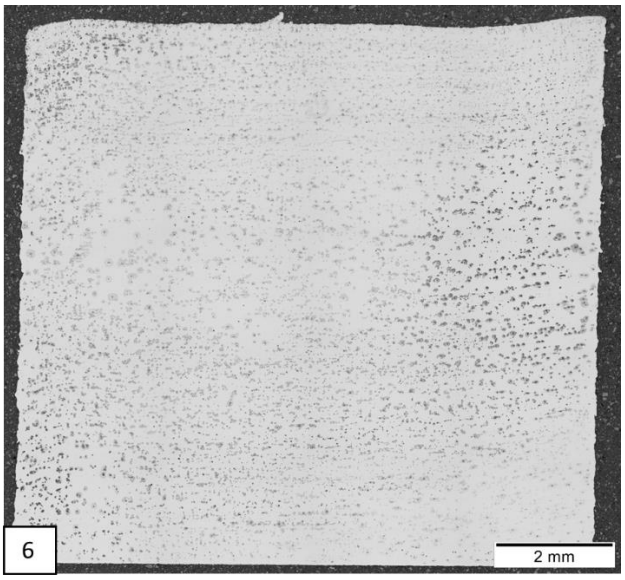
6
2 mm

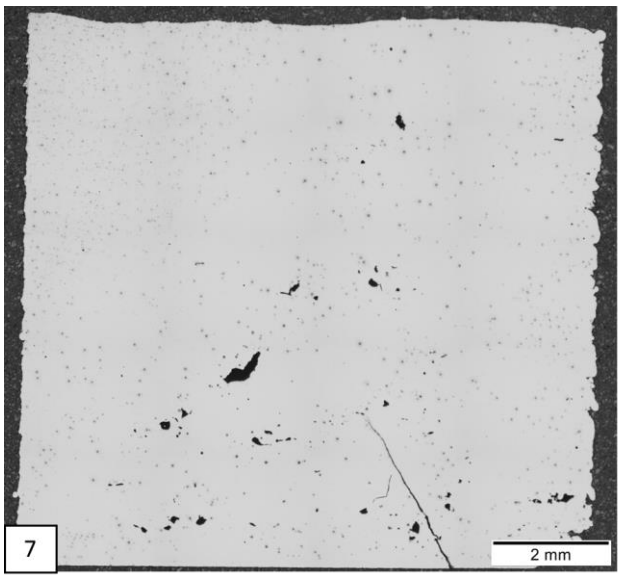
7
2 mm

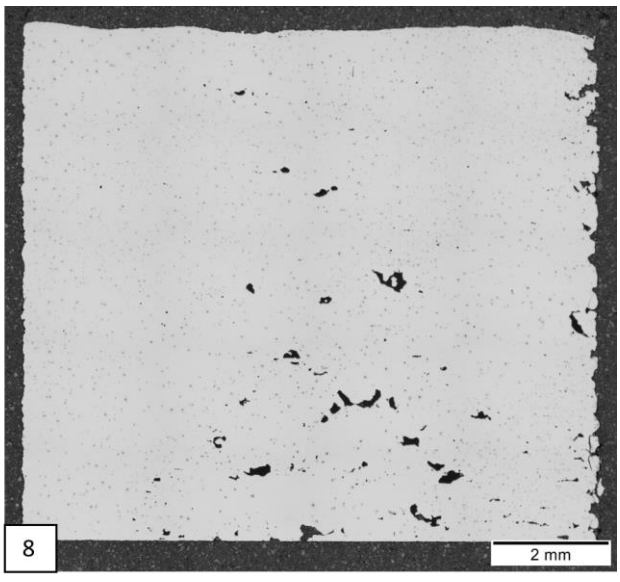
8
2 mm

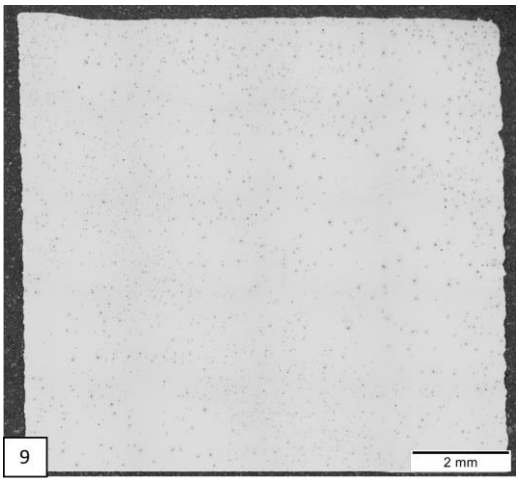

Figure 47. Cross-sections overviews of samples of S2 + 10%SiC P500

4.2.3 Defects quantification and characterization

Using Stream Analysis Software, the percentage of porosities in every sample has been quantified.

Batch	Sample	Porosity [%]
No Preheating	7	0.879
	8	0.992
	12	0.085
	13	0.754
	10	2.263
	16	0.699
	14	0.051
	18	0.043
Preheating	1	1.249
	2	0.323
	3	0.072
	4	0.082
	5	0.036
	6	-
	7	0.494
	8	0.902
	9	0.007

Table 13. Porosity values for all S2 + 10%SiC samples

Porosity of sample number 6 of batch 2 was not possible to quantify due to difficulties to identify what were porosities in the cross-section.

The values of porosity as a function of VED were put on a graph along with the values of the samples produced with only S2 of "Fabrication and characterization of low-alloyed tool steel obtained by Selective Laser Melting," 2023 [1]. Figure 48 also shows acceptable values of porosity for S2 (grey rectangle), for S2 + 10%SiC (blue rectangle) and for S2 + 10%SiC P500 (orange rectangle). The acceptable values for S2 + 10%SiC are in between the range of the acceptable values of S2 but with a much smaller range. However, when preheating is added the range increases again.

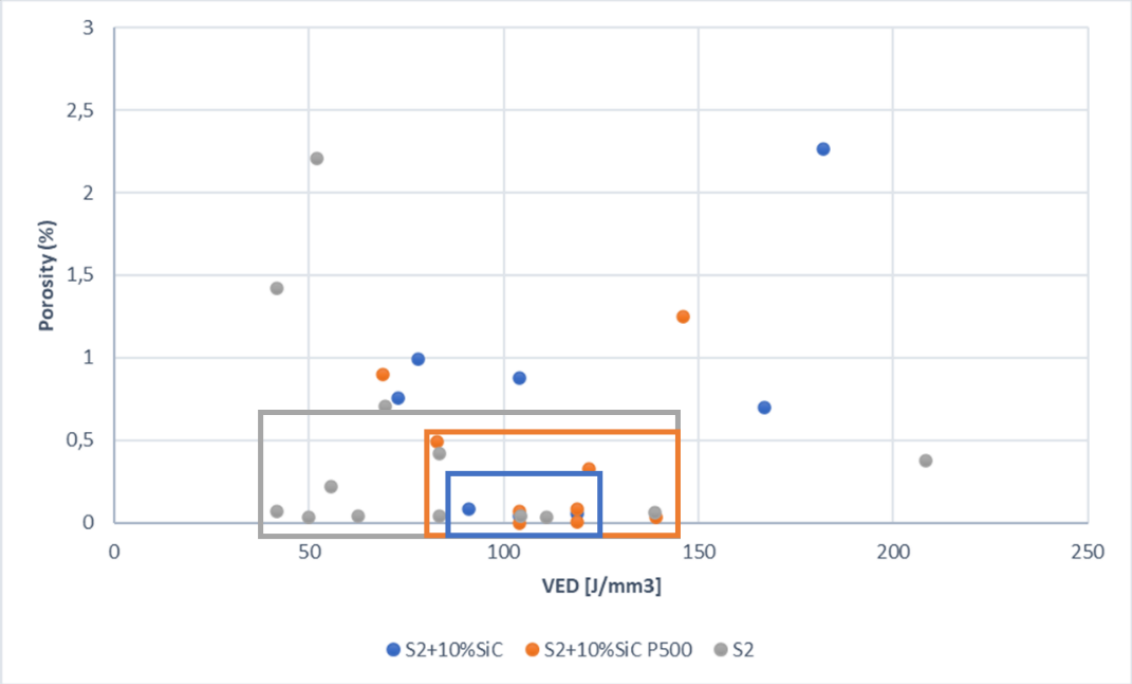

Figure 48. Porosity values of only S2 and S2 + 10%SiC with and without preheating batches

Furthermore, using the cross-sections, the type of porosities were also evaluated. In every sample, little rounded gas porosities were found. Thus, it was not possible to relate this kind of porosity to any parameter. In some samples, though, the quantity was higher than in others.

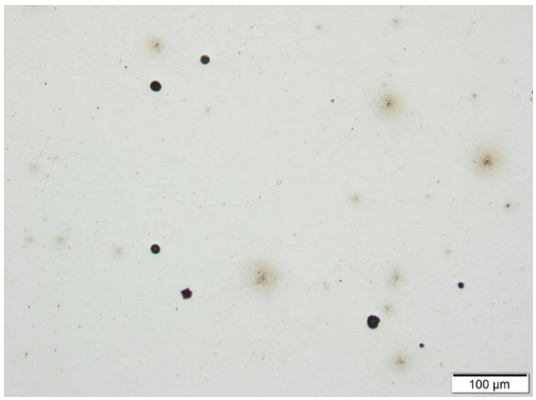

Figure 49. Gas porosities in sample 4 of S2 + 10%SiC P500

On the other hand, LOF porosities were also found in both preheated and non-preheated samples. This time, this type of defects appeared only in the samples with low VED. Some examples can be seen in Figure 50.

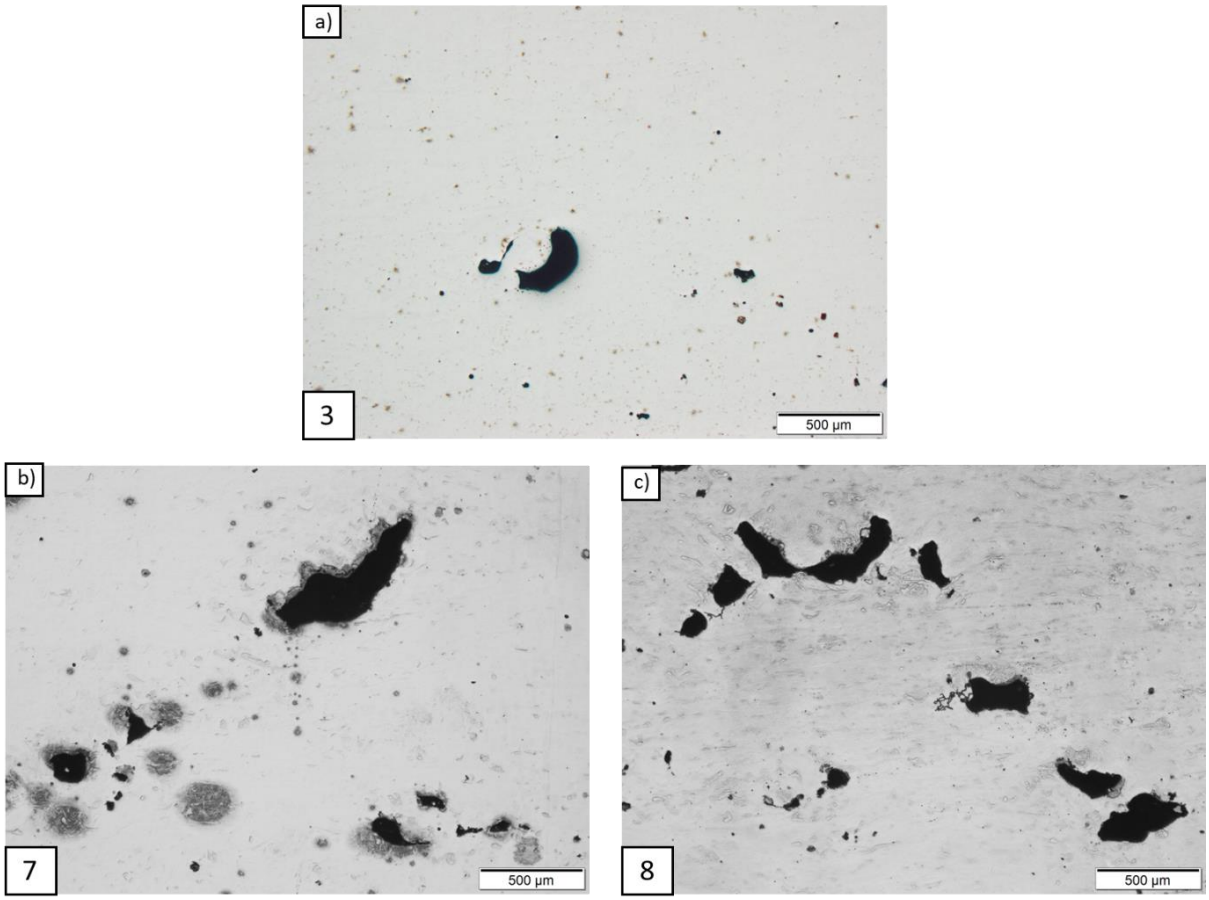

Figure 50. LOF defects in a) sample 3 of S2 + 10%SiC b) sample 7 of S2 + 10%SiC P500 c) sample 8 of S2 + 10%SiC P500

Similarly, keyhole porosities were also identified in some samples. These defects were concentrated only in samples with high VED.

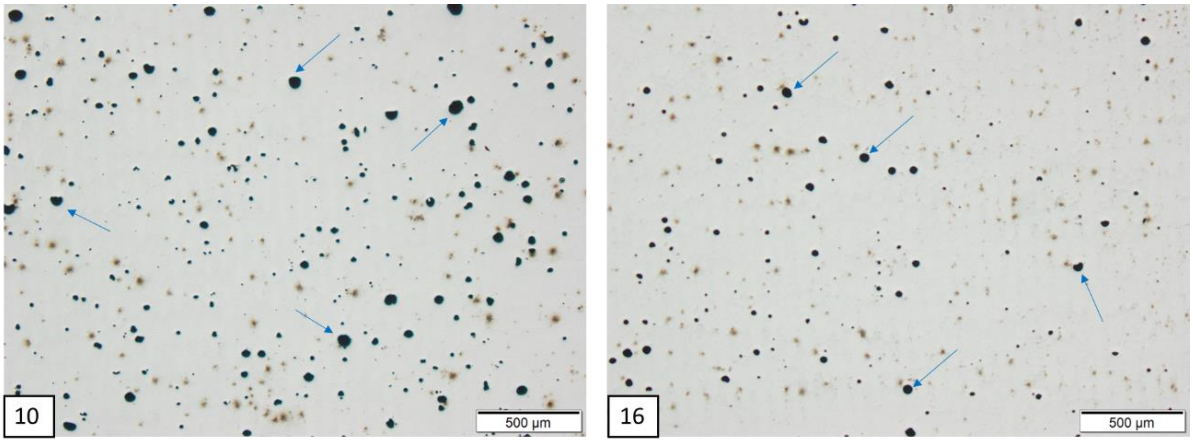

Figure 51. Keyhole porosities in samples 10 and 16 of S2 + 10%SiC P500

Also, cracks were found in every non-preheated sample and in some preheated too.

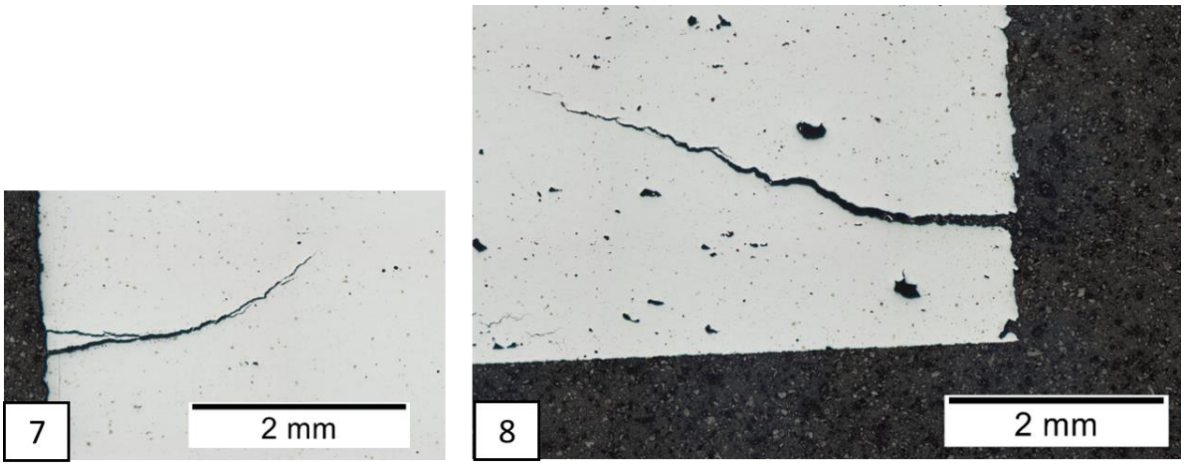

Figure 52. Cracks in samples 7 and 8 of the non-preheated batch

As a summary, a table showing which defects were found in each sample is constructed. Green ticks mean that the sample is free or nearly free of the said defect. The red “X” means that it contains this type of defect.

- **Batch 1:** S2 + 10%SiC no preheating

Sample	VED [J/mm3]	Keyhole porosities	Lack of Fusion	Gas Porosities	Cracks
10	182	✗	✓	✗	✗
16	167	✗	✓	✗	✗
14	119	✓	✓	✗	✓
18	104	✓	✗	✗	✗
7	104	✓	✗	✗	✗
12	91	✓	✗	✗	✗
8	78	✓	✗	✗	✗
13	73	✓	✗	✗	✗

Table 14. Defects in S2 + 10%SiC samples

- **Batch 2:** S2 + 10%SiC P500

Sample	VED [J/mm3]	Keyhole porosities	Lack of Fusion	Gas Porosities	Cracks
1	146	✗	✓	✗	✗
5	139	✗	✓	✗	✓
2	122	✓	✓	✗	✓
4	119	✓	✓	✗	✗
9	119	✓	✓	✗	✓
6	104	✓	✓	✓	✓
3	104	✓	✓	✗	✓
7	83	✓	✗	✓	✗
8	69	✓	✗	✓	✓

Table 15. Defects in S2 + 10%SiC P500 samples

The table is organized in decreasing VED. Thus, the relation between VED and type of defects is clear. High VED implies keyhole porosities. On the contrary, low VED is associated to LOF porosities. The VED from which each type of defect starts to appear is also different depending on

the preheating. Regarding keyhole porosities, only samples with 167 J/mm^3 or higher exhibit them in non-preheated samples while preheated samples with 139 J/mm^3 or higher already show this defect. However, LOF seems to appear much easier in non-preheated samples because 104 J/mm^3 samples appear with LOF whereas the same VED in preheated samples do not exhibit it. In preheated samples LOF starts at 83 J/mm^3. That means preheating has a significant effect on shifting the process map. Besides, in non-preheated samples more defects are present.

4.2.4 Melt pools characterization

Etching the samples allowed to see the layers depths and morphologies. Focusing on the top layer, values of its depths were taken in different points of each sample.

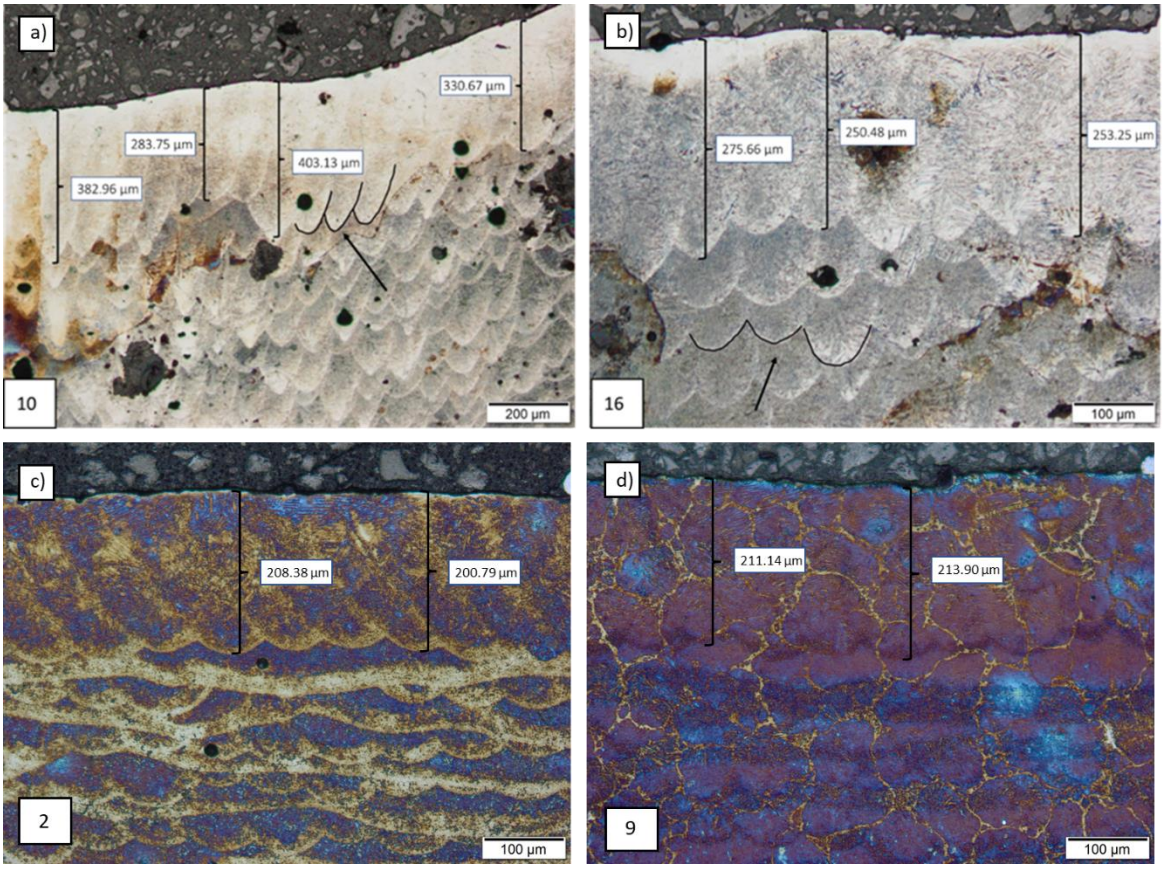

Figure 53. Top layer depths and morphologies of a) sample 10 with no preheating b) sample 16 with no preheating c) sample 2 with preheating d) sample 9 with preheating

With the different values an average per sample was calculated. The values of top layer depth as a function of the VED of both batches plus the only S2 samples of the study "Fabrication and characterization of low-alloyed tool steel obtained by Selective Laser Melting," 2023 [1] were put in

a graph. In some preheated samples, however, was difficult to identify the top layer so no value was obtained. The tendency line for each batch was also included.

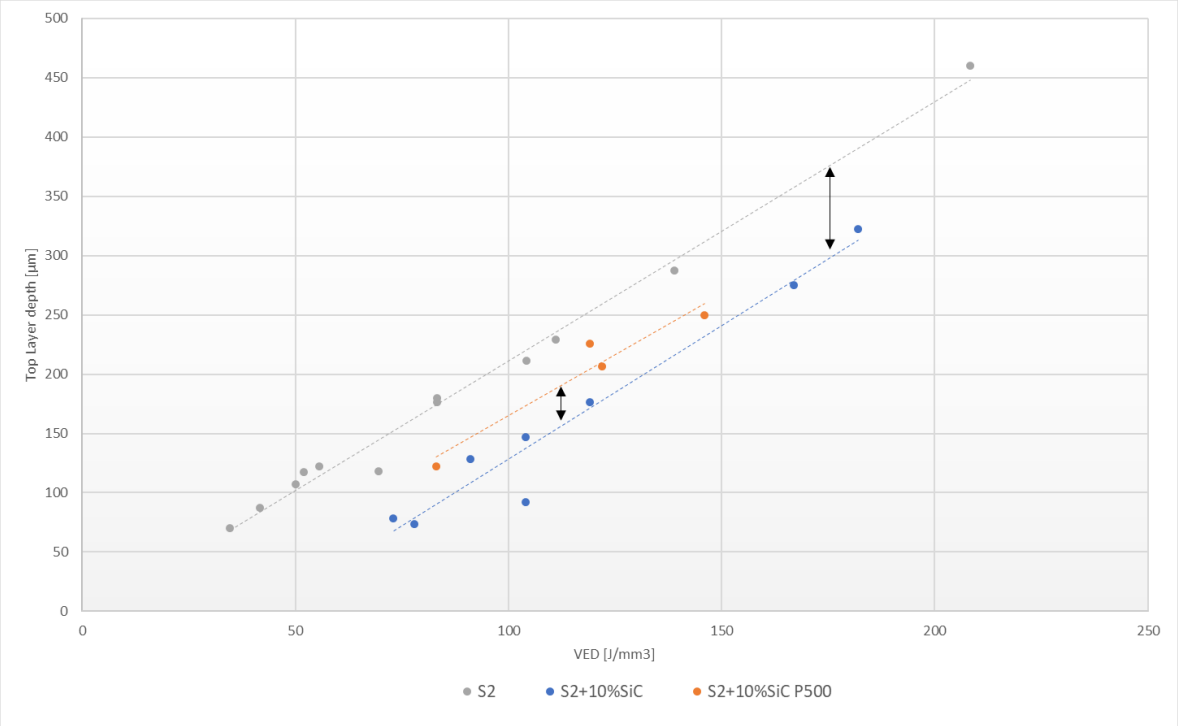

Figure 54. Top layer depths as a function of VED in only S2 and preheated and non-preheated S2 + 10%SiC samples

It can be observed that increasing the VED result in deeper top layers. Also, at the same VED, S2 samples tend to have higher values of top layer depth than S2 + 10%SiC. Out of the two batches with SiC, though, preheated samples have higher top layer depth.

4.2.5 Microstructure

In order to analyse better the microstructure, we are going to focus on one preheated and one non-preheated sample. These are sample 14 without preheating and sample number 9 with preheating, since they are the best ones of each batch. OM, SEM, EDX and EBSD analysis were performed. In this section all the relevant microstructural aspects will be showed.

Firstly, the OM of sample with no preheating depicts a clear needle-shaped phase uniform in the whole sample whereas in sample number 9 different zones can be well identified.

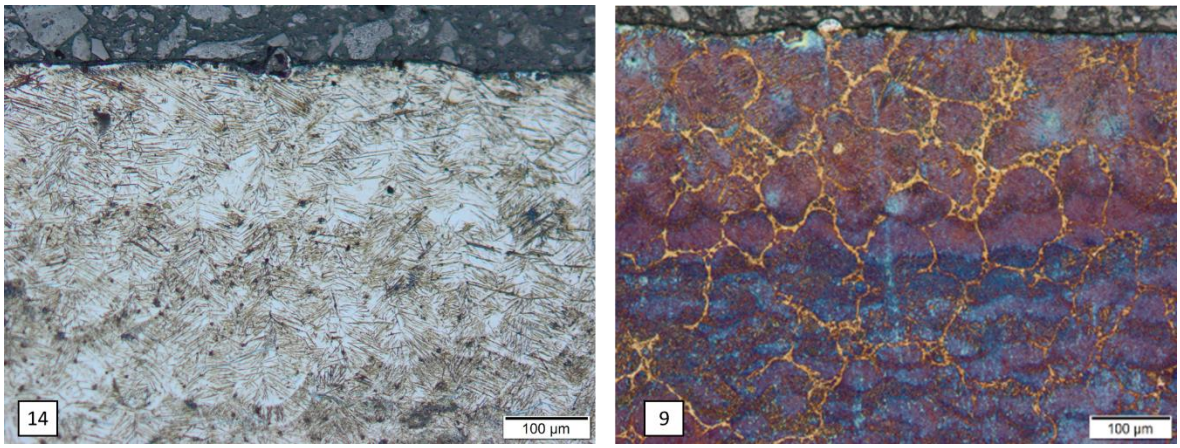

Figure 55.OM of sample number 14 with no preheating and sample number 9 with preheating

The top layer in sample number 9 has a microstructure in form of brown elongated dendrites in contrast to the center of the sample that has a much more uniform, compacted and coarse zone. Furthermore, big grains separated by a yellow grain boundary phase can be observed all over the sample with the Alkaline sodium picrate. This can be observed in Figure 56.

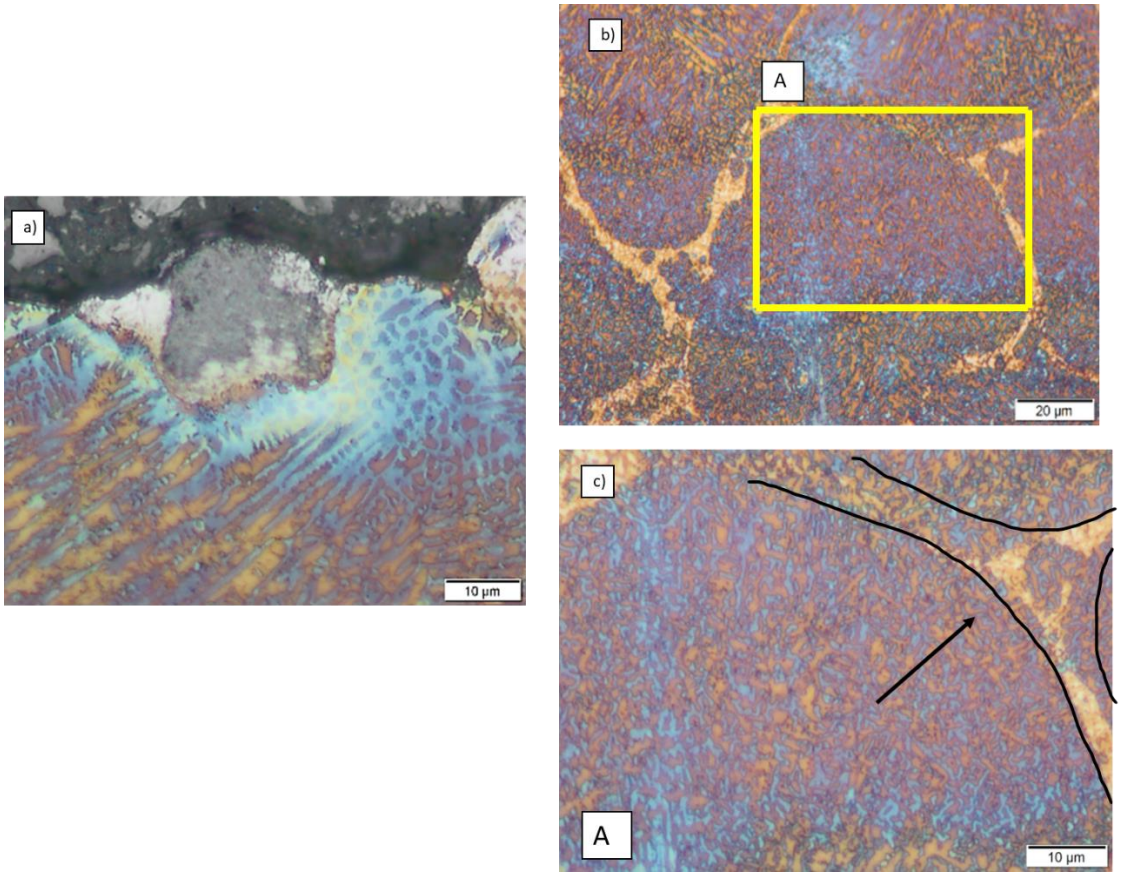

Figure 56. OM images depicting the microstructure of a) top layer b) center of the sample c) amplified zone A of the sample center

SEM analysis performed also depicted differences between the zones inside the samples. Different microstructures were present in the top layer, in the heat affected zone (HAZ) and in the middle of the sample. Each zone was designated as zone 1, 2 and 3 respectively.

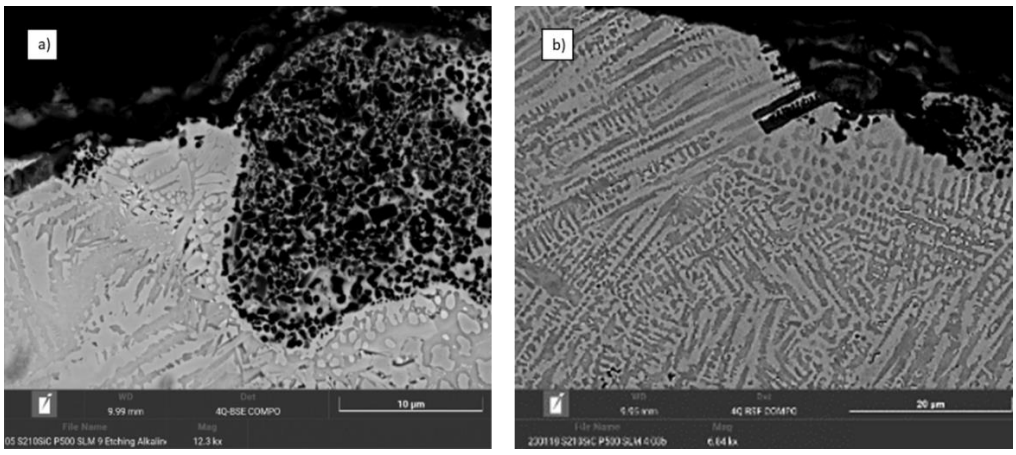

Figure 57. SEM of the top layer of S2 + 10%SiC P500 sample at different zones and a) 12.3 kx magnification b) 6.84 kx magnification

Figure 57 depicts clear elongated dendrites as the ones that were seen with the OM. In the HAZ, however, it can be observed a zone with no elongated dendrites with a white phase growing inside the darker zone, shown in zone 2AA of Figure 58.

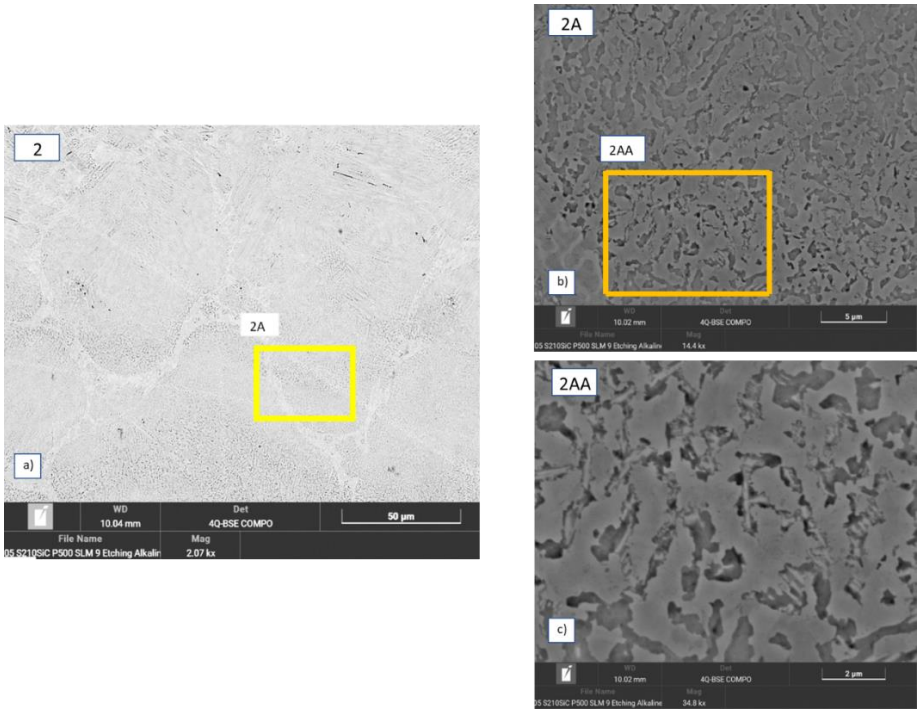

Figure 58. SEM images of the HAZ microstructure of sample 9 with P500 at a) zone 2 b) zone 2A c) zone 2AA

Similarly, in the center of the sample a non-elongated microstructure is obtained. In certain zones, epitaxial growth in the melt pool is well identified, as can be seen in Figure 59.

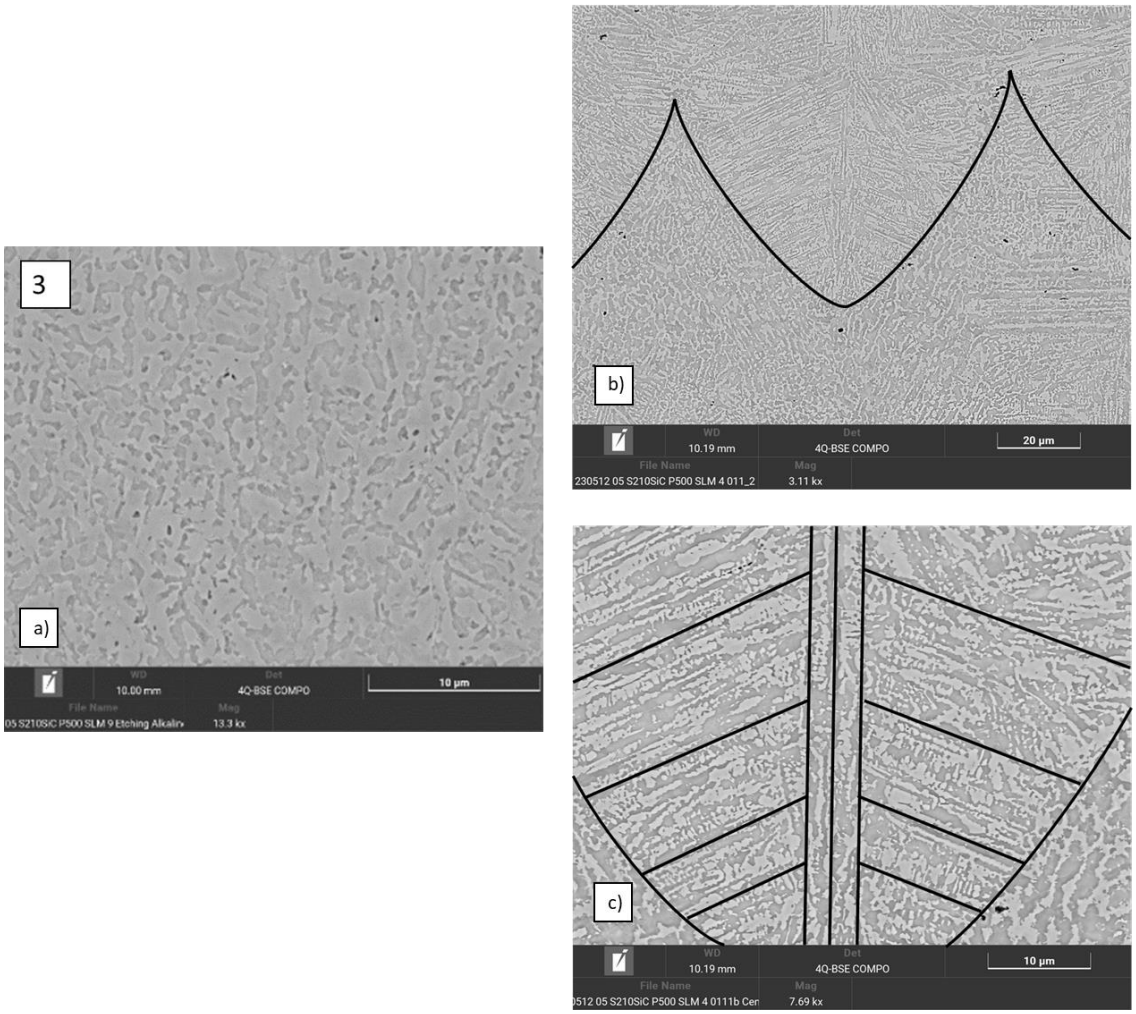

Figure 59. SEM images of the center of the preheated sample 9 showing a) general microstructure b) morphology of the melt pools c) epitaxial growth

Having seen that different phases are present inside the preheated sample, EDX analysis was performed to better identify them. It was also evaluated in zones 1, 2 and 3.

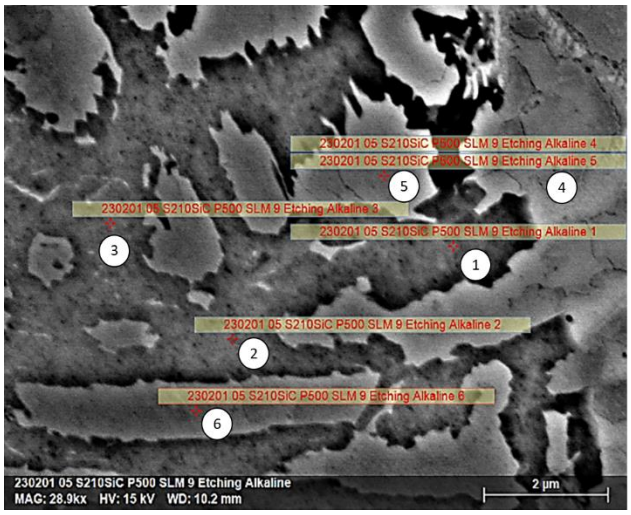

POINTS	Carbon	Oxygen	Sodium	Silicon	Manganese	Iron	Molybdenum
1,2,3	8,133	5,606	1,750	8,356	0,370	75,483	0,303
STD	0,61	0,96	0,38	0,92	0,11	2,80	0,13
4,5,6	3,883	3,170	0,856	8,073	0,316	83,610	0,090
STD	0,30	1,48	0,36	0,33	0,06	1,47	0,03

Figure 60. Composition in atomic % of phases in zone 1 of sample 9 with preheating

In the top layer the composition of each phase was evaluated. There were 2 differentiable phases also seen in OM and SEM analysis. 3 points in each phase were considered. The composition is the average between the 3 points of the same phase. The results can be seen in Figure 60. Moreover, in the HAZ the additional phase identified in Figure 58 was also analysed. In this figure, points 1,2,3 are this new phase formed in between the dark zones.

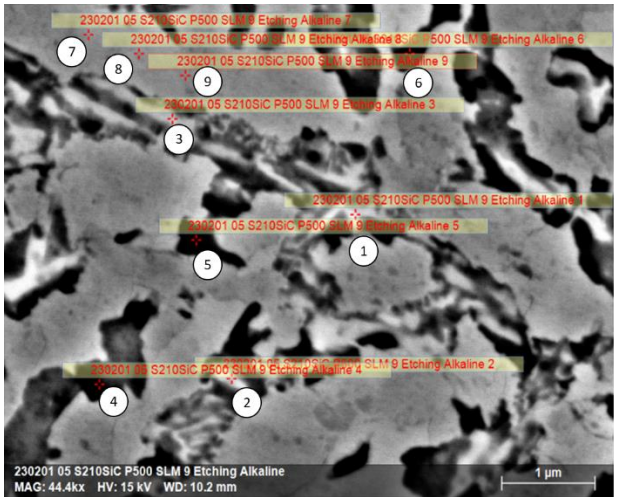

POINTS	Carbon	Oxygen	Sodium	Silicon	Manganese	Iron	Molybdenum
1,2,3	10,82	4,37	1,31	6,50	0,37	76,11	0,50
STD	2,08	0,64	0,11	1,17	0,07	1,66	0,18
4,5,6	8,41	4,14	1,40	6,68	0,36	78,64	0,35
STD	2,85	0,81	0,06	0,38	0,13	2,60	0,38
7,8,9	4,46	3,85	1,04	7,11	0,30	83,10	0,10
STD	0,17	0,25	0,12	0,01	0,03	0,34	0,05

Figure 61. Composition in atomic % of phases in zone 2 of sample 9 with preheating

Finally, in the center of the sample apart from the three different zones present in Figure 61, the grain boundaries also stand out. Because of that, the composition of this phase was also evaluated. The composition that represents the yellow grain boundaries depicted in the Alkaline sodium picrate image taken with the OM (Figure 56) is point number 1.

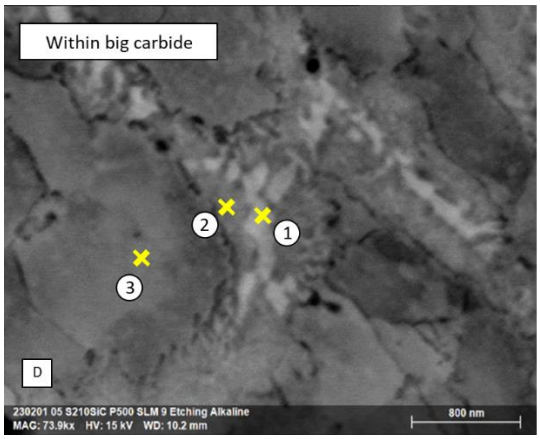

POINTS	Carbon	Oxygen	Silicon	Manganese	Iron	Molybdenum
1	9,40	4,17	6,98	0,34	78,66	0,43
STD	1,23	0,58	0,75	0,09	1,25	0,23
2	5,09	2,75	7,79	0,41	83,68	0,25
STD	0,19	0,22	0,19	0,05	0,22	0,04
3	4,63	2,03	7,81	0,28	85,13	0,10
STD	0,65	0,61	0,28	0,07	0,73	0,02

Figure 62. Composition in atomic % of the center of the preheated sample

Finally, EBSD analysis was also performed in both preheated and non-preheated samples. As seen in Figure 63, identified phases are higher in the non-preheated sample because of the zero solution.

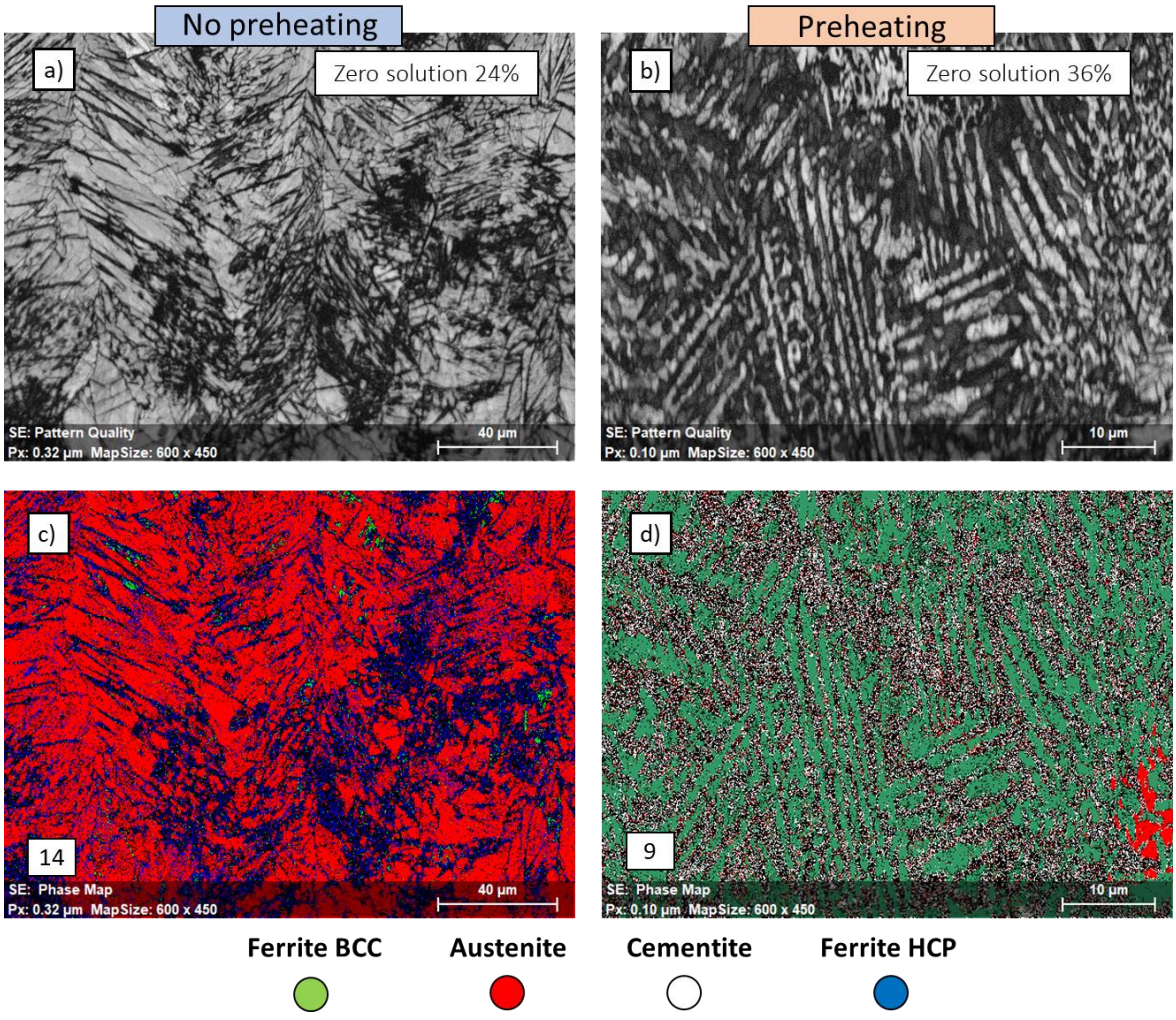

Figure 63. EBSD images a) Pattern Quality of non-preheated sample b) Pattern Quality of preheated sample c) Phase Map of non-preheated sample d) Phase Map of preheated sample

In the non-preheated sample, the pattern quality shows a needle-shaped structure of non-identified phases surrounded by recognised austenite. Apart from that, some ferrite HCP was also identified. Thus, the typical structure of martensite needles plus austenite is highly probable, also considering previous studies seen in the paragraph 2.3. On the other hand, a pattern quality in form of elongated dendrites is obtained when preheating is added. The main phase or dendrites are identified as BCC ferrite. The phase in between the dendrites, though, is not-well identified. However, some cementite is represented. There are some concrete zones, also, that have punctual concentrations of austenite but are not abundant.

Also, the IPF showed relevant differences between preheated and non-preheated samples. Non-preheated samples tend to grow the grains epitaxially whereas preheated ones have a more uniform and not epitaxial growth of grains.

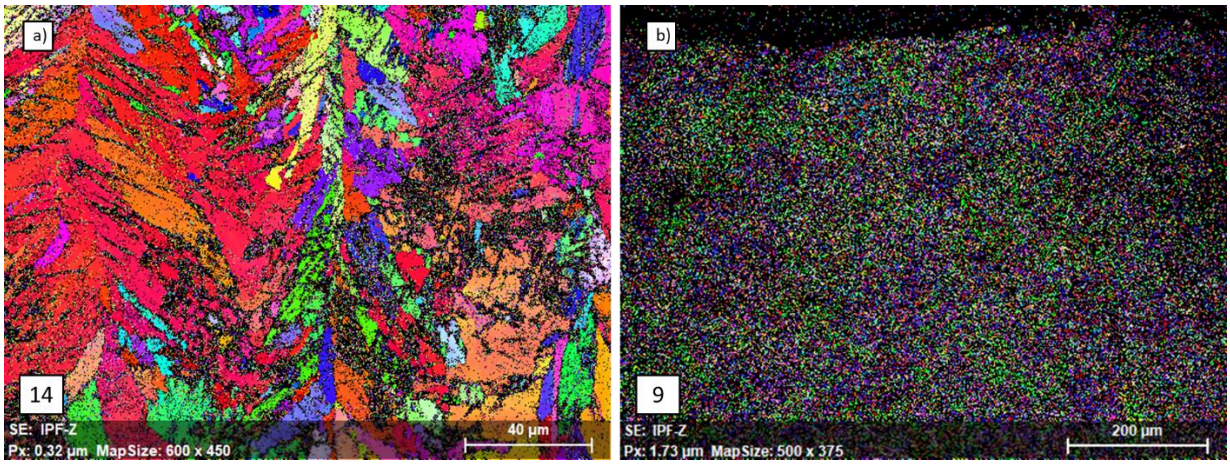

Figure 64. IPF in Z direction of a) non-preheated sample 14 b) preheated sample 9

4.2.6 DTA

The DTA results help to understand the transformations happening during the printing process and, thus, the final phases that are present. For this study, only a limited part of the heating curve (up to 1000°C) was considered. The results of the analysis were the following:

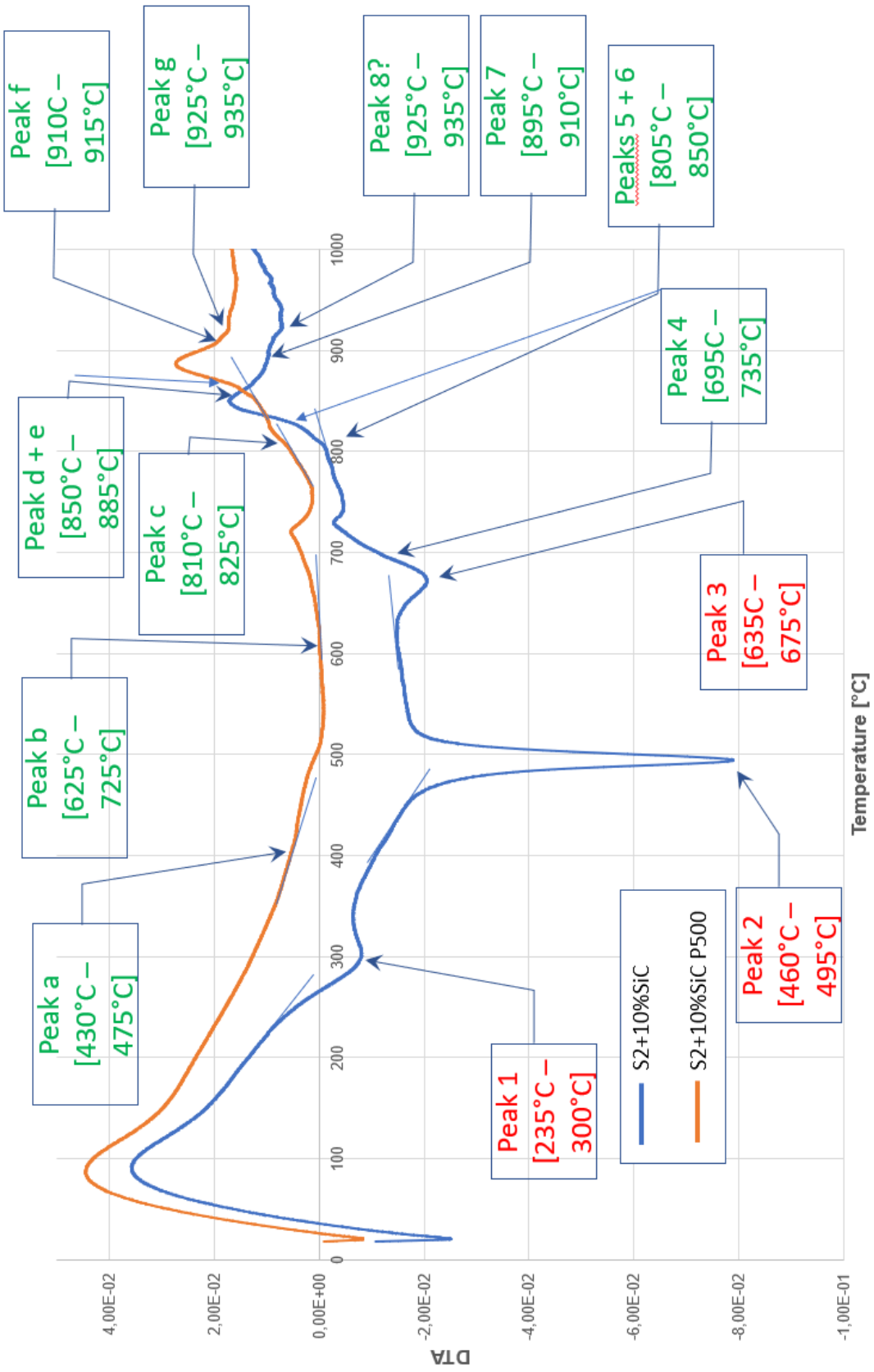

Figure 65. DTA of preheated and non-preheated samples

A summarizing table is constructed to see the most relevant peaks and its reactions:

Peak	Start temperature [ºC]	End temperature [ºC]	Reaction or phase transformation
1	235	300	Precipitation of secondary carbides
2	460	495	Precipitation of type II carbides
3	635	675	Martensite to ferrite + carbides type III
4	695	735	Austenitization
5 + 6	805	850	Dissolution of carbides type I and II
7	895	910	Dissolution of carbides type III
8	925	935	Dissolution linked to HAZ
a	430	475	Dissolution of carbides
b	625	725	Bainite to austenite
c	810	825	Dissolution of carbides
d + e	850	885	Dissolution of carbides
f	910	915	Dissolution of carbides type III
g	925	935	Dissolution linked to HAZ

Table 16. Principal DTA peaks of S2 + 10%SiC

4.2.7 Hardness

Macrohardness tests have been performed in non-preheated sample 14 and preheated sample number 9. A grid of indentations was done at HV5. The top layer, though, was perforated at HV1 as explained in section 3.6.

The average value for each row was calculated to see the tendency of hardness as a function of the distance to the substrate. The average value of all the sample disregarding the value of the top layer

(which can have a very different value from the rest of the sample) is noted on the bottom of the graph (564 HV preheated sample and 624 HV non-preheated). The value of the top layer hardness is 550 HV and 523 HV respectively). The standard deviation in each row is also represented to see if the values follow similar values in the same row or not.

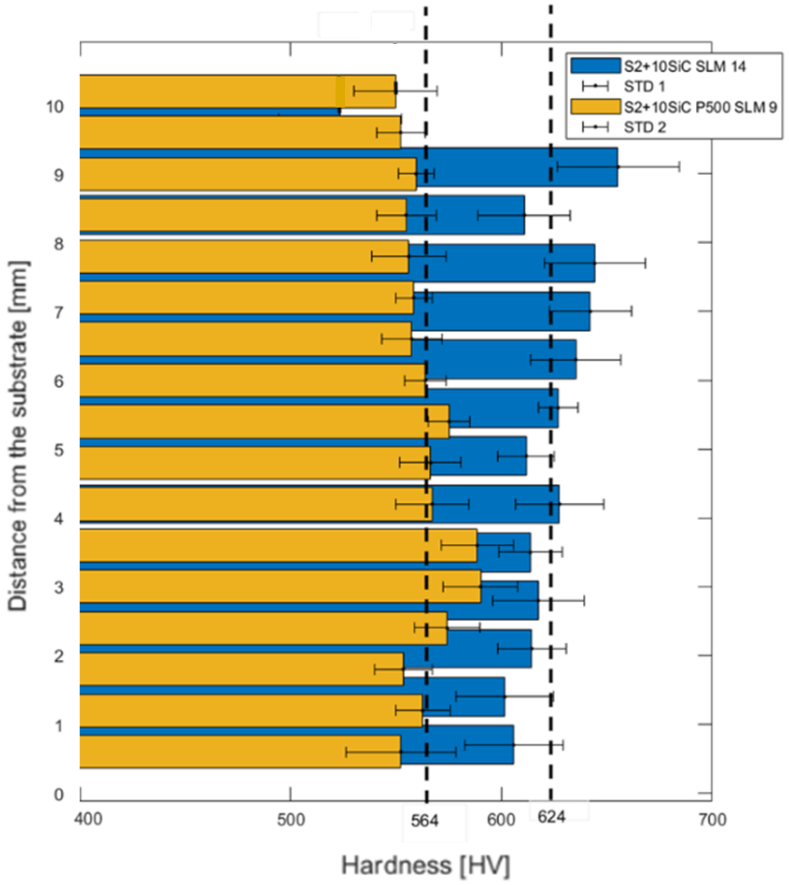

Figure 66. Hardness values as a function of the distance to the substrate of batch 1 and 2

The values of hardness clearly differ from one another. In sample number 14, the average value of the rows is way higher than the average of sample number 9. Despite that, the top layer value of hardness is higher in sample 9 than in sample 14. Moreover, the general values in the non-preheated sample are so different compared to the top layer one. In the preheated sample the values are similar though.

5 DISCUSSION

The aim of this work is to develop the alloy S2 + 10% (in vol.) SiC by LPBF. In a previous work of the same team "Fabrication and characterization of low-alloyed tool steel obtained by Selective Laser Melting," 2023 [1], the tool steel AISI S2 was processed by LPBF as material reference. Therefore, in this chapter will be explained the effect of SiC addition on the processability and on the microstructure. In particular, a comparison between S2 and S2 + 10%SiC is done. Moreover, since a substrate preheating to obtain fully dense, defect-free samples of S2 + 10%SiC was applied during the LPBF process, the effect of the preheating will be discussed.

5.1 Shifting of the Process Map

The ultimate objective of this work is to find the optimal process parameters to obtain fully dense, defect-free samples with the composition S2 + 10% (in vol.) SiC. Therefore, different combinations of parameters were tested and their effect on the final part was studied, with particular attention to the influence of the VED. Finally, a process map was developed by combining the results of the density evaluation, the percentage of porosity and the types of defects. The main factor that has been identified as influencing on finding the optimal parameters is the preheating.

The parameters for the production of batch 1 (S2+10%SiC without preheating) were selected starting from the process map of the tool steel AISI S2, visible in Figure 67.

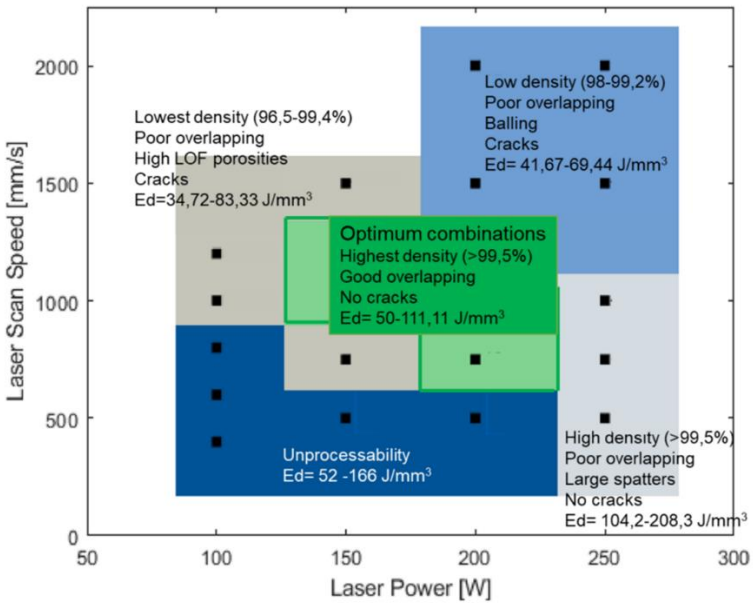

Figure 67. Process map of S2 samples built by LPBF

Since SiC is added in 10% in volume, a high amount of carbon is present. According to previous studies, it affects the processability because increases the tendency of crack appearance. This is due to a reduction of wettability of the melt pool and the carbide formation that lead to embrittlement. [78][5][4]. Furthermore, it shifts the parameters at which certain defects appear [4] and, consequently, the parameters at which optimal samples are produced. Therefore, from the process map of AISI S2 only limited combinations of parameters were chosen. In particular, laser power of 150, 175 and 200 W and scan speed ranging from 400 to 1000 mm/s.

The results were indeed different. Sample number 13 was the only with scan speed of 1000 mm/s and resulted in such a low density compared to the others of the same batch (considering the sample with higher density of the same batch, its density is 15% lower). The rest of the samples were in between 150 - 200 W and 400 - 800 mm/s and had similar high density. This differs from the only S2 samples since the same parameters resulted in unprocessable samples and samples with low density. Only the sample of 200 W and 750 mm/s in this range was an optimal high-density sample.

When it comes to the percentage of porosity seen in the 2D images, in non-preheated samples we find 3 different samples with porosity values under 0.1%. These are samples with high power (175-200 W) and 700 – 800 mm/s. The rest of the samples have similar percentages, around 0.8%, except for sample number 10. It is the only one with a scan speed of 400 mm/s and has a porosity around 2.2%. Then, we can distinguish samples with really good, with regular and with bad values of porosity.

Related to the percentage of porosity, the types of porosity appearing in the samples depend also on the VED. Table 14 depict the different types of porosity that appear in each sample and it was confirmed that high VED generates keyhole porosity and low VED generates LOF. With the addition of SiC, however, LOF starts at samples with lower VED than 104 J/mm^3whereas with only S2 starts at 83 J/mm^3. Similarly, the optimal combination is also shifted towards higher VED (91 – 119 J/mm^3 in comparison to the 50 – 111 J/mm^3 of the only S2.

Therefore, the conclusion that SiC shifts the process map towards higher VED can be taken. The resulting process map of S2 + 10%SiC with no preheating can be seen in Figure 68.

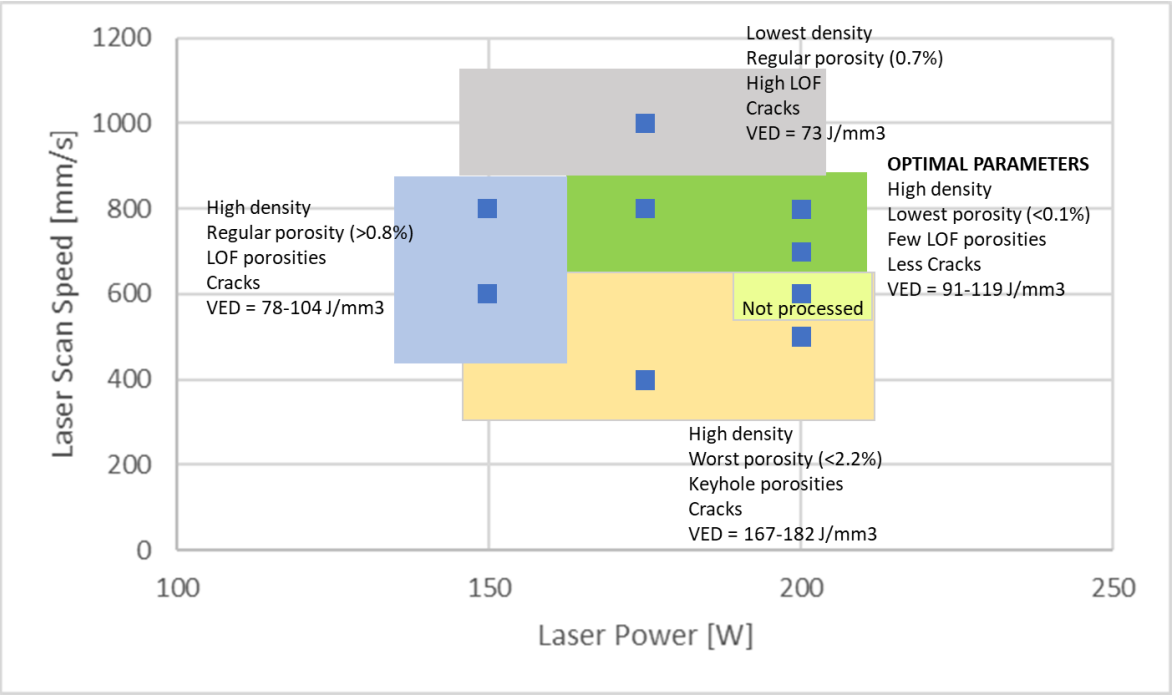

Figure 68. Process map of S2 + 10%SiC built by LPBF without preheating

However, despite some few parameters combinations that is possible to achieve high density and few defects, all the samples show cracks. In order to avoid cracks, previous works already shown the beneficial effect of the preheating [82], [85], [87], [110]. Therefore, a second batch of samples with the same powders (S2+10%SiC) was processed by applying a substrate preheating of 500°C. Indeed, after production, all samples did not exhibit cracks. Moreover, for this batch, a further refinement of the parameters was done starting from the process map obtained from the first batch without preheating. In particular, the samples of 150 W were excluded because of the bad previous results. The samples were focused on 175 W with lower scan speed (500 – 700 mm/s) and 200 W with higher scan speed (600 – 1200 mm/s).

Comparing the two batches with and without preheating, a further shifting of the process map is visible. Regarding the density, the only sample with 500 mm/s of scan speed of the preheated batch stands out for a lower density compared to the others (5% lower density). Therefore, the worst parameters in terms of density were in a range considered acceptable in samples without preheating. The rest of the samples of the batch can be considered as fully dense (maximum 2% lower density).

Moreover, in the preheated batch we can also see samples between 600 and 700 mm/s with really good values of porosity (porosity < 0.1%) and the other samples with regular porosity values. There are not really bad values of porosity since the worse one is 1.2%. In the non-preheated batch, samples such as the one with 800 mm/s and 200 W were considered of bad porosity whereas with preheating it was one of the best. Preheating generates a general shifting in terms of porosity as well.

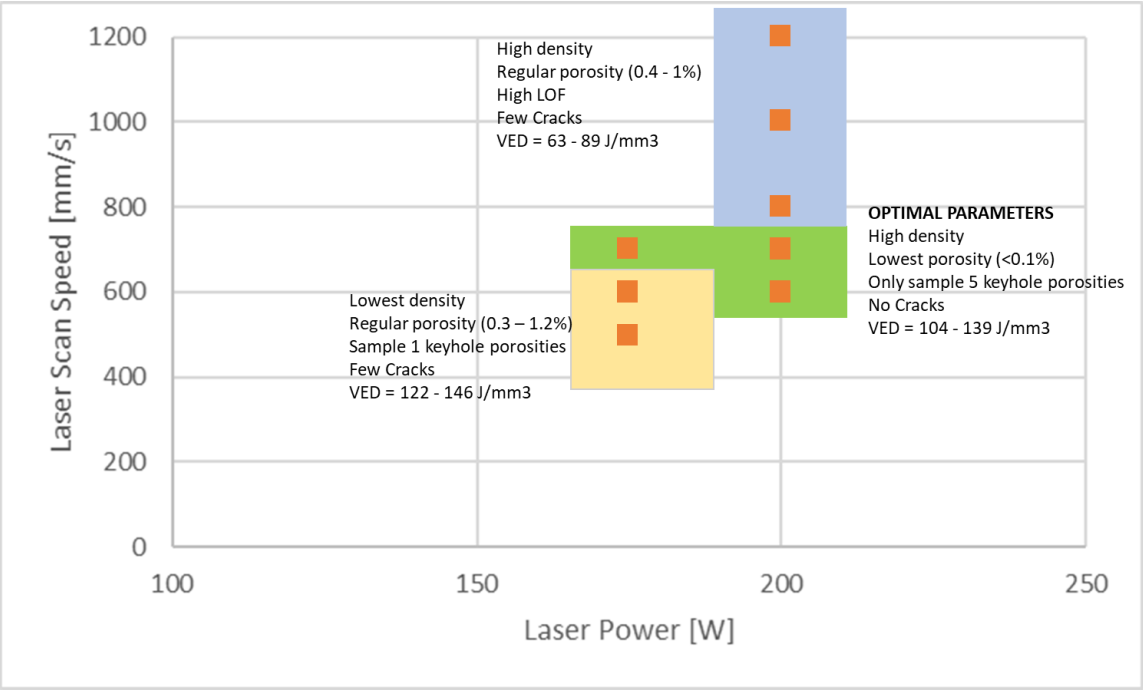

Figure 69. Process map of S2 + 10%SiC built by LPBF with preheating at 500°C

Considering the three processes map, the optimal parameters have been definitely shifted even though the bests samples have the same parameters in both S2 + 10%SiC batches. In the case of only S2 the optimal parameters were around 50 - 111 J/mm^3. With the addition of SiC, the optimal is shifted into higher VED (91-119 J/mm^3). If finally preheating is added, the optimal is slightly shifted towards 104 - 139 J/mm^3. This changes are due to the SiC and preheating effect.

5.2 SiC effect on cracks appearance

As explained at the beginning of this chapter, comparisons with the work on the development of S2 as material reference are necessary to understand the effect of SiC addition. S2 samples did not show cracks after the process. On the other hand, all the samples made of S2 + 10%SiC exhibit cracks. The appearance of cracks is due to the carbon within the samples.

The first thing to note is that the range of low porosity values decreases with the addition of SiC, as seen in Figure 48. This is something that has been seen in different studies with increasing carbon content [4]. This carbon increment tends to increase porosity values, making it more difficult to find acceptable values of porosity. This is because with the addition of SiC there is a reduction of the melt pool wettability [78]. In case of S2 + 10%SiC, the acceptable values are not exactly in the middle of the S2 range but a little shifted towards higher VED. This can be related to Figure 54, that shows that in order to get the same melt pool size, more VED is needed for S2 + 10%SiC. Since depending on

the melt pool size porosities appear, if more VED is needed to have the same melt pool logically more VED is needed to reach the acceptable values of porosity.

The top layer depth is also affected by SiC. The fact that with higher VED deeper top layers are obtained is due to the increase of energy given to the powders, that results in deeper melt pools that can be better seen in the top layer. Apart from that, S2 samples have higher top layer values than the batches with SiC for the same VEDs. Therefore, it can be said that the addition of nanoparticles decreases the depth of the melt pool. A possible explanation can be related to the melting point. SiC have a much higher melting point than S2. Because of that, when SiC is added, the powders in the border of the melt pool will not reach the needed temperature to melt. Thus, the melt pool will be reduced since a fraction of powders that would melt with only S2 will not when adding SiC [111].

Apart from that, the characterization of the S2 microstructure showed the presence of martensite in the whole sample. In-situ thermal treatments natural from LPBF distinguished different types of martensite inside the sample, though. In the top layer untampered martensite was identified along with an austenitization zone. However, due to the heat of next layers, a tempering of the martensite occurs in all the other layers [1]. When SiC is added, though, big needles of martensite can be seen in the OM surrounded by retained austenite. SiC turns the microstructure into a much more austenitic structure, where the martensite is joined by retained austenite that could not reach Ms. This is due to the carbon content increment, that reduces Ms temperature of the samples. Therefore, martensite is not reached in that many zones of the sample, staying as austenite.

Similarly, looking at Figure 63 phase map, it can be seen that the main phase recognised is austenite whereas the non-recognised parts have the needle-shape typical from the martensite. As seen in previous studies, tool steels usually solidify as martensite plus retained austenite due to out-of-equilibrium conditions [81]. High cooling rates and high carbon content end up in martensitic supersaturated structures with high internal stresses. This first approach is reaffirmed when looking at DTA, that confirms these final phases. Looking at Figure 65, S2 + 10%SiC have 3 marked exothermic peaks, meaning supersaturation phases, followed by a group of endothermic ones. First, peak 1 is an exothermic reaction that should be related to the precipitation of secondary carbides inside the martensitic phase in a supersaturated state. Sharp exothermic peak 2 may correspond to the precipitation of carbides type II along with a significant heat released. Later, martensite turns into ferrite and carbides in peak 3. Peak 4 correspond to a broad endothermic peak, which is austenitization. Finally, peaks 5 + 6, 7 and 8 may correspond to a dissolution of previously precipitated carbides.

Therefore, it can be said that all the results lead to the typical tool steel microstructure, with martensite needles plus retained austenite due to high carbon content that reduce martensite formation. Furthermore, two different types of martensite are formed during the printing process.

The first one, and the most typical one, is formed due to the rapid cooling (BCC). The second, is known as "ε martensite" and is formed due to high amount of stresses, the same ones that generate cracks (HCP).

Also, Figure 64 show long elongated grains growing epitaxially that are typical also of LPBF fabricated tool steels with no preheating. The thermal gradient in the middle of the sample causes the formation of elongated grains following the building direction and the heat flow. Nevertheless, it has been identified that SiC influences slightly the epitaxial growth reduction. SiC increases the absorptivity of the sample. Then, it has the capacity to absorb more energy and takes more time to solidify after the laser melting. Indeed, less cooling rate is affecting the sample. Because of that, there will be less thermal gradient since the previous layer is going to be hotter when another layer is added on top. The main reason for epitaxial growth formation is the grains following the heat flow generated by the thermal gradient. If the thermal gradient is reduced, epitaxial growth is also reduced.

Summarizing, SiC changes the type of microstructure, which results in different martensite type and consequently higher residual stresses within the microstructure. This causes cracks nucleation and propagation during the printing process.

5.3 Advantages of substrate preheating

As explained in chapter 5.2, the addition of SiC cause cracks in all the samples. Therefore, since the goal is to obtain a part defects-free, a substrate preheating of 500°C was applied. As explain in chapter 5.1, no cracks were detected after the printing process. This is due to the effect of the preheating on the microstructure that reduces the internal stresses and affects all the properties of the samples.

In Figure 48, the range of acceptable porosity values is increased again with the addition of preheating. This phenomenon reduces the internal thermal gradient and the internal stresses, giving samples with less porosities and less cracks [86]. It can also be observed that the acceptable VEDs for non-preheated samples are again inside the range of acceptable values of the preheated ones. These values, however, are shifted towards less VED inside preheated-samples range. Similar to the previous section, it can be related to the top layer depth. If, according to Figure 54, less VED is needed to obtain the same top layer depth, makes sense that less VED is needed to obtain low porosity values. Overall better results in the defects can be related to the reduction of porosity caused by the addition of a preheated baseplate.

Moreover, regarding Figure 54, as mentioned before, it can be seen that preheating also slightly shifts the tendency line of the non-preheated samples. The effect is a little increase of the top layer depth.

The powders are not only receiving input energy from the laser but also from the baseplate. Overall, more energy is given to the powders increasing the size of the melt pool.

When it comes to the microstructure, indeed, applying a preheating reduce the thermal gradient and solidification rates. This thermal gradient and high solidification rates typical from LPBF lead to internal stresses and supersaturated structures that end up in cracks [85]. With the reduction of the solidification rate no martensite can be formed, so no brittle supersaturated phase is present, as seen in the DTA. Of course, OM and EBSD images do not show the typical martensitic needles that could be observed without preheating (Figure 55 and Figure 63). Instead, since the cooling rates are lower, a different type of microstructure is formed.

The first thing to consider is that, as previously seen and according to the DTA, no exothermic reactions are present in the solidification process. That means no precipitation occurs so no supersaturation is present in the sample. With that being said, Figure 63 depicts that the main recognised phase is BCC ferrite in form of elongated dendrites. However, since no supersaturated phases are present in the sample it is considered as BCC "bainitic ferrite". This phase can be well seen in Figure 57 and it corresponds to the darker "islands" or upper phase present in the SEM of the top layer. It will be named phase 1. When alkaline sodium picrate etching is applied, this phase is seen as brown dendrites.

In the printing process, then, the first solidification steps after the melting of the laser can be seen in the top layer since no heat of further layers is involved in the microstructure. It can be observed in Figure 57 the solidification in form of dendrites of the bainitic ferrite and another phase richer in carbon and molybdenum (Figure 60). This whiter zone, or the surroundings of the dendrites phase, is assumed to be cementite and will be named as phase 2. This phase is not well identified according to the pattern quality but in the phase map is shown as basically cementite. When this lack of recognition happens, is normally because the phase is supersaturated or because of distortions. Since there are no supersaturated phases according to the DTA, the cementite is present as a distorted phase due to out-of-equilibrium conditions. In the etching, this phase can be recognized for its blue colour.

When other layers are put on top, in the HAZ a precipitation inside the cementite occurs due to the heat, converting the previous cementite into precipitates and more cementite, this time less rich in Silicon. Figure 58 shows this white precipitates inside the cementite phase. Furthermore, in this HAZ a general refinement of the microstructure occurs, as seen in Figure 58, turning the bainitic ferrite dendrites into a much more homogeneous, uniform and coarser zone. Finally, in every zone, but better seen in the middle of the sample (zone 3), we find well identified with the alkaline sodium picrate the grain boundaries. They are yellow, as seen in Figure 56.

Summarizing the printing process, it can be assumed that from the liquid a nucleation of austenitic dendrites takes place. The parts remaining turn into cementite. From this austenite dendrites, a

transformation occurs turning them into bainitic ferrite because of the lower cooling rates due to preheating and the carbon going to the cementite phase. Without this preheating, martensite would have been formed. Later, in HAZ, much finer microstructure with no dendrites is obtained, so a process of precipitation along with a general refinement takes place.

As a summary of the phases present in S2 + 10%SiC P500, a table is constructed.

Phase	Microstructure	Pattern Quality	Phase Map	SEM	Alkaline Sodium Picrate
1	Bainitic Ferrite	White	Green	Upper phase	Brown
2	Cementite	Dark	White/dark	Surroundings	Blue
3	Precipitates	Dark	Dark	Inside phase 2	Not visible
4	Grain boundaries	Dark	Dark	Not identified	Yellow

Table 17. Phases present in S2 + 10%SiC P500 microstructure

Also, the composition of each phase can be also discussed according to the results taken. Stands out that phases 3 and 4 are richer in molybdenum than phases 1 and 2. The quantity of carbon in phase 2 is higher (more than doubled) than in phase 1 and even higher in phase 3 and 4, being phase 3 the highest percentage (10.82%). The percentage of silicon is similar in phases 1 and 2 and also similar in 3 and 4, being these two lower than 1 and 2. It is also worth noting that the same phase may not necessarily have the same composition in all the zones of the sample. Phase two in the HAZ has less silicon content than in the top layer, maybe due to a dissolution into the other phases.

When it comes to the epitaxial growth of the grains, Figure 64 shows a clear non-epitaxial growth with the IPF analysis. However, Figure 59 depicts epitaxial growth with the EBSD. Therefore, we can say that due to the preheating and SiC, epitaxial growth is reduced. Is not reduced enough to not see it in any part of the sample but is reduced because IPF cannot identify the epitaxial grains. This conclusion, however, needs further evaluation.

6 CONCLUSIONS

From the fabrication and characterization of S2 + 10%SiC samples processed by LPBF, the following conclusions can be drawn up.

- Adding 10% of SiC to the tool steel S2 shifts down and narrows the process map compared to that of S2. The trend is even greater for S2 + 10%SiC processed with preheating compared to S2. With S2 alone, the optimal processing parameters lead to a VED between 50 – 111.11 J/mm^3, which switches to 91-119 J/mm^3 for S2 + 10%SiC without preheating, and to 104 – 139 J/mm^3 if preheating at 500°C is performed for the MMC.

- The processing maps achieved on both MMCs batches lead to fully dense samples. Nevertheless, preheating is required to obtain crack-free samples. Cracking that occurs during processing of S2 + 10% SiC without preheating is due to both the carbon content and the characteristic out-of-equilibrium conditions of LPBF that together result in the formation of martensite and the presence of high amount of residual stresses.

- The addition of SiC nanoparticles to AISI S2 changes several properties. Firstly, there is a decrease of the density of the MMC compared to S2 due to the lower density of the added SiC. Secondly, increasing the carbon content decreases the acceptable range of porosity values due to the reduction of the melt pool wettability. Nevertheless, the enhanced carbon content also promoted cracks occurrence, but this can be inhibited when using preheating. Furthermore, the reduction of the melt pool size can be related to the higher melting point of SiC, that reduces the zone of powders that will reach the temperature needed to melt.

- The microstructure obtained in S2 + 10%SiC without preheating is martensite plus retained austenite because the addition of SiC increase the carbon content which lowers the temperature range for martensitic transformation, the final point being assumed to be far below room temperature. Two different types of martensite are present, the thermal one that is formed due to the rapid cooling (BCC) and another (HCP) formed via deformation due to high amount of internal residual stresses. Consequently, both the martensitic transformations and the higher residual stresses within the microstructure will promote cracks during the printing process.

- Preheating effect yields a slightly higher density within the samples. Besides, the melt pool size is also increased as seen on the top layer. Preheating allows the formation of bainite instead of supersaturated martensite, thus lowering the level of internal stresses while

avoiding the formation of cracks at the same time. In addition, other new phases like cementite at grain boundaries or small carbides inside grains are formed due to preheating.

- Regarding the solidification structure, preheating decreases thermal gradients which helps to wipe out the epitaxial growth that usually occurs under AM processes. SiC also helps erasing the epitaxial growth while increasing the absorptivity on the sample, which decrease the cooling rate.

7 PERSPECTIVES

Further investigations can be done related to this thesis:

- Perform XRD, quenching dilatometer, nanoindentation and DTA in liquid state tests to better understand the in-situ thermal treatments and the microstructure phases present.
- Perform wear tests to the as-printed parts to validate and compare them between each other and between only S2 samples.
- Develop finite element method with Thermo-Calc to predict thermal history. With its new AM section, it is easier to simulate LPBF conditions and to evaluate the material response and behaviour.

8 BIBLIOGRAPHY

[1] E. FILIPPI, “Fabrication and characterization of low-alloyed tool steel obtained by Selective Laser Melting,” 2023, Accessed: Apr. 30, 2023. [Online]. Available: https://thesis.unipd.it/handle/20.500.12608/36367

[2] R. Duan *et al.*, “In situ alloying based laser powder bed fusion processing of β Ti–Mo alloy to fabricate functionally graded composites,” *Compos B Eng*, vol. 222, p. 109059, Oct. 2021, doi: 10.1016/J.COMPOSITESB.2021.109059.

[3] C. Tan, W. Ma, C. Deng, D. Zhang, and K. Zhou, “Additive manufacturing SiC-reinforced maraging steel: Parameter optimisation, microstructure and properties,” *Advanced Powder Materials*, vol. 2, no. 1, p. 100076, Jan. 2023, doi: 10.1016/J.APMATE.2022.100076.

[4] W. Hearn and E. Hryha, “Effect of Carbon Content on the Processability of Fe-C Alloys Produced by Laser Based Powder Bed Fusion,” *Front Mater*, vol. 8, p. 547, Jan. 2022, doi: 10.3389/FMATS.2021.800021/BIBTEX.

[5] J. Saewe, N. Carstensen, P. Kürnsteiner, E. A. Jägle, and J. H. Schleifenbaum, “Influence of increased carbon content on the processability of high-speed steel HS6-5-3-8 by laser powder bed fusion,” *Addit Manuf*, vol. 46, Oct. 2021, doi: 10.1016/J.ADDMA.2021.102125.

[6] “Impresión 3D: qué es, métodos, aplicaciones, materiales e impresoras 3D.” https://www.adslzone.net/reportajes/tecnologia/impresion-3d/ (accessed Feb. 23, 2023).

[7] “Document.” https://www.ecampus.uliege.be/ultra/courses/_1775_1/outline/edit/document/_777981_1?courseId=_1775_1&view=content (accessed Feb. 24, 2023).

[8] J. Schweiger, D. Edelhoff, and J.-F. Güth, “3D Printing in Digital Prosthetic Dentistry: An Overview of Recent Developments in Additive Manufacturing,” *Journal of Clinical Medicine 2021, Vol. 10, Page 2010*, vol. 10, no. 9, p. 2010, May 2021, doi: 10.3390/JCM10092010.

[9] T. D. Ngo, A. Kashani, G. Imbalzano, K. T. Q. Nguyen, and D. Hui, “Additive manufacturing (3D printing): A review of materials, methods, applications and challenges,” *Compos B Eng*, vol. 143, pp. 172–196, Jun. 2018, doi: 10.1016/J.COMPOSITESB.2018.02.012.

[10] “What is 3D printing? How does 3D printing work? | Hubs.” https://www.hubs.com/guides/3d-printing/ (accessed Feb. 24, 2023).

[11] R. J. Friel, “Power ultrasonics for additive manufacturing and consolidating of materials,” *Power Ultrasonics: Applications of High-Intensity Ultrasound*, pp. 313–335, 2015, doi: 10.1016/B978-1-78242-028-6.00013-2.

[12] G. Roger Vila, “Estudio de las aplicaciones nuevas y futuras de la impresión 3D en el àmbito ingenieril,” 2021, Accessed: Feb. 24, 2023. [Online]. Available: https://upcommons.upc.edu/handle/2117/353529

[13] “Additive manufacturing technologies poster | Hubs.” https://www.hubs.com/get/am-technologies/ (accessed Apr. 27, 2023).

[14] “3D Printing, What is it and how does it work? | Dassault Systèmes®.” https://www.3ds.com/make/guide/process/3d-printing (accessed Apr. 27, 2023).

[15] “Generalized steps of 3D printing process [7] | Download Scientific Diagram.” https://www.researchgate.net/figure/Generalized-steps-of-3D-printing-process-7_fig1_334544502 (accessed Apr. 27, 2023).

[16] “Schematic illustration of the LPBF powder delivery system [84] | Download Scientific Diagram.” https://www.researchgate.net/figure/Schematic-illustration-of-the-LPBF-powder-delivery-system-84_fig5_339437450 (accessed Mar. 14, 2023).

[17] N. Guo and M. C. Leu, “Additive manufacturing: technology, applications and research needs,” *Frontiers of Mechanical Engineering 2013 8:3*, vol. 8, no. 3, pp. 215–243, May 2013, doi: 10.1007/S11465-013-0248-8.

[18] D. Wang *et al.*, “Mechanisms and characteristics of spatter generation in SLM processing and its effect on the properties,” *Mater Des*, vol. 117, pp. 121–130, Mar. 2017, doi: 10.1016/J.MATDES.2016.12.060.

[19] J. Platl, H. Leitner, C. Turk, A. G. Demir, B. Previtali, and R. Schnitzer, “Defects in a Laser Powder Bed Fused Tool Steel,” *Adv Eng Mater*, vol. 23, no. 12, p. 2000833, Dec. 2021, doi: 10.1002/ADEM.202000833.

[20] J. Kunz, J. Saewe, S. Herzog, A. Kaletsch, J. H. Schleifenbaum, and C. Broeckmann, “Mechanical Properties of High-Speed Steel AISI M50 Produced by Laser Powder Bed Fusion,” *Steel Res Int*, vol. 91, no. 5, p. 1900562, May 2020, doi: 10.1002/SRIN.201900562.

[21] S. R. Narasimharaju *et al.*, “A comprehensive review on laser powder bed fusion of steels: Processing, microstructure, defects and control methods, mechanical properties, current challenges and future trends,” *J Manuf Process*, vol. 75, pp. 375–414, Mar. 2022, doi: 10.1016/J.JMAPRO.2021.12.033.

[22] J. P. Oliveira, A. D. LaLonde, and J. Ma, "Processing parameters in laser powder bed fusion metal additive manufacturing," *Mater Des*, vol. 193, Aug. 2020, doi: 10.1016/J.MATDES.2020.108762.

[23] M. A. Buhairi *et al.*, "Review on volumetric energy density: influence on morphology and mechanical properties of Ti6Al4V manufactured via laser powder bed fusion," *Progress in Additive Manufacturing 2022 8:2*, vol. 8, no. 2, pp. 265–283, Jul. 2022, doi: 10.1007/S40964-022-00328-0.

[24] E. M. Sefene, "State-of-the-art of selective laser melting process: A comprehensive review," *J Manuf Syst*, vol. 63, pp. 250–274, Apr. 2022, doi: 10.1016/J.JMSY.2022.04.002.

[25] J. Liu, G. Li, Q. Sun, H. Li, J. Sun, and X. Wang, "Understanding the effect of scanning strategies on the microstructure and crystallographic texture of Ti-6Al-4V alloy manufactured by laser powder bed fusion," *J Mater Process Technol*, vol. 299, Jan. 2022, doi: 10.1016/J.JMATPROTEC.2021.117366.

[26] B. Zhang, Y. Li, and Q. Bai, "Defect Formation Mechanisms in Selective Laser Melting: A Review," *Chinese Journal of Mechanical Engineering (English Edition)*, vol. 30, no. 3, pp. 515–527, May 2017, doi: 10.1007/S10033-017-0121-5/FIGURES/17.

[27] D. Agius, K. I. Kourousis, and C. Wallbrink, "A Review of the As-Built SLM Ti-6Al-4V Mechanical Properties towards Achieving Fatigue Resistant Designs," *Metals 2018, Vol. 8, Page 75*, vol. 8, no. 1, p. 75, Jan. 2018, doi: 10.3390/MET8010075.

[28] W. Hearn and E. Hryha, "Effect of Carbon Content on the Processability of Fe-C Alloys Produced by Laser Based Powder Bed Fusion," *Front Mater*, vol. 8, p. 547, Jan. 2022, doi: 10.3389/FMATS.2021.800021/BIBTEX.

[29] A. Thanki *et al.*, "Melt pool feature analysis using a high-speed coaxial monitoring system for laser powder bed fusion of Ti-6Al-4 V grade 23," *International Journal of Advanced Manufacturing Technology*, vol. 120, no. 9–10, pp. 6497–6514, Jun. 2022, doi: 10.1007/S00170-022-09168-2/TABLES/4.

[30] "a) schematic illustration of L-PBF process showing overlap of melt... | Download Scientific Diagram." https://www.researchgate.net/figure/a-schematic-illustration-of-L-PBF-process-showing-overlap-of-melt-pools-and-remelting-of_fig1_357698316 (accessed Mar. 17, 2023).

[31] H. Gong, K. Rafi, H. Gu, T. Starr, and B. Stucker, "Analysis of defect generation in Ti–6Al–4V parts made using powder bed fusion additive manufacturing processes," *Addit Manuf*, vol. 1–4, pp. 87–98, Oct. 2014, doi: 10.1016/J.ADDMA.2014.08.002.

[32] B. Zhang, Y. Li, and Q. Bai, "Defect Formation Mechanisms in Selective Laser Melting: A Review," *Chinese Journal of Mechanical Engineering (English Edition)*, vol. 30, no. 3, pp. 515–527, May 2017, doi: 10.1007/S10033-017-0121-5/FIGURES/17.

[33] T. Vilaro, C. Colin, and J. D. Bartout, "As-fabricated and heat-treated microstructures of the Ti-6Al-4V alloy processed by selective laser melting," *Metall Mater Trans A Phys Metall Mater Sci*, vol. 42, no. 10, pp. 3190–3199, Oct. 2011, doi: 10.1007/S11661-011-0731-Y/FIGURES/9.

[34] J. Platl, H. Leitner, C. Turk, A. G. Demir, B. Previtali, and R. Schnitzer, "Defects in a Laser Powder Bed Fused Tool Steel," *Adv Eng Mater*, vol. 23, no. 12, p. 2000833, Dec. 2021, doi: 10.1002/ADEM.202000833.

[35] P. Yadav, O. Rigo, C. Arvieu, E. Le Guen, and E. Lacoste, "In situ monitoring systems of the SLM process: On the need to develop machine learning models for data processing," *Crystals (Basel)*, vol. 10, no. 6, pp. 1–26, Jun. 2020, doi: 10.3390/CRYST10060524.

[36] J. Wang, S. Liu, Y. Fang, and Z. He, "A short review on selective laser melting of H13 steel," *International Journal of Advanced Manufacturing Technology*, vol. 108, no. 7–8, pp. 2453–2466, Jun. 2020, doi: 10.1007/S00170-020-05584-4/FIGURES/15.

[37] Y. Shi *et al.*, "Polymer materials for additive manufacturing—powder materials," *Materials for Additive Manufacturing*, pp. 9–189, Jan. 2021, doi: 10.1016/B978-0-12-819302-0.00002-X.

[38] I. Yadroitsev and I. Yadroitsava, "A step-by-step guide to the L-PBF process," *Fundamentals of Laser Powder Bed Fusion of Metals*, pp. 39–77, Jan. 2021, doi: 10.1016/B978-0-12-824090-8.00026-3.

[39] A. Mussatto, R. Groarke, A. O'Neill, M. A. Obeidi, Y. Delaure, and D. Brabazon, "Influences of powder morphology and spreading parameters on the powder bed topography uniformity in powder bed fusion metal additive manufacturing," *Addit Manuf*, vol. 38, Feb. 2021, doi: 10.1016/J.ADDMA.2020.101807.

[40] J. Wang, S. Liu, Y. Fang, and Z. He, "A short review on selective laser melting of H13 steel," *International Journal of Advanced Manufacturing Technology*, vol. 108, no. 7–8, pp. 2453–2466, Jun. 2020, doi: 10.1007/S00170-020-05584-4/FIGURES/15.

[41] V. Gunenthiram *et al.*, "Experimental analysis of spatter generation and melt-pool behavior during the powder bed laser beam melting process," *J Mater Process Technol*, vol. 251, pp. 376–386, Jan. 2018, doi: 10.1016/j.jmatprotec.2017.08.012.

[42] H. Chen and W. Yan, "Spattering and denudation in laser powder bed fusion process: Multiphase flow modelling," *Acta Mater*, vol. 196, pp. 154–167, Sep. 2020, doi: 10.1016/J.ACTAMAT.2020.06.033.

[43] Z. A. Young *et al.*, "Types of spatter and their features and formation mechanisms in laser powder bed fusion additive manufacturing process," *Addit Manuf*, vol. 36, Dec. 2020, doi: 10.1016/J.ADDMA.2020.101438.

[44] D. Wang *et al.*, "Mechanisms and characteristics of spatter generation in SLM processing and its effect on the properties," *Mater Des*, vol. 117, pp. 121–130, Mar. 2017, doi: 10.1016/J.MATDES.2016.12.060.

[45] J. Dawes, R. Bowerman, and R. Trepleton, "Introduction to the additive manufacturing powder metallurgy supply chain," *Johnson Matthey Technology Review*, vol. 59, no. 3, pp. 243–256, 2015, doi: 10.1595/205651315X688686.

[46] R. Groarke, R. K. Vijayaraghavan, D. Powell, A. Rennie, and D. Brabazon, "Powder characterization—methods, standards, and state of the art," *Fundamentals of Laser Powder Bed Fusion of Metals*, pp. 491–527, Jan. 2021, doi: 10.1016/B978-0-12-824090-8.00006-8.

[47] O. D. Neikov, "Atomization and Granulation," *Handbook of Non-Ferrous Metal Powders*, pp. 125–185, 2019, doi: 10.1016/B978-0-08-100543-9.00004-X.

[48] K. Kassym and A. Perveen, "Atomization processes of metal powders for 3D printing," *Mater Today Proc*, vol. 26, pp. 1727–1733, 2019, doi: 10.1016/J.MATPR.2020.02.364.

[49] S. Wallner, "Powder Production Technologies," *BHM Berg- und Hüttenmännische Monatshefte 2019 164:3*, vol. 164, no. 3, pp. 108–111, Mar. 2019, doi: 10.1007/S00501-019-0832-2.

[50] M. S. El-Eskandarany, "Introduction," *Mechanical Alloying*, pp. 1–11, Jan. 2020, doi: 10.1016/B978-0-12-818180-5.00001-7.

[51] "Gas atomization. Courtesy of LPW Technology, reprinted with permission... | Download Scientific Diagram." https://www.researchgate.net/figure/Gas-atomization-Courtesy-of-LPW-Technology-reprinted-with-permission-from-Ref-70_fig2_331798165 (accessed Apr. 08, 2023).

[52] "Metal powders for AM: Manufacturing processes and properties." https://www.metal-am.com/articles/metal-powders-for-3d-printing-manufacturing-processes-and-properties/ (accessed Apr. 08, 2023).

[53] "Water Atomization (WA) -Material Technology Innovations Co., Ltd." http://www.mt-innov.com/index.php?ac=article&at=list&tid=13 (accessed Apr. 08, 2023).

[54] J. J. Dunkley, "Metal powder atomisation methods for modern manufacturing," *Johnson Matthey Technology Review*, vol. 63, no. 3, pp. 226–232, Jul. 2019, doi: 10.1595/205651319X15583434137356.

[55] "Schematic representation of the plasma atomization process for the... | Download Scientific Diagram." https://www.researchgate.net/figure/Schematic-representation-of-the-plasma-atomization-process-for-the-production-of-Ti_fig1_331282809 (accessed Apr. 08, 2023).

[56] R. Garrard *et al.*, "Comparison of LPBF processing of AlSi40 alloy using blended and pre-alloyed powder," *Additive Manufacturing Letters*, vol. 2, p. 100038, Apr. 2022, doi: 10.1016/J.ADDLET.2022.100038.

[57] A.-A. Ali, P. Baumli, and G. Mucsi, "MECHANICAL ALLOYING AND MILLING", doi: 10.26649/musci.2015.017.

[58] X. Hu, L. Huang, W. Yan, W. Wang, Y. Shan, and K. Yang, "Study on microstructure stability of A Y2O3 dispersion strengthened low-activation steel," *Jinshu Xuebao/Acta Metallurgica Sinica*, vol. 51, no. 6, pp. 641–650, Jun. 2015, doi: 10.11900/0412.1961.2014.00547.

[59] "Ball mill - Wikipedia." https://en.wikipedia.org/wiki/Ball_mill#cite_note-1 (accessed Apr. 16, 2023).

[60] "1: Ball milling process. | Download Scientific Diagram." https://www.researchgate.net/figure/Ball-milling-process_fig1_320754012 (accessed Apr. 27, 2023).

[61] V. Vivacqua and M. Ghadiri, "Modelling of auto-agglomeration of cohesive powders," *Chemical Engineering Research and Design*, vol. 133, pp. 137–141, May 2018, doi: 10.1016/J.CHERD.2018.03.018.

[62] J. Clayton, D. Millington-Smith, and B. Armstrong, "The Application of Powder Rheology in Additive Manufacturing," *JOM*, vol. 67, no. 3, pp. 544–548, Mar. 2015, doi: 10.1007/S11837-015-1293-Z/FIGURES/7.

[63] I. Widyatmoko, "Sustainability of bituminous materials," *Sustainability of Construction Materials*, pp. 343–370, 2016, doi: 10.1016/B978-0-08-100370-1.00014-7.

[64] M. Gagliardi, "Rheology of elastomer blends and composites," *Elastomer Blends and Composites: Principles, Characterization, Advances, and Applications*, pp. 83–102, Jan. 2022, doi: 10.1016/B978-0-323-85832-8.00018-3.

[65] H. Zhang, S. LeBlanc, H. Zhang, and S. LeBlanc, "Processing Parameters for Selective Laser Sintering or Melting of Oxide Ceramics," *Additive Manufacturing of High-performance Metals and Alloys - Modeling and Optimization*, Jul. 2018, doi: 10.5772/INTECHOPEN.75832.

[66] P. H. M. Janssen, S. Depaifve, A. Neveu, F. Francqui, and B. H. J. Dickhoff, "Impact of Powder Properties on the Rheological Behavior of Excipients," *Pharmaceutics*, vol. 13, no. 8, Aug. 2021, doi: 10.3390/PHARMACEUTICS13081198.

[67] S. E. Brika, M. Letenneur, C. A. Dion, and V. Brailovski, "Influence of particle morphology and size distribution on the powder flowability and laser powder bed fusion manufacturability of Ti-6Al-4V alloy," *Addit Manuf*, vol. 31, Jan. 2020, doi: 10.1016/J.ADDMA.2019.100929.

[68] J. S. Weaver *et al.*, "The effects of particle size distribution on the rheological properties of the powder and the mechanical properties of additively manufactured 17-4 PH stainless steel," *Addit Manuf*, vol. 39, Mar. 2021, doi: 10.1016/J.ADDMA.2021.101851.

[69] M. Besterci, H. Käerdi, P. Kulu, and V. Mikli, "CHARACTERIZATION OF POWDER PARTICLE MORPHOLOGY," *Proceedings of the Estonian Academy of Sciences. Engineering*, vol. 7, no. 1, p. 22, 2001, doi: 10.3176/ENG.2001.1.03.

[70] "Characteristic of Metal Powders | Engineers Gallery." http://www.engineersgallery.com/characteristic-metal-powders/ (accessed Apr. 18, 2023).

[71] A. H. B. SEIDOU, "Development and evaluation of the powders mix low alloyed steel + SIC for selective laser melting," 2023, Accessed: Apr. 18, 2023. [Online]. Available: https://thesis.unipd.it/handle/20.500.12608/36370

[72] "Method II-Measurement in a Volumeter".

[73] A. P. Ferreira, C. F. Rawlinson-Malone, J. Gamble, S. Nicholson, and M. Tobyn, "Applications of Multivariate Analysis to Monitor and Predict Pharmaceutical Materials Properties," *Multivariate Analysis in the Pharmaceutical Industry*, pp. 235–267, 2018, doi: 10.1016/B978-0-12-811065-2.00008-4.

[74] M. H. Sehhat and A. Mahdianikhotbesara, "Powder spreading in laser-powder bed fusion process," *Granul Matter*, vol. 23, no. 4, pp. 1–18, Nov. 2021, doi: 10.1007/S10035-021-01162-X/FIGURES/21.

[75] T. Freeman, K. Brockbank, and J. Sabathier, "Characterising powder flow properties - The need for a multivariate approach," *EPJ Web Conf*, vol. 140, Jun. 2017, doi: 10.1051/EPJCONF/201714003008.

[76] J. Zegzulka, D. Gelnar, L. Jezerska, R. Prokes, and J. Rozbroj, "Characterization and flowability methods for metal powders," *Scientific Reports 2020 10:1*, vol. 10, no. 1, pp. 1–19, Dec. 2020, doi: 10.1038/s41598-020-77974-3.

[77] "Types Of Alloy Steel." https://www.materialwelding.com/types-of-alloy-steel/?utm_content=cmp-true (accessed Apr. 19, 2023).

[78] N. Haghdadi, M. Laleh, M. Moyle, and S. Primig, "Additive manufacturing of steels: a review of achievements and challenges," *J Mater Sci*, vol. 56, no. 1, pp. 64–107, Jan. 2021, doi: 10.1007/S10853-020-05109-0/FIGURES/19.

[79] F. Galbusera, A. G. Demir, J. Platl, C. Turk, R. Schnitzer, and B. Previtali, "Processability and cracking behaviour of novel high-alloyed tool steels processed by Laser Powder Bed Fusion," *J Mater Process Technol*, vol. 302, p. 117435, Apr. 2022, doi: 10.1016/J.JMATPROTEC.2021.117435.

[80] "7 Main Types of Tool Steels | Metallurgy." https://www.engineeringenotes.com/metallurgy/tool-steels/7-main-types-of-tool-steels-metallurgy/26566 (accessed Apr. 20, 2023).

[81] N. Takata, R. Nishida, A. Suzuki, M. Kobashi, and M. Kato, "Crystallographic Features of Microstructure in Maraging Steel Fabricated by Selective Laser Melting," May 2018, doi: 10.20944/PREPRINTS201805.0373.V1.

[82] J. Saewe, C. Gayer, A. Vogelpoth, J. H. Schleifenbaum, and J. Saewe, "Feasability Investigation for Laser Powder Bed Fusion of High-Speed Steel AISI M50 with Base Preheating System," *BHM Berg- und Hüttenmännische Monatshefte 2019 164:3*, vol. 164, no. 3, pp. 101–107, Feb. 2019, doi: 10.1007/S00501-019-0828-Y.

[83] J. J. Yan *et al.*, "Selective laser melting of H13: microstructure and residual stress," *J Mater Sci*, vol. 52, no. 20, pp. 12476–12485, Oct. 2017, doi: 10.1007/S10853-017-1380-3/FIGURES/8.

[84] J. Sander, J. Hufenbach, L. Giebeler, H. Wendrock, U. Kühn, and J. Eckert, "Microstructure and properties of FeCrMoVC tool steel produced by selective laser melting," *Mater Des*, vol. 89, pp. 335–341, Jan. 2016, doi: 10.1016/J.MATDES.2015.09.148.

[85] K. Kempen, B. Vrancken, S. Buls, L. Thijs, J. Van Humbeeck, and J. P. Kruth, "Selective Laser Melting of Crack-Free High Density M2 High Speed Steel Parts by Baseplate

Preheating," *Journal of Manufacturing Science and Engineering, Transactions of the ASME*, vol. 136, no. 6, Dec. 2014, doi: 10.1115/1.4028513.

[86] S. Qin *et al.*, "Influence of Preheating Temperature on Microstructure Evolution and Hardness of High-Speed Steel AISI M50 Processed by Laser Powder Bed Fusion," *Steel Res Int*, p. 2200784, 2023, doi: 10.1002/SRIN.202200784.

[87] S. J, W. MB, J. L, and S. J, "Influence of Preheating Temperature on Hardness and Microstructure of PBF Steel hs6-5-3-8," Jan. 2021, doi: 10.20944/PREPRINTS202101.0622.V1.

[88] Y. Karabulut and R. Ünal, "Additive manufacturing of ceramic particle-reinforced aluminum-based metal matrix composites: a review," *Journal of Materials Science 2022 57:41*, vol. 57, no. 41, pp. 19212–19242, Oct. 2022, doi: 10.1007/S10853-022-07850-0.

[89] C. Tan, J. Zou, D. Wang, W. Ma, and K. Zhou, "Duplex strengthening via SiC addition and in-situ precipitation in additively manufactured composite materials," *Compos B Eng*, vol. 236, p. 109820, May 2022, doi: 10.1016/J.COMPOSITESB.2022.109820.

[90] B. Song *et al.*, "Microstructure and tensile behavior of hybrid nano-micro SiC reinforced iron matrix composites produced by selective laser melting," *J Alloys Compd*, vol. 579, pp. 415–421, Dec. 2013, doi: 10.1016/J.JALLCOM.2013.06.087.

[91] B. Song, S. Dong, and C. Coddet, "Rapid in situ fabrication of Fe/SiC bulk nanocomposites by selective laser melting directly from a mixed powder of microsized Fe and SiC," *Scr Mater*, vol. 75, pp. 90–93, Mar. 2014, doi: 10.1016/J.SCRIPTAMAT.2013.11.031.

[92] A. Riquelme, C. Sánchez de Rojas Candela, P. Rodrigo, and J. Rams, "Influence of process parameters in additive manufacturing of highly reinforced 316L / SiCp composites," *J Mater Process Technol*, vol. 299, Jan. 2022, doi: 10.1016/J.JMATPROTEC.2021.117325.

[93] "Test sieve shakers | Haver & Boecker." https://www.haverboecker.com/en/produktloesungen/particle-analysis/sieve-analysis/haver-test-screening-machines/ (accessed May 02, 2023).

[94] "Planetary Mono Mill PULVERISETTE 6 classic line / Description - fritsch.de." https://www.fritsch-international.com/sample-preparation/milling/planetary-mills/details/product/pulverisette-6-classic-line/ (accessed May 01, 2023).

[95] "AconityMIDI | Aconity3D." https://aconity3d.com/products/aconity-midi/ (accessed May 02, 2023).

[96] "Spark Erosion: The Process Explained - A&M." https://www.amedm.co.uk/spark-erosion-explained/ (accessed May 02, 2023).

[97] "RITECA - Empastilladora de metales CitoPress-1." http://riteca.gobex.es/es/catalogo_infraestructuras/430/empastilladora-de-metales-citopress-1 (accessed May 02, 2023).

[98] "Tegramin grinding and polishing equipment | Struers.com." https://cd-us.struers.com/en/Products/Grinding-and-Polishing/Grinding-and-polishing-equipment/Tegramin (accessed May 02, 2023).

[99] "Olympus BX60M Reflected Light Brightfield & Darkfield Microscope – Microscope Central." https://microscopecentral.com/products/olympus-bx60m-reflected-light-brightfield-darkfield-microscope (accessed May 03, 2023).

[100] G. F. Vander Voort, "Microstructure of ferrous alloys," *Industrial Heating*, vol. 68, no. 1, pp. 28–34, 2001, doi: 10.1201/9781420030365.CH3.

[101] D. McMullan, "Scanning electron microscopy 1928–1965," *Scanning*, vol. 17, no. 3, pp. 175–185, 2006, doi: 10.1002/sca.4950170309.

[102] "TESCAN CLARA UHR SEM | Image Science." https://imagescience.hu/products/about-tescan/tescan-clara-uhr-sem/ (accessed May 03, 2023).

[103] "What is Electron Backscatter Diffraction (EBSD)? - Oxford Instruments." https://www.ebsd.com/ebsd-explained/what-is-ebsd (accessed May 03, 2023).

[104] "Energy-dispersive X-ray spectroscopy - Wikipedia." https://en.wikipedia.org/wiki/Energy-dispersive_X-ray_spectroscopy (accessed May 03, 2023).

[105] "AccuPyc II - Micromeritics AccyPyc Gas Displacement Pycnometer." https://www.micromeritics.com/accupyc-ii/ (accessed May 03, 2023).

[106] P. A. Hooper, "Melt pool temperature and cooling rates in laser powder bed fusion," *Addit Manuf*, vol. 22, pp. 548–559, Aug. 2018, doi: 10.1016/J.ADDMA.2018.05.032.

[107] "Netzsch STA 449 F1 Jupiter Simultaneous TGA/DSC Thermal Analyser | Download Scientific Diagram." https://www.researchgate.net/figure/2-Netzsch-STA-449-F1-Jupiter-Simultaneous-TGA-DSC-Thermal-Analyser_fig18_309571420 (accessed May 03, 2023).

[108] "CCHAPT - 3. Equipment Sheet - M1C 010 EmcoTest micro hardness tester." https://www.cchapt.ro/index.php/en/infrastructura-en/10-english/73-fisa-microdurimetru-en (accessed May 03, 2023).

[109] “M4R-奥地利EMCOTEST_M4R全自动端淬硬度试验机_EMCO-TEST硬度计-德瑞华测量技术（苏州）有限公司.” https://www.chem17.com/st318545/product_26135287.html (accessed May 03, 2023).

[110] S. Qin *et al.*, “Influence of Preheating Temperature on Microstructure Evolution and Hardness of High-Speed Steel AISI M50 Processed by Laser Powder Bed Fusion,” *Steel Res Int*, 2023, doi: 10.1002/SRIN.202200784.

[111] Y. Zou, C. Tan, Z. Qiu, W. Ma, M. Kuang, and D. Zeng, “Additively manufactured SiC-reinforced stainless steel with excellent strength and wear resistance,” *Addit Manuf*, vol. 41, p. 101971, May 2021, doi: 10.1016/J.ADDMA.2021.101971.

9 ANNEXES

Annex 1. Datasheet of S2 powders

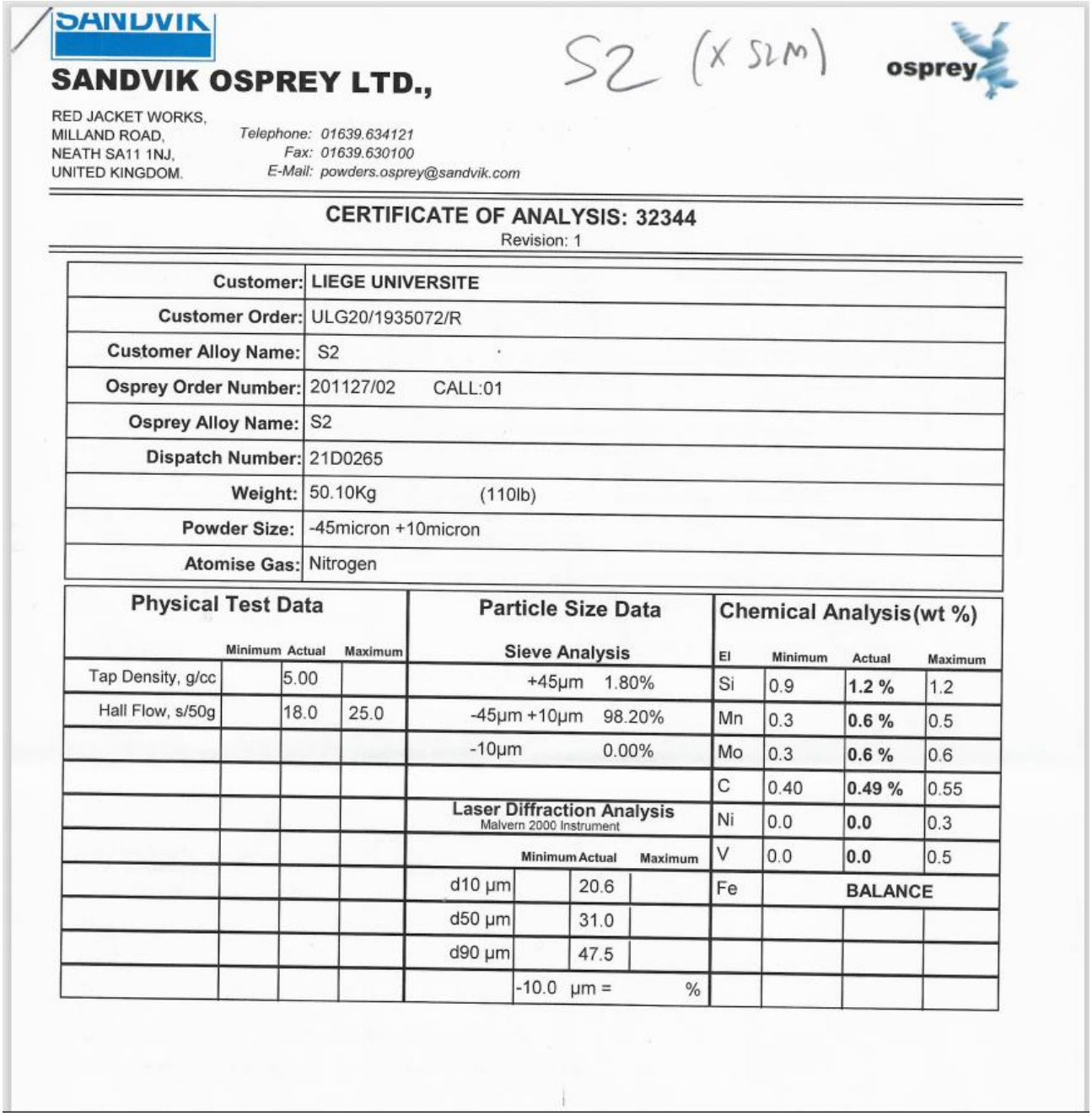

SANDVIK

SANDVIK OSPREY LTD.,

S2 (X 52M)

osprey

RED JACKET WORKS,
MILLAND ROAD,
NEATH SA11 1NJ,
UNITED KINGDOM.

Telephone: 01639.634121
Fax: 01639.630100
E-Mail: powders.osprey@sandvik.com

CERTIFICATE OF ANALYSIS: 32344

Revision: 1

Customer:	**LIEGE UNIVERSITE**
Customer Order:	ULG20/1935072/R
Customer Alloy Name:	S2
Osprey Order Number:	201127/02 CALL:01
Osprey Alloy Name:	S2
Dispatch Number:	21D0265
Weight:	50.10Kg (110lb)
Powder Size:	-45micron +10micron
Atomise Gas:	Nitrogen

Physical Test Data

	Minimum	Actual	Maximum
Tap Density, g/cc		5.00	
Hall Flow, s/50g		18.0	25.0

Particle Size Data

Sieve Analysis

+45µm	1.80%
-45µm +10µm	98.20%
-10µm	0.00%

Laser Diffraction Analysis
Malvern 2000 Instrument

	Minimum	Actual	Maximum
d10 µm		20.6	
d50 µm		31.0	
d90 µm		47.5	

-10.0 µm = %

Chemical Analysis (wt %)

El	Minimum	Actual	Maximum
Si	0.9	**1.2 %**	1.2
Mn	0.3	**0.6 %**	0.5
Mo	0.3	**0.6 %**	0.6
C	0.40	**0.49 %**	0.55
Ni	0.0	**0.0**	0.3
V	0.0	**0.0**	0.5
Fe	**BALANCE**		

Annex 2. Datasheet of SiC powders

KYOCERA

STARCERAM® S UF GRADES

2021.05.17

SPECIFICATIONS

- Chemical formula: SiC
- Chemical name: Silicon carbide
- Description of product: Alpha Phase SiC
- Colour: Grey

CHEMICAL CHARACTERISTICS (TYP.) [1,2]

		UF 05	UF 10	UF 15	UF 25
C	[%]	29.50 - 30.50	29.50 - 30.50	29.00 - 30.00	28.50 - 29.50
O	[%]	max. 0.70	max. 1.10	max. 1.50	max. 2.50
Al	[%]	max. 0.03	max. 0.03	max. 0.03	max. 0.04
Ca	[%]	max. 0.01	max. 0.01	max. 0.01	max. 0.01
Fe	[%]	max. 0.05	max. 0.05	max. 0.05	max. 0.05

[1] Mass fraction in % [cg/g]; ppm [µg/g]
[2] Information on testing methods on request

PHYSICAL CHARACTERISTICS (TYP.)

		UF 05	UF 10	UF 15	UF 25
α-SiC Acheson type mainly 6 H polytype					
Specific surface area [3]	[m^2/g]	4 - 6	9 - 11	14 - 16	23 - 26
Green density [4]	[g/cm^3]	1.70 - 1.90	1.65 - 1.80	1.60 - 1.80	1.50 - 1.70
Particle size distribution (TYP.) [5]					
D90 %	[µm]	6.0	2.2	1.5	1.0
D50 %	[µm]	2.2	0.9	0.75	0.65
D10 %	[µm]	0.6	0.45	0.4	0.35

[3] AREAMETER II by BET DIN 66 132
[4] 10^3 kg/cm^2
[5] MASTERSIZER 2000 by laser light diffraction per ISO 13320, deagglomeration with high energy ultrasonic before analysis

KYOCERA Fineceramics Precision GmbH · Lorenz-Hutschenreuther-Strasse 81 · 95100 Selb / Germany
Tel.: +49 (0)9287 - 807-0 · E-Mail: info@kyocera-precision.com · www.kyocera-precision.com

KYOCERA

STARCERAM® S UF GRADES

2021.05.17

SEM PHOTOMICROGRAPH

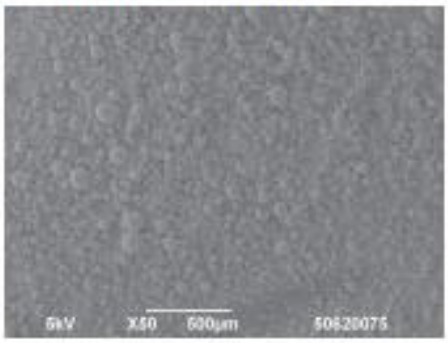

Granule scale

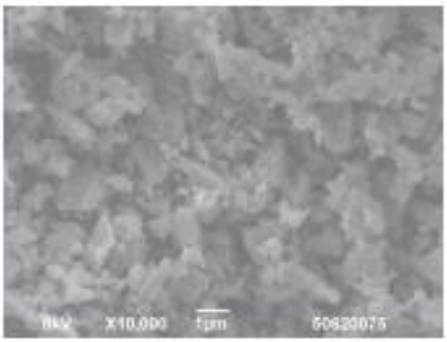

Primary particle scale

PACKAGING

- 25 kg steel drums with polyethylene inlet
- 12 drums on euro-pallet (800 x 1,200) = 1 packaging unit of 300 kg

STORAGE & HANDLING

The shelf-life for unrestricted processability is dependent on the storage conditions and the specific application it is used for.
Storage and handling are subject to the rules and regulations in the country of use.
Store at room temperature in a sealed closed, original container.

HAZARDS IDENTIFICATION IN ADVERTISING (REGULATION (EC) NO 1272/2008 ARTICLE 48)

none

DOCUMENTATION

An inspection document in accordance with EN 10204 is supplied with every shipment.

KYOCERA Fineceramics Precision GmbH · Lorenz-Hutschenreuther-Strasse 81 · 95100 Selb / Germany
Tel.: +49 (0)9287 - 807-0 · E-Mail: info@kyocera-precision.com · www.kyocera-precision.com